Wet electrostatic scrubbing for high efficiency submicron particle capture

by

Luca D'Addio

PHILOSOPHY DOCTOR DISSERTATION

Department of Chemical Engineering

UNIVERSITA' FEDERICO II di NAPOLI

2011

Scientific committee

Prof. W. Balachandran	Brunel University
Dott. F. Di Natale	Università Federico II
Prof. A. Lancia	Università Federico II
Prof. R. Nigro	Università Federico II

Table of Contents

List of Figures V

List of Tables IX

List of Symbols X

Abstract 1

CHAPTER I - **Particle emissions and available particle abatement technologies** 4

I.1. Particle Classification 4

I.2. Particles composition 5

I.3. Anthropogenic particle emissions sources 6

I.4. Particles health effects 8

I.5. Particles and global warming 9

I.6. Regulations 10

I.7. Particulate abatement technologies, an overview 11

I.7.1. Cyclone 11

I.7.2. Fabric Filter (FF) 12

I.7.3. Electrostatic precipitator (ESP) 13

I.7.4. Wet Scrubber (WS) 14

I.7.5. Submicron particle abatement, a general consideration 15

CHAPTER II - **Wet Electrostatic Scrubbing, an innovative technology for submicron particles capture** 18

II.1. Operating principle 18

II.2. Literature review 19

II.2.1. Theoretical framework 19

II.2.1.1. Droplet charging mechanisms 19

II.2.1.1.1. Droplet dynamic and evaporation modeling 24

II.2.1.2. Particle charging mechanisms 29

II.2.1.2.1. Corona discharge 32

II.2.1.2.1.1. Corona discharge for a wire-tube geometry 33

II.2.1.2.2. Back Corona 34
II.2.1.2.3. Dynamic of charged particle in a wire-tube geometry corona discharge 35
II.2.1.3. Particle capture due to droplets 36
II.2.1.3.1. Collisional mechanisms 37
II.2.2. Main theoretical and experimental results on particle abatement in wet electrostatic scrubbers 43
II.3. Considerations on literature results 48
CHAPTER III - **Materials and methods** 50
III.1. Experimental rig for droplet charge and size characterization 51
III.1.1. Preliminary results on droplet charging 54
III.1.2. Experimental protocol for droplet characterization 56
III.2. Experimental rig for particle charge and size characterization 58
III.2.1. Preliminary tests on particle charging 61
III.2.2. Experimental protocol for charged particles characterization 65
III.3. Experimental rig for particle abatement by wet electrostatic scrubbing 66
III.3.1. Preliminary experimental results on particle abatement 68
III.3.2. Experimental protocol for particle abatement 73
CHAPTER IV - **Experimental results and discussion** 75
IV.1. Introduction 75
IV.2. Experimental results on droplet characterization 75
IV.2.1. Scope of experimental section 75
IV.2.2. Experimental results on droplet charging 75
IV.3. Experimental results on particle characterization 82
IV.3.1. Scope of experimental section 82
IV.3.2. Experimental results on particle charging 83
IV.4. Experimental results on wet electrostatic scrubbing 90
IV.4.1. Scope of experimental section 90
IV.4.2. Lab-scale WES modeling 92
IV.4.3. Results and discussion on particle capture 95

CHAPTER V - **Conclusions** 109
Acknowledgment 114
References 115
Appendix - Particle abatement Data 122

List of Figures

Figure I-1: Schematic representation of the size distribution of particulate matter in ambient air 4

Figure I-2: Schematic comparison of typical particle size distributions in the waste gases of (- - - -) thermal process (wood combustion, lignite briquette combustion, heavy oil combustion and large combustion plants), (…….) mechanical (poultry farming, natural stone processing) and mixed (---) processes (cement factories, chemical plants) [2] 7

Figure I-3: Global mean radiative forcing of the climate system for the year 2000 [12] 9

Figure I-4: Comparison of removal efficiencies of different equipments as a function of particles diameter [15] 16

Figure II-1: Generalized geometry for an electrostatic spray charging 20

Figure II-2: Electric field lines for a conducting particle in a uniform field..... 30

Figure II-3: Example of field and diffusion charging at t_r= 46ms and $N_i=4\cdot10^{13}m^{-3}$..... 31

Figure II-4: Basic process involved during corona charging 32

Figure II-5: Schematic diagram showing the particle collection mechanisms by a water droplet..... 40

Figure III-1: Block diagram of the experimental approach 50

Figure III-2: Charged droplets generator assembly 52

Figure III-3: Needle dimensions in millimeters..... 52

Figure III-4: Experimental apparatus for droplet characterization 53

Figure III-5: Picture of the experimental apparatus for droplets characterization 54

Figure III-6: Droplet reduction due to voltage increase up to the formation of satellite droplets (c). The upper part of each picture is the charged droplets generator box..... 54

Figure III-7: Schematic representation of the wetting mode 55

Figure III-8: Incense stick box 59

Figure III-9: Grounded tube and high voltage wire partially shielded by PTFE cylinders and PTFE tube respectively 60

Figure III-10: Experimental apparatus for particles charge and size distribution measurements 60

Figure III-11: Picture of the experimental apparatus for particles characterization ... 60

Figure III-12: Experimental discharge current (dash line) and theoretical prediction (solid line) 61

Figure III-13: Current measured at the DFT (without particles) at air flow rate of 2.7m^3/h at 0kV (blue line) and -13kV (red line) 62

Figure III-14: Absolute values of the I_{DFT} due to charged particles (solid line) and total particle concentration (dash line) sampled during the time at 0, 9.5, 10.5, 11.5 and 12.5 kV. The mean velocity in the DFT is 8m/s. 63

Figure III-15: WES reactor layout 67

Figure III-16: Details of WES reactor (a-b) and complete system(c) 68

Figure III-17: Charged particle concentration (d_p=200nm) during the time in presence of charged droplets (q=100pC D=1.7mm, square symbols) and without droplets (circle symbols) 69

Figure III-18: Data of Figure III-17 reported in logarithmic coordinate 70

Figure III-19: Particle abatement (d_p=300nm) during the time in presence of charged droplets (q=70pC, D=1.2mm, red line) and without droplets (green line) 72

Figure IV-1: Example of current acquired during the dripping 76

Figure IV-2: Droplets diameter and charge to mass ratio for the conical needle at water flow rates of 0.50, 1.00 and 1.50mL/min (respectively red, green and blue symbols) at water electrical conductivities of 1.0 mS/cm (circles) and 20.0 mS/cm (triangles) 78

Figure IV-3: Droplets diameter and charge to mass ratio for the flat needle at water flow rates of 1.40, 1.85 and 2.00mL/min (respectively red, green and blue symbols) at water electrical conductivities of 1.0 mS/cm (diamonds) and 20.0mS/cm (triangles) 78

Figure IV-4:Droplet charge and droplet charge on Rayleigh limit for the conical tip needle at water flow rates of 0.50, 1.00 and 1.50mL/min (respectively red, green and blue lines) at water electrical conductivities of 1.0 mS/cm (solid line) and 20.0 mS/cm (dash line) 81

Figure IV-5: Droplet charge and droplet charge on Rayleigh limit for the flat tip needle at water flow rates of 1.40, 1.85 and 2.00mL/min (respectively red, green and blue lines) at water electrical conductivities of 1.0 mS/cm (solid line) and 20.0 mS/cm (dash line) 81

Figure IV-6: Incense typical particle size distribution during burning time 83

Figure IV-7: Measure of current at DFT and total particle concentration at $Q=2.6m^3/h$, $V_a=10kV$, L=18mm 84

Figure IV-8: Experimental (○) and theoretical (□) results on particle charge to mass ratio. The two lines represent the data regressions 86

Figure IV-9: Experimental (○) and theoretical (□) results on particle charge to surface ratio. The two lines represent the data regressions 87

Figure IV-10: Ratio of experimental and theoretical particle charge to mass ratio in function of the product of the residence time and ion concentration (a), and experimental values of mean current measured at the DFT vs. the predicted values obtained by equation (IV-7) (b) 88

Figure IV-11: Example of original particle charge by equation (II-15) at $t_r \cdot N_i=4.5 \cdot 10^{13}$ s/m^3 (solid red line) and $t_r \cdot N_i=9.9 \cdot 10^{12}$ s/m^3 (blue solid lines) and the correspondent corrected particle charge by equation (IV-8) (dash lines) 89

Figure IV-12: Droplet velocity along the axis of the reactor for three droplet size evaluated at $T_R=25°C$, $T_d=25°C$ and HR=20% 93

Figure IV-13: Droplet temperature (solid line) and diameter (dash line) along the axis of the reactor for D=1mm evaluated at $T_R=25°C$, $T_d=25°C$ and HR=20% 94

Figure IV-14: Experimental total and baseline scavenging coefficients. Experimental conditions: uncharged particles, D=0.9mm, q=79.4pC, $N \approx 11000 drops/m^3$ 96

Figure IV-15: Experimental and theoretical scavenging coefficients. Experimental conditions: charged particles, D=0.9mm, q=79.4pC, $N \approx 11000 drops/m^3$.Other conditions are reported in Appendix-Report 1 97

Figure IV-16:(a) Example of droplet initial (red + white bars); (b) particle abatement contribution divided in baseline contribution (green bars) and droplet contribution (blue bars) 99

Figure IV-17:Theoretical (purple point) and experimental distribution after four time elapsed from initial distribution. Green bars=baseline contribution, blue bars=droplet contribution, white bars=distribution after the time elapsed. Experimental conditions: charged particles, D=0.9mm, q=79.4pC, N≈11000drops/m^3. Other conditions are reported in Appendix-Report 1 100

Figure IV-18:Collisional efficiencies for the results in Figure IV-15. Experimental conditions are reported in Appendix-Report 1 101

Figure IV-19:Experimental and theoretical scavenging coefficients. Experimental conditions: charged particles, D=0.9mm, q=100.8pC, N≈9500drops/m^3.Other conditions are reported in Appendix-Report 6 103

Figure IV-20: Theoretical (lines and error bars) and experimental values (points) of a single droplet scavenging coefficients for droplet charge q=100.8pC (circle points) and q=79.4pC (square points) 104

Figure IV-21:Effect of droplet charge on single droplet theoretical (square symbols) and experimental (circle symbols) scavenging coefficient for three particle size 105

Figure IV-22:Effect of droplet concentration on theoretical (square symbols) and experimental (circle symbols) values of Λ/q for three particle size 105

Figure IV-23:Theoretical (square symbols) and experimental (circle symbols) particle collection efficiency in the reactor after the falling of 40000droplets, in function of droplet charge and for three particle size 107

Figure V-1: Rayleigh charge limit in function of the water drop diameter 112

Figure V-2: Particle abatement efficiency calculated with the equation (V-1) in function of the product between droplet concentration N and droplet residence time t_p in function of the droplet charge q. The particle size considered is dp=250nm and its charged is q_p=5e Experimental points presented in Figure IV-23 are reported too 113

List of Tables

Table I-1: PM emission in Europe in 27 EU member countries in 2005 [2] 7

Table II-1: Expressions for the evaporation correction (f_2), internal temperature gradient correction ($H_{\Delta T}$) and mass transfer potential (H_M) from various models [26] 26

Table II-2: Models for collisional efficiencies 42

Table IV-1: Regression coefficients for D-CMR in mC/kg for the conical needle 79

Table IV-2: Regression coefficients for D-CMR in mC/kg for flat needle 79

Table IV-3: Regression coefficients for droplet diameter in mm for the conical needle 80

Table IV-4: Regression coefficients for droplet diameter in mm for the flat needle 80

Table V-1: Range of the physical variables investigated at ambient temperature and ≈20% of relative humidity 110

List of Symbols

A_i	A	Experimental current acquired during the time Δt_i
c_i	m/s	Mean thermal speed of the ions at stand. cond. - 240 m/s
C_c	-	Cunningham correction factor $C_c = 1 + \frac{2\,\lambda_a}{d_p}\left(1.257 + 0.4exp\left(-\frac{1.1 d_p}{2\lambda_a}\right)\right)$
C_D	-	Droplet drug coefficient
C_L	J/kg K	Liquid water heat capacity
C_G	J/kg K	Air heat capacity
C_o	-	Coulomb Number $C_o = \frac{C_c\, q\, q_p}{3\pi^2\, \varepsilon_0\, \mu\, U\, D^2 d_p}$
D	m	Droplet diameter
D_0	m	Initial droplet diameter
D_{BR}	m^2/s	Particle Brownian diffusivity
D_R	m	Diameter of the reactor
D_w	m^2/s	Water diffusivity in the gas
D-CMR	C/kg	Droplet charge to mass ratio
d_p	m	Particle diameter
d_t	m	Diameter of the grounded tube in the corona charging
d_w	m	Wire diameter for corona charging
E	-	Total collision efficiency
E_0	V/m	Corona starting strength field
e	C	Elemental electric charge
E_{el}	V/m	Electric field
E_{ps}	V/m	Pseudo-homogeneous electric field
E_{BD}	-	Collision efficiency due to Brownian diffusion

E_{DI}	-	Collision efficiency due to directional interception
E_{Dph}	-	Collision efficiency due to diffusiophoresis
E_{Es}	-	Collision efficiency due to electrostatic attraction
E_{In}	-	Collision efficiency due to inertial impaction
E_{Th}	-	Collision efficiency due to thermophoresis
f_1	-	Correction factor to Stokes drag in droplet evaporation model
f_2	-	Correction factor to heat transfer in droplet evaporation model
g	m/s^2	Gravity acceleration
HR	%	Relative humidity
H_R	m	Height of the reactor
H_M	-	Specific driving potential
$H_{\Delta T}$	K/s	Additional terms in droplet evaporation model
I	A	Ion current in the corona discharge
I_{DFT}	A	Current measured at the Dynamic Faraday Tube
$\bar{I}_{Ex-DFT}$	A	Experimental mean current at the Dynamic Faraday Tube
$\bar{I}_{Th-DFT}$	A	Theoretical mean current at the Dynamic Faraday Tube
k_B	J/K	Boltzmann constant
K_c	Nm^2/C	Coulomb constant
K_e	Nm^2/C^2	Constant of proportionality - 9 10^9 Nm^2/C^2
k_g	W/mK	Gas thermal conductivity
Kn	-	Knudsen number
k_p	W/mK	Particle thermal conductivity
L	m	Length of the grounded tube in wire/tube for corona charging
Lv	J/kg	Latent water heat of evaporation
m	kg	Water mass collected during the sampling time

m_d	kg	Droplet mass
M_g	g/mol	Gas molecular weight
M_w	gr/mol	Water molecular weight
n	$1/m^3$	Numerical particle concentration
N	$1/m^3$	Numerical droplet concentration
N_i	$1/m^3$	Ion concentration in the electric field in the charging unit
Pr	-	Prandtl number
$P\text{-}CMR$	C/kg	Particles charge to mass ratio
$P\text{-}CMR_{th}$	C/kg	Theoretical particles charge to mass ratio
q	C	Droplet electric charge
q_{diff}	C	Particle charge to diffusion charging
q_{exp}	C	Experimental charge in the sampling time
q_{field}	C	Particle charge to field charging
q_p	C	Particle electric charge
q_R	C	Rayleigh droplet limit charge
q_s	C	Pauthenier particle limit charge
Q	m^3/s	Air flow rate
Q_w	m^3/s	Water flow rate
R	Pa m^3/mole K	Universal gas constant
Re	-	Droplet Reynolds number
RH	-	Relative humidity
Sc	-	Particle Schmidt number
Sc_w	-	Droplet Schmidt number
Sc_G	-	Air Schmidt number

St	-	Stokes number	$St = \frac{C_c \rho_p d_p^{\,2} U}{18 \mu D}$
St^*	-	Critical Stokes number in Slinn equation	
Sh	-	Sherwood number	
t	s	Time	
t_r	s	Particle residence time in the corona discharge	
t_d	s	Droplet residence time in the reactor	
t_p	s	Particle residence time in the reactor	
t_s	s	Sampling time	
T	K	Gas temperature	
T_d	K	Droplet temperature	
$T_{d,0}$	K	Droplet initial temperature	
T_G	K	Local gas temperature for droplet evaporation model	
T_G	K	Liquid phase normal boiling temperature	
T_R	K	Reactor temperature	
U	m/s	Droplet/particle relative velocity	
u	m/s	Particle velocity	
u_i	m/s	Gas velocity	
U_d	m/s	Droplet velocity	
$\bar{U}_d$	m/s	Mean droplet velocity in the reactor	
V_a	V	Applied voltage in particle charging unit	
V_E	V	Applied voltage to the charged droplets generator	
V_0	V	Starting voltage for corona discharge	
v_t	m/s	Particle terminal velocity in the corona discharge	
v_i	m/s	Local droplet velocity for evaporation modeling	

X	m	Droplet position
Y	-	Mass fraction of water vapor in the air
Z_i	m^2/Vs	Ion mobility – At standard condition 1.5 10^{-4} m^2/Vs

Greek symbols

α	-	Water packing factor – Jung and Lee model
β	-	Dimensionless surface roughness of electrode (1 for smooth surface)
δ	-	Relative density of the air (1 at standard condition)
ε	F/m	Air dielectric constant
ε_0	F/m	Vacuum dielectric constant
ε_r	F/m	Particles dielectric constant
Γ_w	N/m	Water superficial tension
η	-	Collection efficiency
η_c	-	Collection efficiency in the charging unit
η_c	-	Collection efficiency in the reactor due to the droplets
λ	m	Mean free path of gas ions
λ_a	m	Mean free path of air
Λ	s^{-1}	Scavenging coefficient
Λ_b	s^{-1}	Experimental baseline scavenging coefficient
Λ_d	s^{-1}	Experimental scavenging coefficient due to droplet
Λ_T	s^{-1}	Experimental total scavenging coefficient
μ	kg/ms	Gas viscosity
μ_w	kg/ms	Water viscosity

$\psi(D)$	1/µm·m^3	Droplet size distribution
$\bar{\psi}_p$	1/µm·m^3	Mean particle size distribution
$\bar{\psi}_{p,c}(d_p)$	1/µm·m^3	Mean particle size distribution corrected with Deutsch-Anderson equation
ψ_N	1/nm	Normalized particle size distribution
ψ_{N-th}	1/nm	Theoretical normalized particle size distribution
ω	-	Correction factor for field and diffusion charging
Ω	-	Number of fixed droplet
ρ	kg/m^3	Gas density
ρ_p	kg/m^3	Particle density
ρ_w	kg/m^3	Water density
σ	mS/cm	Water electrical conductivity
τ	*s*	Charging time constant for particles
τ_d	*s*	Droplet time constant for Stokes flow
χ	-	Mole fraction of the vapor

Abstract

Exposure to fine particulate matter has been associated with serious health effects, including respiratory and cardiovascular disease, and mortality. Very fine inhalable particles can remain suspended in the atmosphere for a long time, travel long distances from the emitting sources and, once inhaled, they can reach the deepest regions of the lungs and even enter in the circulatory system. Therefore, the smaller the particle size, the higher its toxicity. In typical combustion units used in process industry, the end-of-pipe technologies include trains of consecutive abatements devices. Nevertheless, the traditional particle abatement devices are mainly designed and optimized to treat particles with sizes above or around 1µm, and they are far less effective towards the submicron dimensions.

Among the end-of-pipe technologies, the Wet Scrubbers (WS) are widely utilized in industry due to their capacity to capture simultaneously gaseous pollutants and particles. The main particle collection mechanisms involved in WS are those related to directional interception and inertial impact, which allow high particle abatement efficiency for particles in micrometric range. Both the mechanisms are instead ineffective in the submicron range, thus resulting in low collection efficiencies.

It the past 40 years, it was demonstrated that the presence of electric charge of opposite polarities on the particles and the sprayed droplets can increase the capture efficiency due to Coulomb forces between the two phases. The presence of this additional contribution in a scrubber is an upgrade of the traditional wet scrubbing and the new process is commonly referred as Wet Electrostatic Scrubbing (WES).

Experimental investigation of the pertinent literature confirmed the ability of WES to increase the particle capture efficiency respect to the classic wet scrubber, but submicron range is generally not directly investigated so that the best operating conditions to increase submicron particle abatement efficiency is still an unsolved problem. This optimization problem is mainly related to the difficulties to model wet

electrostatic scrubbing process due to the high number of the variables involved, resulting in a complex experimental evaluation of the main collection mechanisms that are responsible of the particle capture. Above all, a significant hindrance to the assessment of a proper description of wet electrostatic scrubbing is the complexity of the electro-hydrodynamics of the charged water spray.

In this work, a new experimental methodology was adopted to perform experiments in controlled conditions in order to allow an easier investigation of the effects of the main physical variables on the abatement of submicron particles emission. This experimental approach is based on the use of a lab scale batch reactor, in which charged particles produced by combustion are inserted. In the reactor, a train of uniform droplet size and charge is used to remove the suspended particles. This approach has the main advantages to make possible to investigate specific parameters (like the effect of droplet charge or its size) under well-defined conditions and therefore model the particle abatement process.

Therefore, the objective of this work is the experimental analysis and the modeling of wet electrostatic scrubbing process for submicron particles with the new methodology developed and the evaluation of the influence of the main physical variables on the capture of submicron particles.

The results obtained confirm that the particle abatement is significantly enhanced by charging both particles and droplets, and that the particle abatement rate is directly proportional to the particles and droplet charges and droplet concentration. Furthermore, tests with uncharged particles and charged droplets do not show any relevant increase in the scrubbing efficiency with respect to common wet scrubbing in the investigated conditions.

The experimental results obtained were compared with the predictions of classical particle scavenging models valid for ambient temperature and humidity conditions. These models were rarely applied to submicron particles and found a reliable experimental support from the performed experiments. On the other hand, this

comparison also confirm the reliability of the experimental methodology in the study of wet electrostatic scrubbing and encourage the development of further tests in experimental conditions more similar to that of industrial scrubbers.

CHAPTER I - Particle emissions and available particle abatement technologies

I.1. Particle Classification

Particulate is a mixture of solid and/or liquid particles suspended in the air [1]. These suspended particles vary in size, composition and origin. It is convenient to classify particles by their aerodynamic properties, which is the size of a unit-density sphere with the same aerodynamic characteristics of the real particles

An idealized distribution of particulate matter in ambient air is shown in Figure I-1.

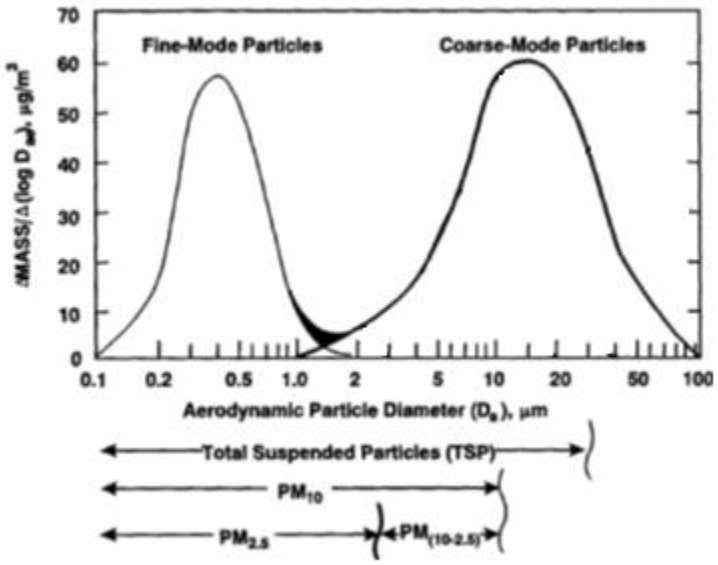

Figure I-1: Schematic representation of the size distribution of particulate matter in ambient air

The size of suspended particles reported in Figure I-1 in the atmosphere varies over four orders of magnitude, from a few nanometers to tens of micrometers. The largest particles, called the *coarse* fraction, are mechanically produced by the break- up of larger solid particles. These particles can include wind-blown dust from agricultural processes, uncovered soil, unpaved roads or mining operations. Near coasts,

evaporation of sea spray can produce large particles. Pollen grains, mould spores, and plant and insect parts are all in this larger size range. The amount of energy required to break these particles into smaller sizes increases as the size decreases, which effectively establishes a lower limit for the production of these coarse particles of approximately 1 μm. Smaller particles, called the *fine* mode, are largely formed from gases. The smallest particles, less than 0.1 μm, are formed by *nucleation*, that is, condensation of low vapor pressure substances formed by high-temperature vaporization or by chemical reactions in the atmosphere to form new particles (nuclei). Particles in this nucleation range can grow by *coagulation*, that is, the combination of two or more particles to form a larger particle. Coagulation is most efficient for large numbers of particles, and nucleation is most efficient for large surface areas. Therefore, the efficiency of both coagulation and nucleation decreases as particle size increases, which effectively produces an upper limit such that particles do not grow by these processes beyond approximately 1 μm. Thus, particles tend to "accumulate" between 0.1 and 1 μm; for this reason fine mode are generally referred as *accumulation range*.

Particles are then defined *primary* when they are present in the atmosphere as they are emitted from natural or anthropogenic sources. Instead they are named *secondary* if they are the result of chemical and physical reactions which take place in the atmosphere.

Combustion of fossil fuels such as coal, oil and petrol can produce coarse particles from the release of noncombustible materials, i.e. fly ash, fine particles from the condensation of materials vaporized during combustion, and secondary particles through the atmospheric reactions.

I.2. Particles composition

The composition of particles depends on their source. Wind-blown mineral dust tends to be made of mineral oxides and other materials blown from the Earth's crust. Sea

salt is considered the second-largest contributor in the global particle budget, and consists mainly of sodium chloride originated from sea spray; other constituents of atmospheric sea salt reflect the composition of seawater, and thus include magnesium, sulfate, calcium, potassium, etc. In addition, sea spray aerosols may contain organic compounds, which influence their chemistry.

The precursors of the secondary particles may have an anthropogenic origin (from fossil fuel or coal combustion) and a natural biogenic origin. In the presence of ammonia, secondary aerosols often take the form of ammonium salts; in the absence of ammonia, secondary compounds take an acidic form as sulfuric acid and nitric acid. Organic matter (OM) can be either primary or secondary, the latter part deriving from the oxidation of VOCs; organic material in the atmosphere may either be biogenic or anthropogenic. Another important aerosol type is constituted of elemental carbon (EC, also known as black carbon, BC). Organic matter and elemental carbon together constitute the carbonaceous fraction of aerosols.

I.3. Anthropogenic particle emissions sources

Particulate emission sources are mainly related to industrial activities, even though the major exposure risks are related to those sources active in urban areas - such as domestic heating, urban traffic and emission of the diesel engines of harbored vessels - usually accounting for a 30% of the total particulate emission inventories.

Particles emission related to different anthropogenic activities are resumed in Table I-1 and Figure I-2.

Sector	Emissions in Gg/year		
	$PM_{2.5}$	$PM_{>10}$	PM_{10}
Combustion in energy and transformation industry	137	110	247
Non-industrial combustion plants	517	125	642
Combustion in manufacturing industry	150	66	216
Production processes	219	183	402
Extraction and distribution of fossil fuels	26	49	75
Solvent and other product use	22	11	33
Road transport	267	82	349
Other mobile sources and machinery	140	17	157
Waste treatment and disposal	59	14	73
Agriculture	87	213	300
Total	1625	870	2495

Table I-1: PM emission in Europe in 27 EU member countries in 2005 **[2]**

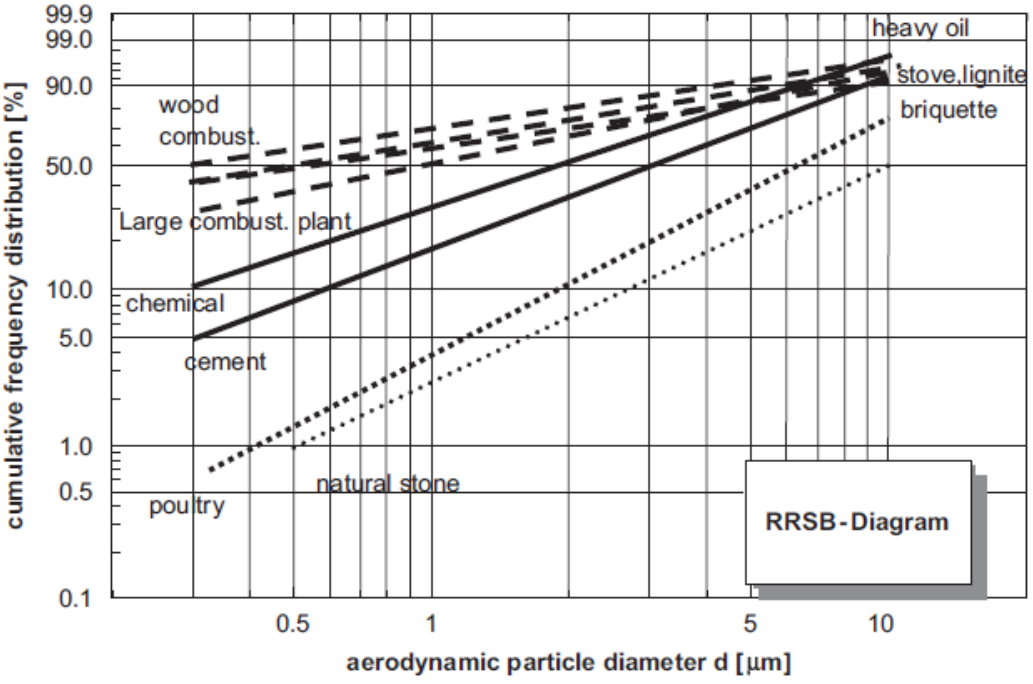

Figure I-2: Schematic comparison of typical particle size distributions in the waste gases of (- - - -) thermal process (wood combustion, lignite briquette combustion, heavy oil combustion and large combustion plants), (…….) mechanical (poultry farming, natural stone processing) and mixed (---) processes (cement factories, chemical plants) **[2]** .

Table I-1 and Figure I-2 clearly show that the combustion processes are the main atmospheric sources of particulate: in particular, the PM_{10} portion (particles with size up to 10μm) accounted for more than 90wt% of the emitted particles, while the $PM_{2.5}$ and the $PM_{1.0}$ are, respectively, the 60-80wt% and the 50-70wt% of the total.
Then particles produced by combustions processes represent the larger portion of anthropogenic particles, furthermore they produce large quantity of submicron particles.

In urban environments the major sources of pollution are the motor vehicle emissions and more than 80% of particle emissions in terms of particle number are of ultrafine size (less than 100nm) [3-7].
In environments affected by motor vehicle emissions, ultrafine particles can account for levels of up to an order of magnitude higher than those in natural environments.
The emission of particulate from ships should not be overlooked; it was recently estimated that ships produce at least 5% of black carbon global output [8].

I.4. Particles health effects

The large number of deaths and other health problems associated with particulate pollution was first demonstrated in the early 1970s [9]. PM pollution is estimated to cause 22,000-52,000 deaths per year in the United States in 2000 [10] and 200,000 deaths per year in Europe.
Epidemiological studies [1, 11] have demonstrated that particulate matter and chronic disease are strictly correlated. In fact, the porous nature of the particles causes cancerogenic compound adsorption and increases health risk due to their presence. The toxic effect of particulate is thus related both to the actual structure of the particles and to the kind of substance that particulate can transfer in human bodies. The main route of contamination is the inhalation of polluted air. The particles size determines where, in the respiratory tract, they will deposit when inhaled. Particles larger than ten

microns are generally filtered in the nose and throat and do not cause problems, while particles smaller than ten micron can reach the bronchi, penetrate the deepest part of the lungs and cause serious health problems. For example, it was demonstrated that $PM_{2.5}$ leads to high plaque deposits in arteries, causing vascular inflammation and atherosclerosis, which can lead to heart attacks and other cardiovascular problems [11].

I.5. Particles and global warming

Particulates and aerosols, both natural and anthropogenic, can affect the climate by changing the way radiation is transmitted through the atmosphere. The chemical composition of the aerosol directly affects how it interacts with solar radiation. The radiative forcing can be assumed as the parameter to identify if a compound provides a positive contribution to the global warming. Radiative forcing is a measure of how the energy balance of the Earth-atmosphere system is influenced when factors that affect climate are altered. The word "radiative" means that the factors affect the balance between incoming solar radiation and outgoing infrared radiation within the Earth's atmosphere. Positive forcing tends to warm the surface while negative forcing tends to cool it. In Figure I-3 is reported the radiative force of different compound presented in the atmosphere.

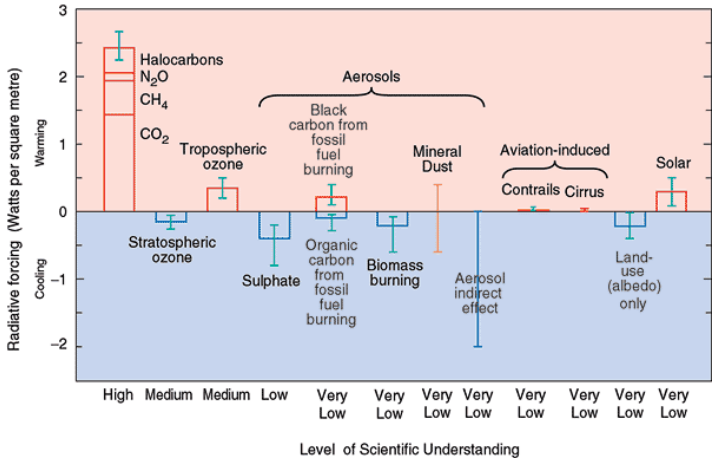

Figure I-3: Global mean radiative forcing of the climate system for the year 2000 **[12]**

The rectangular bars in Figure I-3 represent estimates of the contributions of some natural or anthropogenic compounds on the radiative forcing, some of which yield warming, and some cooling.

The radiative forcing of the black carbon is about 0.25 W m^{-2} classifying the BC as a greenhouse compound. However recent study have shown that the emissions of black carbon are the second strongest contribution to current global warming, after carbon dioxide emissions, with a radiative forcing estimated in 0.9 W m^{-2} [13].

This effect is confirmed by researches from NASA and Columbia University [14] witch show that more than 25 percent of the increase in average global temperature between 1880 and 2002 may be due to soot contamination of snow and ice worldwide. Pure snow and ice can be blindingly bright, reflecting large amounts of incoming radiation back into space, whereas snow and ice that is contaminated with black carbon absorbs incoming solar radiation. The scientists estimate that a soot content of only a few parts per billion can reduce snow's ability to reflect incoming radiation by 1 percent. In North America, soot has reduced snow's reflectivity by 3 percent [14].

I.6. Regulations

In Italy the emission of PM are regulated by the Dlg. 152/06 that limit the amount of particle emitted by specific plants in terms of PM10.

With reference to air quality in urban areas, the DM60/2002, 99/30/CE and 00/69/CE directives implementation set some limit values for different polluting substances, like particulate. The decree establishes a 50μg/m^3 daily threshold, for PM10, not to exceed more than 35 times per year and a 40μg/m^3 year's threshold. Starting from 1/1/2010 the annual limit value in ambient air has been lowered to 20 μg/m^3 and the daily limit value of 50μg/ m^3 can be exceeded at most 7 times per year.

Moreover, the new 08/50/CE directive introduces the PM2.5 concentration valuation method and sets a 25μg/m^3 limit value within 1st January 2020.

Similarly, more restrictive regulations have been applied to light duty vehicles (passenger cars and light commercial vehicles). In 2007, the Regulation 715/2007 (Euro 5/6) introduced some important regulatory steps implementing emission standard for light-duty vehicles and, from September 2011, a *particle number*

emission limit in addition to the mass-based limits is introduced for the new diesel vehicle (category M1) .

Also in naval field, several countries have introduced specific regulations to reduce the emission factors of ships and recently (March 2010) the International Maritime Organization (IMO) has enforced its environmental regulations. The adoption of the new regulations (MARPOL, Annex VI), which are far more restrictive than those previously in force, requires modification of the entire commercial fleet that has to be retrofitted with innovative solutions.

I.7. Particulate abatement technologies, an overview

Actually, several consolidated technologies for particle capture exist, such as separators, cyclones, fabric filters (FF), electrostatic precipitators (ESP), Wet Scrubber (WS) together with some new technologies, still under investigation. Their specific operating conditions, system design and capture efficiency are different for each technology and are briefly described in the following.

I.7.1. Cyclone

Cyclones use inertia to remove particles from gas streams, imparting centrifugal forces, in a purposely designed conical chamber. They operate by creating a double vortex inside the cyclone body.

The incoming gas is forced into circular motion down the cyclone near the inner surface of the cyclone tube. At the bottom, the gas turns and spirals up through the center of the tube and out of the top of the cyclone. Particles in the gas stream are forced toward the cyclone walls by the centrifugal force of the spinning gas but are opposed by the drag force of the gas travelling through and out of the cyclone. Large particles reach the cyclone wall and are collected in a bottom hopper, whereas small particles leave the cyclone with the exiting gas.

Cyclones are simple installation units used to primarily control particles over PM10, however, there are high efficiency cyclones designed to be effective even for PM2.5.

Only low maintenance is required for cyclones: easy periodic inspection of the unit for erosion or corrosion. The pressure drop across the cyclone is routinely monitored and the dust handling system is checked for blockages.

Cyclones themselves are generally not adequate to meet air pollution regulations, but they can be used as precleaners for more expensive final control devices such as fabric filters or electrostatic precipitators. In addition, they have the great advantage to operate at high temperatures.

When very large gas volumes must be handled and high collection efficiencies are needed a multiple of small diameter cyclones are usually nested together to form a multicyclone.

I.7.2. Fabric Filter (FF)

In a fabric filter, waste gas is forced through a tightly woven or felted fabric, collecting particulate matter on the fabric by sieving or other mechanisms. Fabric filters can be in the form of sheets, cartridges or bags (the most common type) with a number of the individual fabric filter units housed together in a group. When low particles loads occur, filter collection efficiency is primary related to the filter pore size and length, but when high particulate loading is treated, it forms a “cake” on the filter surface, which significantly increases the collection efficiency.

Fabric filters are used, primarily, to remove particulate matter down to PM2.5 and hazardous air pollutants in particulate form, such as metals. This technology is useful to collect particulate matter with electrical resistivities either too low or too high for Electrostatic Precipitator, so they are suitable to collect fly ash from low-sulphur coal or fly ash containing high levels of unburned carbon. The addition of a baghouse downstream of an ESP has been found to achieve very low particulate emissions.

When the waste gas loading consists of relatively large particulates, upstream mechanical collectors, such as cyclones, electrostatic precipitators or spray coolers may be used to reduce the load for the fabric filter, especially at high inlet concentrations.

Practical application of fabric filters requires the use of a large filter surface to avoid an unacceptable pressure drop, which can cause failure of the filter housing, resulting in fugitive dust emissions.

The intensity and the frequency of cleaning are important variables in determining removal efficiency. Indeed, the dust cake can provide a significant fraction of the fine particulate removal capability of a fabric. A cleaning, which is too frequent or too intense, will lower the removal efficiency. On the other side, if removal is too infrequent or too ineffective, the pressure drop will become too high.

I.7.3. Electrostatic precipitator (ESP)

An ESP is a particulate control device that uses electrical forces to move particles entrained within a waste gas stream onto collector plates. The entrained particles acquire an electrical charge when they pass through an electric field generated by a corona discharge electrode. These are placed in the center of the flow lane, generate the electrical field that forces the particles to the collector walls. Although corona discharge occurs above 8kV, in practice the DC voltage required is in the range of 20-100kV.

Electrostatic precipitators are used to remove particulate matter down to PM2.5. ESPs have the advantage of low pressure drop through the device and a high efficiency. However, ESP disadvantages are mainly connected with the high voltages and power required and the discontinuous operation because of their maintenance, such as electrodes cleaning. Moreover, the possibility of dust explosion owing to electric discharges represents a serious problem.

The ESP can be of two types: wire-plate or wire-pipe. In the first one, the waste gas flows horizontally and parallel to vertical plates of sheet material. The high voltage electrodes are long wires that are weighted and hang between the plates. Within each flow path, gas flow must pass each wire in sequence as it flows through the unit.

In the wire-pipe ESP (or tubular ESP) the exhaust gas flows vertically through conductive tubes, generally with many tubes operating in parallel. The high voltage electrodes are long wires suspended from a frame in the upper part of the ESP that run through the axis of each tube.

ESPs may work both as single or as two stage units. In single stage ESP, the electric field that generates the corona discharge is also used to attract and remove the charged particles, with charging and discharging taking place in one device. This equipment is used in large complex flue gas treatment systems, e.g. in power stations and waste incinerations, for dust and fly ash abatement. As part of the dust, heavy metals and their compounds are eliminated as well and disposed of together with other particulates. It is also suitable for separating aerosols and mists. In a two stage ESP, charging and removal of the particles occur in separate electric fields. The second stage, purely electrostatic, is applied to remove dust and oil mists. The two stage ESP is common where small waste gas streams (<90000 Nm^3/h) and a high proportion of submicron particles, e.g. smoke or oil mist, are involved.

I.7.4. Wet Scrubber (WS)

Wet Scrubbers are particulate matter control devices that rely on direct and irreversible contact of a liquid with the PM. They are usually classified according to the method used to put in contact the gas and the liquid as spray towers, packed bed scrubber and Venturi scrubbers.

In a spray tower, the liquid is mixed with the gas stream to promote contact with the PM. Instead, in a packed-bed scrubber, layers of liquid are used to coat packing material of various shapes that become impaction surfaces for the particle-laden gas.

In a Venturi scrubber a “throat” section forces the gas stream to accelerate due to the duct narrowing, with a consequent pressure decrease, to improve gas-liquid contact. [15]. In spite of its simplicity, Venturi scrubbers have a very effective gas-liquid contact with high particle capture efficiency; but it produce high pressure drop.

One of the main advantages of wet scrubbers is their ability to remove and recover dusts additionally to gaseous compounds, with quite high collection efficiency.
On the other hand, the main disadvantages associated with wet scrubbers are their potential for corrosion and freezing, the low particle collection efficiency in the particles range of about 0.1-2µm and the generation of a liquid by-product that has to be suitable treated.

I.7.5. Submicron particle abatement, a general consideration

Although various technologies already exist to effectively remove coarse particulate matter from flue gases, recent environmental and medical studies are forcing the introduction of more restrictive limits for submicron particles, driving the development of more cost effective gas cleaning technologies for these particle sizes.
Indeed, submicron particles are highly toxic and are produced in large amounts during natural and anthropic activities. Nevertheless, their detection is a complex problem itself. In fact, industrial emissions are always characterized by a wide particle size distribution ranging from few nanometers to tens of microns. The same measure of particles mass distribution in place of number distribution in the flue gas poses a severe hindrance to the determination of finer particles, whose contribution to the mass of collects particles is negligible. Anyway, a large amount of fine particles can produce large particles as a secondary aerosol in the atmosphere also contributing to overcome the daily limit in urban areas.

As shown in the previously paragraph, the existing technologies have low efficiency for fine particles, and both experimental and theoretical evidences pointed out that the capture efficiency is drastically reduced in the particle diameter range from 0.01 to 1µm, called *Greenfield gap* region. Therefore, a new challenge of the scientific

research is the development of new cleaning systems to remove particles from flue gas and the optimization of the existing technologies in order to improve the particle capture of submicron particles, in particular in the Greenfield gap.

Generally, spray towers (usually referred simply as wet scrubbers) allow the capture of particles in a wide range of working conditions. Typical particle collection efficiencies are higher than 90% for particle diameters coarser than 1μm and finer than 0.1μm, but lower than the typical values obtained with electrostatic precipitators, and fabric filters that, at the moment represent the Best Available Technology (BAT) for high efficiency particle abatement [16]. Moreover, the wet scrubber efficiency falls down at 60-70% in the Greenfield gap range, resulting sensibly less effective than ESP and FF as shown in Figure I-4, where the trends of collection efficiency, as a function of particulate diameter, are reported for different equipments.

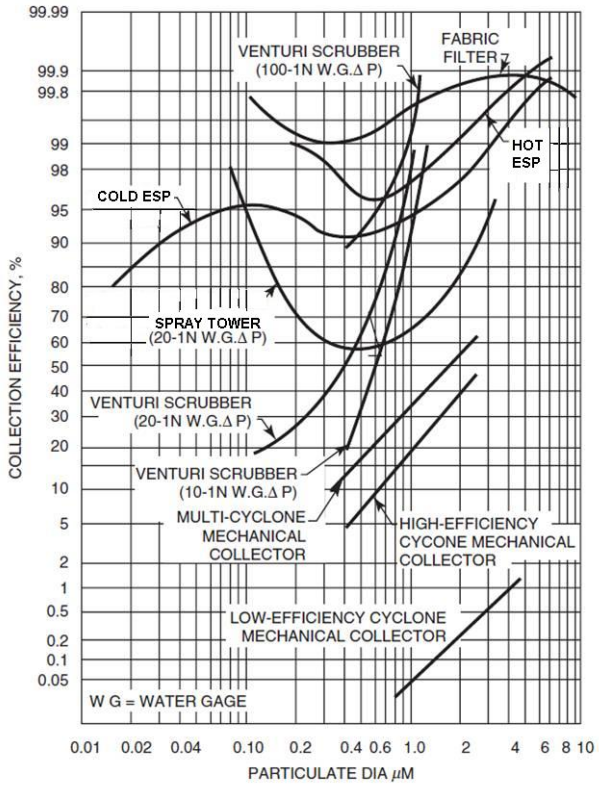

Figure I-4: Comparison of removal efficiencies of different equipments as a function of particles diameter **[15]**

In spite of this lack of efficiency in the Greenfield gap, wet scrubbers presents many advantages as the low pressure drops, the reduced process costs, the possibility to work at high temperature and the simultaneous ability to capture particles and gaseous pollutants (SOx, NOx , HCl, soluble VOCs).

In order to increase the submicron particle abatement efficiency, wet scrubbers can be proficiently upgraded by the electrification of sprayed water and the particles in a gas stream resulting in electrodynamics interactions among particles and droplets. This approach is generally known as Wet Electrostatic Scrubbing and is presented in detail in the following CHAPTER II.

CHAPTER II - Wet Electrostatic Scrubbing, an innovative technology for submicron particles capture

II.1. Operating principle

Starting from the early seventies of the last century, it was suggested that Wet Scrubbers technology could be improved to achieve higher collection efficiencies in the Greenfield gap, by coupling the typical hydrodynamic forces active in the scrubbing phenomena to electrostatic interactions.

In fact, since conventional Wet Scrubbers efficiency mainly rely on the inertial impaction between PM and liquid droplets, they generally have poor efficiency for particles in the Greenfield gap. Electrostatic forces between particles and droplets can significantly increase scrubber collection efficiency for submicrometer particles. In this way, the charged droplets sweeping the precipitation chamber act as small collectors attracting the particles due to Coulomb force. A practical example of these electrostatic phenomena is the atmospheric aerosol scavenging during thunderstorms, when the highest particle removal is achieved [17].

There are different types of Wet Electrostatic Scrubbing systems and several types of charging and spraying configurations are possible. A single reactor can be used with PM charged either negatively or positively and scrubbed by droplets with the opposite polarity. Otherwise two particulate abatement chambers can be used to treat naturally charged aerosol with droplets charged in the two polarities.

The promising features of the Wet Electrostatic Scrubbing have driven the scientific community toward the definition of appropriate criteria for design and operation of industrial equipments based on this process. The main literature results are reviewed in the following paragraph.

II.2. Literature review

The objective of this paragraph is to present the models involved in the wet electrostatic process and the main experimental and theoretical literature results on particle abatement due to wet electrostatic scrubbing phenomena.
The literature is therefore subdivided in two sections: in the first one (II.2.1) a theoretical framework to model the droplet and particle charging, and the interactions involved during particle capture due to charged droplet are presented. In the second section (II.2.2) the main theoretical and experimental literature results on wet electrostatic scrubbing process are instead reported.

II.2.1. Theoretical framework

II.2.1.1. Droplet charging mechanisms

Due to the complexity and the extension of this field, this section cannot provide a comprehensive description of droplet charging. Indeed this is intended to provide a simple and brief introduction to the main systems actually used to produce a charge spray.

Three are the main charging mechanisms applicable to liquids, i.e., corona charging, contact charging, and induction charging. These methods can be illustrated by observing the industrial charger developed by Law [18] and presented in Figure II-1, where it is shows a continuous jet J of liquid flowing at a velocity V from a fluid nozzle N and directed towards an outlet end. The nozzle N, the ring C, and the point P are three different kinds of electrodes (L1, L2, and L3).

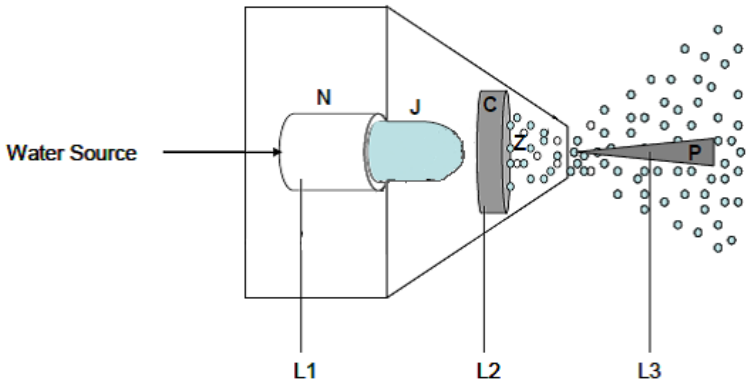

Figure II-1: Generalized geometry for an electrostatic spray charging

Thanks to the interaction of high pressure air (for an air assisted nozzle) or because of the water is pumped at high pressure (pneumatic nozzle), the continuous liquid jet may be disrupted into discrete airborne droplets within a droplet-production zone Z between the nozzle N and the point P. The cylindrical electrode C is coaxial with this jet. With the layout reported in Figure II-1 the three charging mechanisms can be discussed:

1. ***Corona charging***. Grounding the conductors L1 and L2 and applying a sufficiently high DC potential to conductor, L3 will result in the dielectric breakdown of the air immediately surrounding the metal point P. The needle P is than the discharge electrode. Consequently, as regards the cylindrical geometry shown in Figure II-1, a self-sustaining gaseous-discharge current will flow between P and C. In this way, major portion of cylindrical gap is occupied by unipolar air ions travelling outward along the radial electric-field lines to toward the non-ionizing electrode C. When a stream of liquid passes close to the ionizing needle tip, the charged ions produced are attracted to the liquid and carried away by it.

The level of charge is dependent on the dielectric constant of the spray, its surface area, the electrical characteristics of the corona discharge and the residence time within the ionized field.

The nozzle is usually negatively charged, as higher voltages are required to create an equivalent positive corona. Liquids with a wide range of conductivities can be charged with this method [19].

2. ***Contact charging***. If the metal nozzle is connected by the conductor L1 to a voltage source (while L2 and L3 remain unconnected) an excess supply of free charge are present in the liquid; in this way the charge in the liquid can be trapped during spray formation. As regards conductive liquids, to maintain the fluid nozzle at an elevated voltage, entire liquid bulk and liquid-handling system have to be maintained at that elevated voltage.

3. ***Induction charging***. An excess of negative charge will accumulate on the grounded liquid jet J if the potential is applied to the cylindrical electrode C by the connection of a voltage source between conductors L1 and L2 (L3 remaining unconnected). This happens for every liquid having non-zero electrical conductivity. The charge transfer results from electrostatic induction of electrons onto the axial jet in order to maintain it at ground potential in the presence of nearby charged cylindrical electrode.

   Spray droplets formed from the charged jet will themselves carry a charge of the same polarity as the jet. The charge on the sprayed droplets is than opposite of that on the electrode. So, some sprayed droplets can be attracted by the electrode, which, if wetted, is liable to the short circuit. An air stream is used on some nozzles to blow droplets away from the electrode and keep it dry.

In the case of both contact and induction charging, electrostatic charge is applied to the liquid and then transferred to the spray droplets as then are formed. Conversely, in the case of corona charging, the charge is applied to the droplets themselves.

Therefore, contact and corona charging result in a spray charge of the same polarity as the charging electrode, whereas induction charging leads to a spray charge of the opposite polarity.

The charge, *q*, generated on a droplet depends on the electrical charging system and can be considered as a fraction of the so called Rayleigh limit, q_R, which is the highest electrical charge that can be present on a droplet of a given diameter, *D*, without making it unstable and eventually tearing it apart. The Rayleigh limit of a droplet of diameter *D* can be calculated using the following formula.

$$q_R = \sqrt{8\pi^2 \, \Gamma_w \, \varepsilon_0 D^3} \qquad \text{(II-1)}$$

Charging of droplets in corona discharge is not an effective method because the charge on the droplets is much smaller than that obtained by induction. Another disadvantage is that the droplets are precipitated on the corona-electrode isolators. Droplets charged by induction are usually one order of magnitude lower than the Rayleigh limit, but induction charging can be used when a large amount of water is required [20]. The same charge level can be obtained by contact charging. In the case of contact charging, where the electrode is in direct contact with the liquid supply, a voltage breaking device is necessary in order to isolate the liquid circuit near the charging device from earth. This problem can limit the use of contact charging in industrial application to safety concerns [21].

It must to be pointed out that none of the industrial mechanisms presented are able to produce uniform droplet sizes.

In addition to these three methods, another important mechanism to produce charged droplet is the Electrohydrodynamic (EHD) atomization often also referred as *Electrospraying*. This is a physical process where the electric field itself is the cause of the atomization of a liquid into fine droplets.

A sample electrospray consists of a needle, in which the liquid in pumped, connected to a high voltage generator; the needle tip is placed near a grounded surface. The liquid at the tip of the needle is subject to electrical and mechanical forces able to elongate the liquid meniscus formed at the outlet of a capillary, to a jet that then disrupts into droplets because of electrical and mechanical forces.

The formation of an electrostatic spray can be observed by gradually applying a potential to a capillary through which a liquid is flowing at a relatively low flow rate. With no voltage applied, the liquid drips from the capillary as droplets of a volume dependent on the surface tension. Under the action of a small electric field, the electric force operates with the gravitational force, thus reducing the critical volume for drop detachment. A change in the shape of the drop and an increase in the dripping rate are observed as the electric field is increased. This is known as the *dripping mode* [22].

With a further increase in the applied electric field, a potential that is slightly larger than the one needed to cause instability of the liquid meniscus is reached. At this critical potential, the liquid ejects either a small droplet or a long filament. This filament breaks off and the liquid meniscus relaxes back to its initial shape. The cycle is then repeated in what is known as the pulsating mode. An increase in the electric field causes an increase in the pulsating rate until a value of the field is reached when a single steady jet is formed, having a conical base at the capillary tip. A few centimeters below the capillary tip, the jet breaks up into a brush of monodispersed drops. This is referred to as the *stable cone-jet mod*e. A further increase in the electric field causes two or more jets to develop until finally many smaller, symmetrically arranged jets (*multi jet mode*) form at the rim of the capillary, producing a monodispersed cloud spray [23].

The three cited modes, dripping, cone-jet and multi jet, produce uniform size droplets that depend on many parameters; the first mode produces droplets about two orders of magnitude larger the other two modes [22].

Some of the parameters that affect the electrospray are the magnitude of the applied potential, the field geometry, the liquid flow rate and its physical properties, such as the electrical conductivity, viscosity, surface tension, and dielectric constant.

Traditionally electrospray were used with different organic solvents e.g. heptane, acetone, alcohols etc. Different kinds of vegetable oils have been successfully atomized. There are however very few reports of water being atomized effectively in the cone-jet mode using EHD. The high surface tension together with the high conductivity makes water very difficult to atomize using this technique. Stable cone-jet or multi jet is very difficult to obtain with tap or seawater and the windows of operation of electrosprays resulted very narrow [24].

Due to the low flow rate, electrospray is hardly to be considered an industrial device even if industrialized application exists [25]; commonly application of the electrospray are instead related to the generation of highly dispersed micro and nanoparticles, for ink-jet printing, paint spraying, fuel atomization, ion sources in mass spectrometer.

II.2.1.1.1.Droplet dynamic and evaporation modeling

The evaporation (or condensation) of droplets can be described coupling complex nonlinear equation for momentum, energy and mass transfer. Apart from the macroscopic complexity of the flow field, the traditional modeling approach for such flows generally requires to specify the governing equations for a single, isolated droplet including drag, convective heat transfer, mass transfer and effects due to finite droplet Reynolds numbers.

Evaporation of a single drop was described by Miller *et al.* [26]. They achieved good experimental results applying theoretical models based on Langmuin-Knudsen formulation, both at equilibrium and non-equilibrium state.

For a single evaporating droplet, the momentum exchange with the carrier gas is assumed to be only a function of the drag force. Furthermore, the thermal energy

exchange between phases is assumed to occur only through convective heat transfer. Internal droplet vortical flow is neglected. Under these conditions, the generic Lagrangian equations describing the transient position (X), velocity (v_i), temperature (T_d) and mass (m_d) of a single uncharged droplet are:

$$\frac{dX_i}{dt} = v_i \tag{II-2}$$

$$\frac{dv_i}{dt} = \left(\frac{f_1}{\tau_d}\right)(u_i - v_i) + g \tag{II-3}$$

$$\frac{dT_d}{dt} = \frac{f_2 Nu}{3Pr}\left(\frac{\theta_1}{\tau_d}\right)(T_G - T_d) + \left(\frac{L_V}{C_L}\right)\frac{\dot{m}_d}{m_d} - H_{\Delta T} \tag{II-4}$$

$$\frac{dm_d}{dt} = -\frac{Sh}{3Sc_G}\left(\frac{m_d}{\tau_d}\right)H_M \tag{II-5}$$

Where dm_d/dt is negative for evaporation, u_i and T_G are the local carrier gas velocity and temperature respectively, g is gravitational acceleration, L_V is the latent heat of evaporation. The ratio between the gas heat capacity (constant pressure) and that of the liquid phase is $\theta_1=C_G/C_L$. The Prandtl and Schmidt numbers of the gas phase in terms of the viscosity (μ), thermal conductivity (k_g) and binary diffusion coefficient (D_w) are $Pr_G=\mu C_G/k_G$ and $Sc_G=\mu/\rho D_w$ (with gas density ρ), respectively, $\tau_d=\rho_d D^2/(18\mu)$ is the droplet time constant for Stokes flow, where D is the droplet diameter and f_1 is a correction to Stokes drag for droplet motion and evaporation.

Furthermore, f_2 is a correction to heat transfer due to evaporation, Nusselt (Nu) and Sherwood (Sh) numbers are empirically modified for convective corrections to heat and mass transfer, respectively. Finally, $H_{\Delta T}$ represents some additional terms used to incorporate non-uniform internal temperature effects (i.e. finite liquid thermal conductivity) and H_M represents the specific driving potential for mass transfer (analogous to T_G-T_d for heat transfer).

The equations (II-2) and (II-5) can be solved under specific assumptions and simplifications that are representatives of the different models for the calculation of f_2, $H_{\Delta T}$ and H_M. These are summarized in Table II-1.

Model	Name	f_2	$H_{\Delta T}$	H_M
M1	Classical rapid mixing[1]	1	0	$ln[1+B_{M,eq}]$
M2	Abramson-Sirignano[2]	$\frac{-\dot{m}_d}{m_d B_T'}$	0	$ln[1+B_{M,eq}]$
M3	Mass analogy Ia	1	0	$B_{M,eq}$
M4	Mass analogy Ib	$(1+B_T)^{-1}$	0	$B_{M,eq}$
M5	Mass analogy IIa	1	0	$(Y_{s,eq}-Y_G)$
M6	Mass analogy IIb	$(1+B_T)^{-1}$	0	$(Y_{s,eq}-Y_G)$
M7	Langmuir-Knudsen I	G	0	$ln[1+B_{M,neq}]$
M8	Langmuir-Knudsen II[3]	G	$\frac{2\beta}{3P_{rG}}\left(\frac{\theta_1}{\tau_d}\right)\Delta_s$	$ln[1+B_{M,neq}]$

Table II-1: Expressions for the evaporation correction (f_2), internal temperature gradient correction ($H_{\Delta T}$) and mass transfer potential (H_M) from various models [26]

The nomenclature used in is as follows: Y is the vapor mass fraction (Y_G refers to the free stream vapor mass fraction away from the droplet surface), the subscripts *eq* and *neq* stay for "equilibrium" and "non-equilibrium". Transfer numbers for mass (B_M) are defined as:

$$B_{M,eq} = \frac{Y_{s,eq} - Y_G}{1 - Y_{s,eq}} \tag{II-6}$$

$$B_{M,neq} = \frac{Y_{s,neq} - Y_G}{1 - Y_{s,neq}} \tag{II-7}$$

Transfer number for energy (B_T) is:

$$B_T = (T_G - T_d)\frac{C_{p,V}}{L_V} \tag{II-8}$$

[1] Properties are evaluated using the "1/3" rule for reference mass fraction.
[2] Properties are evaluated using the "1/3" rule for reference mass fraction.
[3] An additional equation for $\Delta_s = T_{d,s} - T_d$ is required.

Each model requires the knowledge of the mass fraction of the vapor at the droplet surface. This is obtained for models M1-M6 using the equilibrium assumption:

$$Y_{s,eq} = \frac{\chi_{s,eq}}{\chi_{s,eq} + (1 - \chi_{s,eq})\theta_2} \tag{II-9}$$

Where $\theta_2 = M_g/M_w$ is the ratio of molecular weights; the surface equilibrium mole fraction of the vapor ($\chi_{s,eq}$) is related to the saturation pressure P_{sat} through the Clausius-Clapeyron equation (for constant latent heat):

$$\chi_{s,eq} = \frac{P_{sat}}{P_G} = \frac{P_{atm}}{P_G} exp\left[\frac{L_V}{R/W_V}\left(\frac{1}{T_B} - \frac{1}{T_d}\right)\right] \tag{II-10}$$

Where T_B is the liquid phase normal boiling temperature and R is the universal gas constant. Non-equilibrium surface mass fractions are used for the Langmuir-Knudsen models (M7 and M8).

The classical evaporation model (model M1) was first derived by Godsave [27] and Spalding [28] and has received great attention since its introduction over 40 years ago. This model, also referred to as the "D^2 law", was originally derived assuming a constant droplet temperature fixed at the wet bulb condition. It included the quasi-steady assumption for the gas phase leading to the logarithmic form for the mass transfer potential, H_M. Since its introduction, the importance of transient droplet heating has been recognized [29] and the evaporation rate is now generally coupled with a time dependent energy equation typically with assumed infinite thermal conductivity of the liquid [30]. In this form, the classical model is generally referred to either the infinite conductivity model or the rapid mixing model.

It is worth noticing that the model reported for droplet evaporation is valid for uncharged droplets; if the interactions due droplet charges are important (or also because the droplet are immersed in a charged particle cloud), additional terms should be considered in equation to take into account the acceleration related to columbic forces between droplets. Therefore the dynamic of charged droplets result a very hard

problem; in this case, a CFD code must be used in order to resolve a complex system of differential equations.

In addition, when charged droplets evaporate, they can undergo an "electrostatic" explosion. In fact, during the falling, the droplet starts to evaporate losing water molecules, but not charge. As a result, the surface charge density increases to a point at which the force of Coulomb repulsion at the surface overcomes the cohesive force of surface tension, at which point the droplet distorts and emits jets of small, highly charged progeny droplets in a process called Coulomb fission or Rayleigh discharge. Charged droplets generally undergo Rayleigh discharge while they are at 70-120% of their Rayleigh limit of charge [31].

A parameter that can affect the evaporation rate of charged droplets is their shape; in fact highly charged drops develop a pronounced oblate distortion caused by the charge density enhancement at their waist where the drop curvature is maximum [32, 33]. Since the surface electric stress caused by the charge opposes to the surface tension force of the drop, the effect of drop charge is to enhance its oblateness, increasing the mean value of drop's major axis around which it oscillates. This causes an increase in the cross sectional area of the charged drop exposed to the airflow which alters the gas fluid dynamic field around the drop surface with a consequently modification of the evaporation rate respect to a spherical uncharged droplet. In fact, the forced convection mechanism is not able to operate efficiently over the entire surface of the oblate drop and, therefore, evaporation rate will slightly decrease with the increasing of the drop oblateness. For example Bhalwankar et al [34] showed that the radius of a drop falling from 2 km height in an atmosphere of 70% relative humidity has to be of 1.07mm if uncharged and 1.037mm if charged at 10^{-10}C, to reach the ground with 1.00mm radius. Differences in the evaporation rates of charged and uncharged droplet in this case is around 3.1%.

II.2.1.2. Particle charging mechanisms

The principal mechanisms by which aerosol particles acquire charge are *flame charging*, *triboelectrification*, *diffusion charging*, and *field charging* [35].

Flame charging occurs when particles are formed or pass through a flame. At the high temperature of the flame, direct ionization of gas molecules creates high concentrations of positive and negative ions that can be acquired by particles. The net charge acquired by the particles depends on the material and the charge distribution and is usually symmetric with respect to polarity (equal numbers of positive and negative charges). Triboelectrification makes particles charged by mechanical action. This charging mechanism can produce highly charged particles under optimized circumstances, but is not feasible for aerosol charging.

Particles can become unipolar charged in presence of ions by random collisions between ions and particles. This process represents a *diffusion charging* mechanism, because the collisions result from the Brownian motion of the ions and particles. This mechanism does not require an external electric field and, to a first approximation, does not depend on the particle material. As the charge accumulates on the particle surface, they produce a field that tends to repel additional ions, reducing the charging rate. An expression to evaluate the charge acquired by a particle d_p by diffusion charging during a time t_R is [35]:

$$q_{diff} = \frac{d_p k_b T}{2\, K_e e}\, ln\left[1 + \frac{\pi K_e d_p c_i e^2 N_i t_r}{2 k_b T}\right] \qquad \text{(II-11)}$$

Where N_i is the ions concentration. At standard conditions, for $Ni \cdot t_r > 10^{12}$ s·m^{-3} this equation is accurate to within a factor of two for particles from 0.07 to 1.5 µm; for $Ni \cdot t_r > 10^{13}$ the equation is accurate to a factor of two for particles from 0.05 to 40µm [35].

Differently, if the particles are immersed in an electric field, it can be bombarded by ions in a process called *field charging*. In this charging mechanism the uncharged

spherical particle is able to distort the electromagnetic field as shown in Figure II-2/A. All ions moving on the field line intersecting to the left of the particles will collide with the particle and transfer their charge to it. As the particle becomes charged, it will tend to repel the incoming ions, as shown in Figure II-2/B. The presence of charges on the particle reduces the field strength and the number of field lines converging on the particle. Finally, the charge builds up to the point where no incoming field lines converge on the particle (Figure II-2/C) and no ions can reach the particle. At this condition the particle reach a saturation charge.

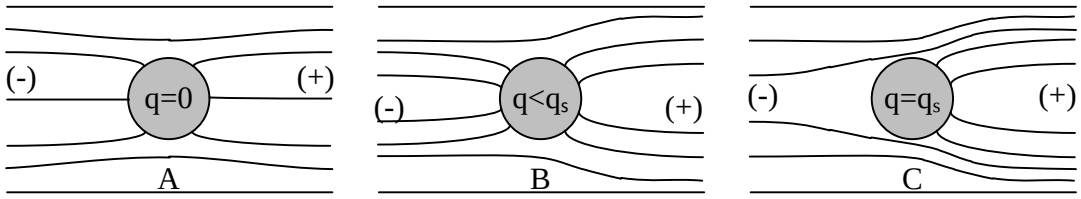

Figure II-2: Electric field lines for a conducting particle in a uniform field

An expression to evaluate the charge acquired by a particle d_p under this mechanism, is:

$$q_{field} = \frac{q_s \left(\frac{t_r}{\tau}\right)}{1 + \frac{t_r}{\tau}} \tag{II-12}$$

where:

$$q_s = 12\,\pi\varepsilon_0 \left(\frac{d_p}{2}\right)^2 E_{el} \frac{\varepsilon_r}{\varepsilon_r + 2} \tag{II-13}$$

and:

$$\tau = \frac{4\,\varepsilon_0}{N_i e Z_i} \tag{II-14}$$

E_{el} is the electric field in which the particle travel and q_s represents the saturation limit called Pauthenier limit.

Field and diffusion charging are usually the most effective and significant mechanisms to charge particles in a gas stream. Usually their contributions can be summed to determine the actual particle charge. However, it is worth noting that the charge

acquired by a droplet is proportional to d_p^2 in field charging and to d_p in diffusion charging, so field charging is the dominant mechanism for particles larger than 1.0µm, while diffusion charging prevails for particles finer than 0.1µm, even in presence of an electric field. It is assumed that the charge acquired by particles in an electric field is sum of the two contributes:

$$q_p(d_p) = q_{diff} + q_{field} \tag{II-15}$$

An example of the charge acquired by particles in the range 10-10000nm are reported in Figure II-3.

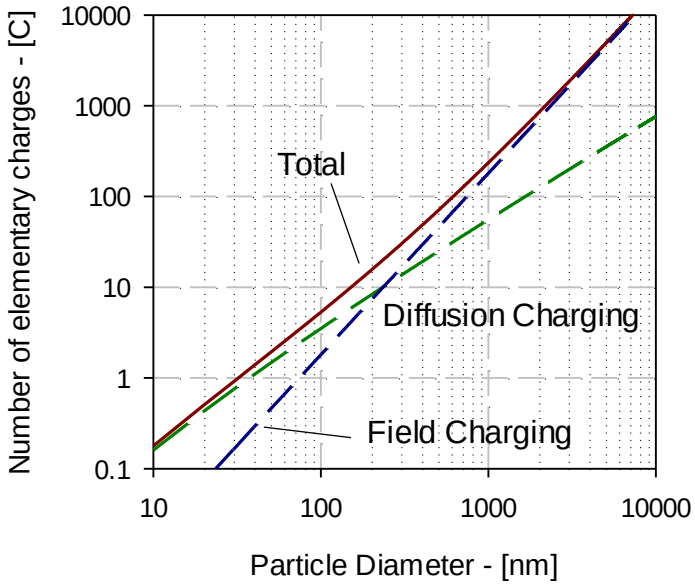

Figure II-3: Example of field and diffusion charging at t_r= 46ms and $N_i=4\cdot10^{13}m^{-3}$

Several other particle charging models have been proposed in the past. For example, Liu et al. [36, 37] and Lawless [38] have presented numerical models taking into account the effects of diffusion, field, and combined charging, thus applicable for predicting electrical charge on the particles of all sizes. These models showed reasonable agreement with the experimental results but they need to be solved numerically with complex resolution and do not have analytical solutions. For

practical application, the proposed equations (II-15) allow a reliable description of charging processes.

II.2.1.2.1.Corona discharge

The field and diffusion charging described before require high concentration of unipolar ions to take place. Because of the mutual repulsion and high mobility of these ions, their lifetime is short, so they must be continuously produced to charge particles effectively. Ions can be created in air by radioactive discharge, ultraviolet radiation, flames and corona discharge; but only the latter can produce unipolar ions at concentration high enough to be useful for aerosol charging.

To produce a corona discharge, one must establish a non-uniform electrostatic field, such as that between a needle and a plate or between a concentric wire and a tube. Air and other gases are normally very good insulators, but in a region of sufficiently high field strength, they become conductive. This mechanism occurs when the magnitude of the applied electric field is high enough to accelerate the free electrons. When free electrons attain sufficient velocity, they collide with neutral gas molecules ionizing them. Ionization occurs when the force of the collision removes an electron from the gas molecule, resulting in a positively charged gas molecule and another free electron (see Figure II-4). These newly free electrons are also accelerated and cause additional ionization. A particle that travels in this ionization zone at high ion concentration acquires a charge according to the diffusion and field charging mechanisms.

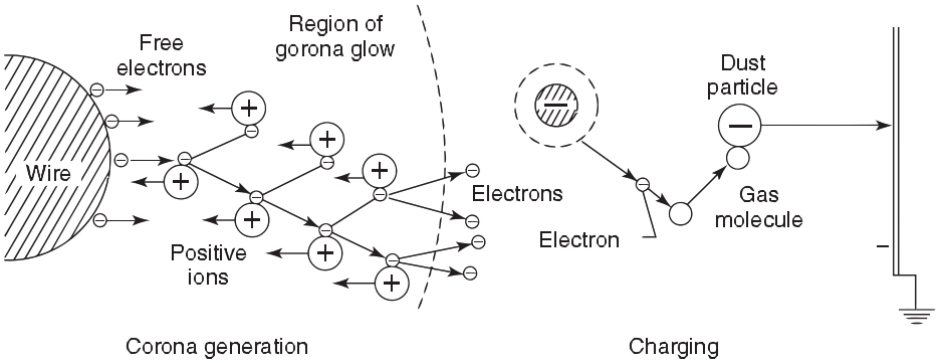

Figure II-4: Basic process involved during corona charging

Corona discharge is at the basis of electrostatic precipitators that exploit this mechanism to charge particles letting them to migrate from the bulk phase of the gas stream toward the grounded surface, where they are eventually collected.

Corona discharge can be positive and negative, with quite different properties and appearances. With positive corona, the entire region around the wire has a stable, glowing sheath with a characteristic bluish-green color. With negative corona, the corona glow exists in tufts or brushes that appear to be in a dancing motion over the surface of the wire. These tufts may be several millimeters in length. In this system there is sufficient energy in the corona region to produce ozone from oxygen. However, industrial negative corona produces about 10 times as much ozone as a positive corona. Indoor and recirculating electrostatic precipitators use positive corona for this reason. Industrial electrostatic precipitators usually use negative corona, because they can be operated at higher voltages and thereby achieve higher efficiencies.

II.2.1.2.1.1. Corona discharge for a wire-tube geometry

In the case of a wire at high voltage inserted coaxially in a grounded tube, the field strength required to initialize the corona discharge depends on the wire diameter d_w and can be evaluated by a modification of well-known Peek's formula [39]:

$$E_0 = 31.02 \cdot 10^5 \cdot \beta \cdot \delta \left(1 + \frac{0.0308}{\sqrt{\mathrm{d}_w/2 \cdot \delta}}\right) \qquad \text{(II-16)}$$

Where β is the dimensionless surface roughness of electrode and δ is the air relative density. For $E_{el} > E_0$, the electric field at a point r from the axis of the wire, assuming that the space charge effect is negligible, is given by the relation [40]:

$$E_{el} = \frac{V_a}{r\ ln\left(\frac{d_t}{d_w}\right)} \qquad \text{(II-17)}$$

Where V_a is the voltage applied to the wire and d_t is the diameter of the grounded cylinder.

The equation represents a hyperbole that approach high values, up to infinity, only near the wire ($r \approx d_w/2$). For $d_w < r < d_t$, the value of E_{el} is quite constant; it is therefore possible to consider a mean value of the electric field as:

$$\overline{E_{el}} = \frac{\int_{d_w/2}^{d_t/2} \frac{V_a}{r\, ln\left(\frac{d_t}{d_w}\right)} dr}{(d_t - d_w)/2} \tag{II-18}$$

The ion concentration in the electric field can be determined from the conservation of current, given by the equation [41]:

$$N_i = \frac{I}{e\, Z_i \overline{E_{el}}\, \pi\, L\, d_t/2} \tag{II-19}$$

Where I represents the current supplied to the wire, which is very simple to measure. Anyway, a semi-empirical relation for an estimation of I is reported in the literature [42] and is expressed as:

$$I = A\, V_a (V_a - V_0) L \tag{II-20}$$

$$A = \frac{32\, \pi\, \varepsilon\, Z_i}{{d_t}^2 ln\left(\frac{d_t}{d_w}\right)} \tag{II-21}$$

Where ε is air dielectric constant (or air permittivity) that can be considered the same of the vacuum permittivity, ε_0 , up to about 500K and for any water vapor concentration [43].

II.2.1.2.2. Back Corona

Back corona, or reverse ionization, describes the conditions where an electrical breakdown occurs in a corona discharge. Its presence inside of an electrostatic precipitator is usually associated to a threshold in the resistivity of the particle layer deposited on the plates.

In a typical electrostatic precipitator configuration, a negative applied voltage between the emitter electrode and a collecting electrode produce a negative glow-corona discharge at the emitter electrode. The negative ions exiting the glow corona discharge together with the charged particles drift towards the collecting electrode.

If the glow-corona discharge, when current and layer resistivity are high enough, a positive back-corona discharge is formed in the layer. From the dust layer positive ions exit the back-corona discharge and drift towards the emitter electrode discharging previously charged negative dust particles. Besides positive ions may attach to neutral dust particles, causing their drift backwards to the emitting electrodes. Back corona impose an upper limit to the voltage at which a corona discharge can be operated; the explanation for these phenomena is beyond the scope of this dissertation and, more details can be found, for example, in the book by H. J. White. [44].

II.2.1.2.3. Dynamic of charged particle in a wire-tube geometry corona discharge

When a charged particle carried by a gas flows through an electric field between a wire and a grounded tube, it is subject to an electric force direct radially to the wire and to a drag force direct along the axis of the tube in opposite direction to the electric force.

From a force balance along radial coordinate, the terminal velocity can be calculated as:

$$v_t = \frac{q_p \, \overline{E_{el}} \, C_c}{3 \, \pi \, \mu \, d_p} \qquad \text{(II-22)}$$

If the particle remains in the tube for a sufficient time, it can reach the wall and then be captured. In a period dt all particles within a distance $v_t \, dt$ from the tube wall will be removed. The fraction of particles removed during this period, dN/N, is the negative ratio between the area of the annulus, $\pi d_t v_t dt$, and the total cross –sectional area of the tube, $\pi \, d_t^2/4$, and is given by:

$$\frac{dn}{n} = -\frac{4\pi d_t v_t dt}{\pi\, {d_t}^2} = -\frac{4 v_t dt}{d_t} \qquad \text{(II-23)}$$

Integrating the equation with the condition $N(t=0)=N_0$, gives:

$$\frac{n(t)}{n_0} = exp\left(-\frac{4 v_t}{d_t} t\right) \qquad \text{(II-24)}$$

By substituting the expression of the particle residence time $\pi d_t 2L/4Q$, it results:

$$1 - \eta_c = \frac{n(t)}{n_0} = exp\left(-\frac{\pi\, d_t L\, v_t}{Q}\right) \qquad \text{(II-25)}$$

The equation is commonly called Deutsch-Anderson equation [45] and is the basis scaling equation for electrostatic precipitators.

II.2.1.3. Particle capture due to droplets

While a drop falls through a particle-laden gas, it collides with aerosol particles and can collect them. As the droplet falls, it sweeps (per unit time) the volume of a cylinder equal to $\pi\, D^2\, U_d / 4$, where U_d, is its falling velocity and D its diameter. As a first approximation, one would be tempted to conclude that the droplet would collect all the particles that are in this volume. Actually, if the aerosol particles have a diameter d_p, a collision will occur if the center of the particle is inside the cylinder with diameter $D + d_p$. Also, the particles are themselves moving with a velocity $u(d_p)$. So the "*collision volume*" per time becomes $\pi\, (D + d_p)^2\, |\, U_d(D) - u(d_p)|\, /\, 4$.

The relative velocity $|\, U_d(D) - u(d_p)|$ in the collision volume is valid when the particles flow parallel to the falling droplets; if the trajectories of particles and droplets are not parallel, the module of the relative velocity must be considered.

The *total collision efficiency* $E(D, d_p)$ is commonly introduced to indicate the fraction of particles of diameter d_p contained within the collision volume of a drop with a diameter D that are actually collected. Thus $E(D, d_p)$ can be viewed as a correction

factor accounting for the "active" interactions between the falling drop and the aerosol particle.

If $n(d_p)$ is the concentration of the particle of diameter d_p, the number of active collisions between particles of this diameter and one drop of diameter D is

$$\frac{\pi}{4}\left(D + d_p\right)^2 \left|U_d(D) - u\left(d_p\right)\right| E\left(D, d_p\right) n(d_p) \qquad \text{(II-26)}$$

When the entire ensemble of sprayed droplets is considered, the total rate of collection of all particles of diameter d_p is obtained integrating eq. (II-26) over the droplet number concentration and size distribution $\Psi(D)$

$$n|_{d_p} = n(d_p) \int_0^\infty \frac{\pi}{4}\left(D + d_p\right)^2 \left|U_d(D) - u\left(d_p\right)\right| E\left(D, d_p\right) \Psi(D)\, dD \qquad \text{(II-27)}$$

Hence, the scavenging rate of aerosol particles of diameter d_p can be written as

$$\frac{dn(d_p)}{dt} = -\Lambda\left(d_p\right) n(d_p) \qquad \text{(II-28)}$$

Where $\Lambda\left(d_p\right)$ is called *scavenging coefficient* and is the integral in the equation eq. (II-27); considering an initial value of particle concentration $n(d_p, 0)$, the integration over the time t of the eq. (II-28) gives:

$$n(d_p, t) = n\left(d_p, 0\right) e^{-\Lambda\left(d_p\right) t} \qquad \text{(II-29)}$$

Therefore, collection efficiency for the particle diameter d_p, that remaining in the reactor for a time equal to t_p, can be written as:

$$\eta\left(d_p\right) = \frac{n\left(d_p, 0\right) - n\left(d_p, t_c\right)}{n\left(d_p, 0\right)} = 1 - e^{-\Lambda\left(d_p\right) t_p} \qquad \text{(II-30)}$$

II.2.1.3.1.Collisional mechanisms

The *total collisional efficiency* $E(D,d_p)$ is, by definition, equal to the ratio of the total number of collisions occurring between droplets and particles to the total number of particles in the collision volume swept out by a falling drop. A value of $E = 1$ implies

that all particles in the geometric volume will be collected. Usually $E < 1$, although E can exceed unity under certain conditions (as, for example, for the electrical interactions). The evaluation of the total collisional efficiency starts to the evaluation of the fundamentals interactions between droplet and particles. These interactions can vary in functions of many variables like their dimensions, the charge carried, the temperature and humidity in the environmental or the droplet-particle relative velocity.

To better understand the concept of the collisional efficiency, a description of the basic physics of droplet-particle interactions is required.

In order to remove suspended particles from a gas, this must pass through a zone in which the particles, under the influence of one or more active "collecting" forces, would be diverted from the flow direction of the stream. The particles must remain under the influence of the collecting forces for a time sufficient to be diverted toward some collecting surfaces and, eventually, being removed from the gas [46]. During scrubbing, the forces are originated from the interactions between falling droplets (the collectors) and particles and there are six major particle collection mechanisms of particle collection by water droplets each of which corresponds to a the effect of different physical phenomena and to a particular collisional efficiency:

1. **Inertial impaction E_{In}** [46-48];
2. **Directional interception E_{DI}** [46, 47, 49];
3. **Brownian diffusion E_{BD}** [47, 49];
4. **Electrostatic interactions E_{Es}** [50-52]
5. **Thermophoresis E_{Th}** [50, 53];
6. **Diffusiophoresis E_{Dph}** [50, 53].

The *Total collision efficiency*, *E*, is usually considered the sum of these collisional efficiencies deriving from different contributions, whose properties will be briefly described as follows:

1. **Inertial impaction**. Inertial impaction occurs when the gas direction changes around a droplet. Fine particles have less inertia and are more likely to be carried by

the gas flow, while coarse particles depart from the gas streamlines and continue straight on towards the droplet.

2. **Directional interception**. Direct interception occurs when the fluid streamlines, carrying the particle, pass within one-half of a particle diameter than the droplet surface; therefore, the particles can touch the droplet surface and can be captured.

3. **Brownian diffusion**. Brownian diffusion capture takes place when random movements of the particles push them toward the droplets.

4. **Electrostatic interactions**. Electrostatic attractions occur because the particle, the droplet, or both possess sufficient electrical charge to overcome the inertial forces; than the particle can be attracted by the droplet and collected. If only droplets or particles are charge, the electrostatic forces are also present due to image forces.

5. **Thermophoresis**. Thermophoretic capture takes place when a thermal gradient between gas and water exist. The hot molecules of air have higher kinetic energies and higher momentum than those in colder areas. Therefore, the molecules colliding with the particle from the "hot" side of the particle will exert a greater force than those on the "cold" particle side. As a result of these forces, a particle moves away from the high-temperature area and toward colder gas temperatures. If the drops are colder than the gas, the thermal gradient promotes the thermophoresis of particles from the bulk of the gas phase to the cold particle surface.

6. **Diffusiophoresis**. Diffusiophoresis occurs in presence of a gradient of gas molecule concentration. Diffusiophoresis is the net particle motion resulting from non-uniformities in the gas molecules of the suspending gas. It includes Stephan flow plus movement in the direction of the heavier or more concentrated gas molecule. It is caused by the differences in molecular impacts on opposite sides of the particles. The Stephan flow portion of diffusiophoresis results from the flow of gas molecules toward or away from the surface of a volatile liquid in the gas medium as a result of condensation or evaporation respectively. Stephan flow

results in gas molecule and hence particle movement, toward a liquid during condensation and away during evaporation. This suggests that positive diffusiophoresis exists when particles to be collected in the presence of liquid droplets exist in a saturated and cooled gaseous medium. Hot dry gases develop a negative phoretic force; the water evaporation pushes particles away from the collector.

Schematic diagram of these collection mechanisms and the main models are show in Figure II-5.

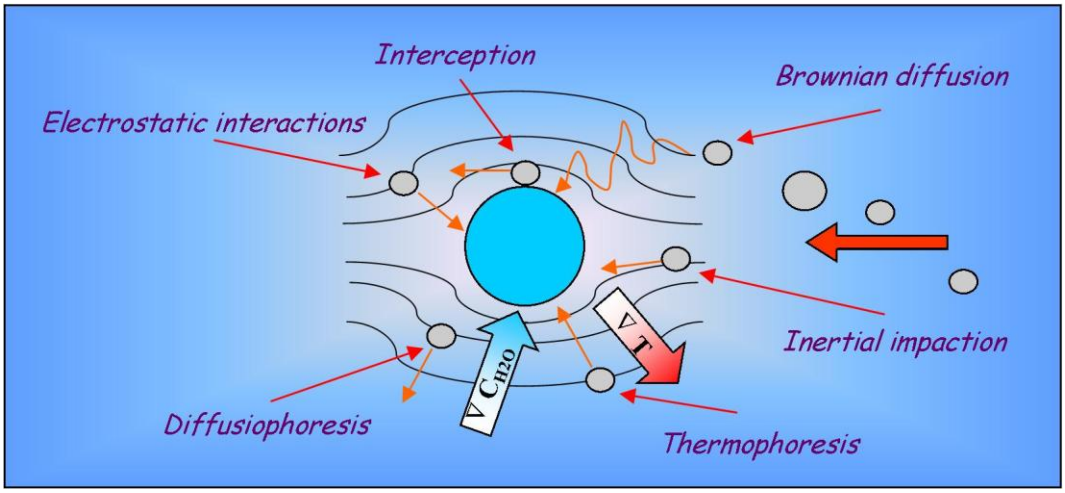

Figure II-5: Schematic diagram showing the particle collection mechanisms by a water droplet

Collisional efficiencies were calculated by several authors in the past. Table II-2 resume main equation presented in the pertinent literature.

INERTIAL IMPACTION, E_{In}

$$E_{In} = \left[\frac{St - St^*}{St - St^* + 2/3}\right]^{\frac{3}{2}} \left(\frac{\rho_p}{\rho_w}\right)^{\frac{1}{2}} \quad \text{(II-31)}$$

$$St = \frac{C_c \rho_p d_p^{\,2} U}{18 \mu D} \quad \text{(II-32)}$$

Slinn 1983 [47]

$$St^* = \frac{1/2 + 1/12 \cdot \ln[1 + \mathrm{Re}]}{1 + \ln[1 + \mathrm{Re}]} \quad \text{(II-33)}$$

$$E_{In} = \left[\frac{St}{St + 0.35}\right]^2 \quad \text{(II-34)}$$

Licht 1988 [46]

$$E_{In} = 3.4 St^{\frac{3}{5}} \quad \text{at} \quad St \le 0.5$$
$$E_{In} = 1 \quad \text{at} \quad St > 0.5 \quad \text{(II-35)}$$

Kim, et al. 2001 [48]

DIRECTIONAL INTERCEPTION, E_{DI}

$$E_{DI} = 4H\left[\omega^{-1} + \left(1 + 2\,\mathrm{Re}^{1/2}\right)H\right] \quad \text{(II-36)}$$

$$\omega = \frac{\mu_w}{\mu} \quad \text{(II-37)}$$

Slinn 1983 [47]

$$H = \frac{d_p}{D} \quad \text{(II-38)}$$

$$E_{DI} = \frac{(1-\alpha)}{(J + \omega K)}\left[\left(\frac{H}{1+H}\right) + \frac{1}{2}\left(\frac{H}{1+H}\right)^2 (3\omega + 4)\right] \quad \text{(II-39)}$$

$$J = 1 - \frac{6}{5}\alpha^{\frac{1}{3}} + \frac{1}{5}\alpha^2 \quad \text{(II-40)}$$

$$\omega = \frac{\mu_w}{\mu} \quad \text{(II-41)}$$

Jung and Lee 1998 [49]

$$K = 1 - \frac{9}{5}\alpha^{\frac{1}{3}} + \alpha + \frac{1}{5}\alpha^2 \quad \text{(II-42)}$$

$$H = \frac{d_p}{D} \quad \text{(II-43)}$$

BROWNIAN DIFFUSION, E_{BD}

$$E_{BD} = \frac{4}{\mathrm{Re}\,Sc}\left[1 + 0.4\,\mathrm{Re}^{\frac{1}{2}} Sc^{\frac{1}{3}} + 0.16\,\mathrm{Re}^{\frac{1}{2}} Sc^{\frac{1}{2}}\right] \quad \text{(II-44)}$$

Slinn 1983 [47]

$Sc = \frac{\mu}{\rho D_{BR}}$		(II-45)	
$D_{BR} = \frac{k_B C_c T}{3\pi\mu d_p}$		(II-46)	
ELECTROSTATIC INTERACTIONS, E_{Es}			
$E_{Es} = \frac{16K_c C_c q \cdot q_p}{3\pi\mu U D^2 d_p}$	For droplet and particles charged	(II-47)	Davenport and Peters 1978 [50]
$E_{Es,CD} = \left\{ \frac{15\pi}{8} \left(\frac{\varepsilon_p - 1}{\varepsilon_p + 2} \right) \frac{2C_c \left[q/(\pi D^2) \right]^2 d_p^2}{3\pi\mu_g U \varepsilon_0 D} \right\}^{0.4}$	Image force for Charged Droplet	(II-48)	Nielsen and Hill 1976 [51]
$E_{Es,CP} = 2.89 \left\{ \frac{C_c q_p^2}{3\pi^2 \mu_g U \varepsilon_0 D^2 d_p} \right\}^{0.353}$	Image force for Charged Particles	(II-49)	Nielsen and Hill 1976 [51]
THERMOPHORESIS, E_{Th}			
$E_{Th} = \frac{4a\left(2 + 0.6\,\mathrm{Re}^{\frac{1}{2}} \mathrm{Pr}^{\frac{1}{3}} \right)(T - T_{as})}{UD}$		(II-50)	Davenport and Peters 1978 [50]
$a = \frac{2C_c(k_g + 5Kn \cdot k_p)k_g}{5P(1+6Kn)(2k_g + k_p + 10Kn \cdot k_g)}$		(II-51)	
DIFFUSIOPHORESIS, E_{Dph}			
$E_{Dph} = \frac{4b\left(2 + 0.6\,\mathrm{Re}^{\frac{1}{2}} Sc_w^{\frac{1}{3}} \right)\left(\frac{P_w^{\circ}(T)}{T} - \frac{P_w^{\circ}(T_{as})}{T_{as}} RH \right)}{UD}$		(II-52)	Davenport and Peters 1978 [50]
$b = \frac{T D_w}{P} \sqrt{\frac{M_w}{M_g}}$		(II-53)	

Table II-2: Models for collisional efficiencies

The electrostatic collisional mechanism was first studied by Kraemer and Johnstone [54]. They solved a numerical model for the deposition of charged aerosol from a moving stream on spherical charged and fixed collector (a metal sphere). Aerosol concentration was measured by weight, the aerosol distribution were not reported. The results obtained was verified experimentally; they show that collection by the

electrostatic mechanism is enhanced by increased times of retention in the dust collection equipment and by lower relative velocities between the aerosol and the collecting surfaces. They concluded that the optimum design of equipment utilizing electrostatic forces, requires lower velocities than those in which the inertial collection is predominant. Barlow and Latham [55] in 1983 focused their attention on the submicron particulate range. They measured the collisional efficiency between a water aerosol cloud in the range of 0.3-2µm and 37 droplets (radius 270-660µm) with charge of 10^{-14}-10^{-11}C. The comparison with scientific literature allowed the authors to understand that collisional efficiency of every droplet increased with its charge (almost apart from the polarity) and it was two orders of magnitude higher than collisional efficiency without charge. Nevertheless, experimentation was lacking in theoretical foundations, therefore it was impossible to achieve a general conclusion.

II.2.2. Main theoretical and experimental results on particle abatement in wet electrostatic scrubbers

In the early 1940's, an electrostatic droplet spray scrubber consisting of electrically charged water droplets collecting aerosol particles charged to the opposite polarity was proposed by Penney [56]. He patented an electrified liquid spray dust precipitator involving particle charging by corona discharge and droplet charging by either corona or induction discharge. The system consisted in a scrubber chamber of 6 ⅜ inches diameter and about 24 inches length. Water loading was of about 0.7 liters per cubic meter of gas, and was obtained with a single spray nozzle charged at 9-10 kV. Particles were charged with a corona wire in a 3 inches diameter metal cylinder. Penney reported that the dust collection efficiency increased from 13.8%$_w$ to 44.8%$_w$ by charging the particles and droplets with opposite polarity.

In 1974 Pilat et al. [57] used a double chamber electrostatic droplet spray scrubber able to work with air flow rates up to 230 m^3/h. The first chamber was counter-current and was operated with a water flow of 4.5 L/min sprayed by 20 nozzles. The second chamber was co-current and water flow rate was of 3.8 gal/min with 13 spray nozzles.

The spray nozzles were the Spraying Systems Fogjet 7N4 model. The water droplets were positively charged by induction with a 5 kV power supply. The droplets were about 50µm and were charged at specific charge of 0.56mC/kg. A dioctyl-phthalate aerosol, with size distribution between 0.3 and 4µm, was generated and charged by corona at 27 kV. Experiments were carried out measuring particle mass concentration and size distribution, droplet distribution and charge to mass ratio for both aerosol and spray. The results showed that the overall particle collection efficiency increased from 68.8%$_w$ for the uncharged conditions to 93.6%$_w$ for the charged.

Metzler et al. [58] in 1997 used a co-counter horizontal pipe scrubber with a diameter of 300 mm. The air flow rate ranged from 500 to 1800 m^3/h. Quartz particles, in a range of 0.5-3.5 µm, were fed in the chamber and charged by corona wire. Droplets were produced with an industrial nozzle and charged by induction. Particles abatement was measured at different operational conditions showing efficiency values up to 95% for particles of 3.5 µm, but only 45% for particles of 0.5 µm

Krupa et al. [59] estimated removal efficiency in a rectangular WES with a cross section of 160x160 mm. The particles were charged in a corona discharge while the droplet was produced by electrospray operating in the precession mode whit a volume mean size of about 80 µm. Fly ash from a last stage of an electrostatic precipitator of mean particle size lower than about 5 µm was used in the experiments. The experiments were carried out in three different charging configurations and for three different air flow rates. For negatively charged dust, and positively charged spray the collection efficiency was about 90%; for dust and spray charged positively, the collection efficiency was of about 85%; for dust uncharged and spray charged positively, the collection efficiency was not higher than 50%. Thus, the system, which used charge with opposite polarity for water and particulate, gave the best efficiency.

Balachandran et al. [60] studied smoke cigarette abatement in a batch chamber of about 6 m^3. The particle size distribution ranged from 0.5 to 2.5µm. The water droplets were generated by Newland Electric Atomizer and charged by induction at -8 kV.

Tests were carried out measuring the smoke suppression by means of light beam extinction method using a homemade optical system. It was shown that electrical charging of droplets significantly increases the efficiency of removal of smoke particles from about 40 to 90%.

In a later work Jaworek et al. [61] used the same experimental apparatus to study charged smoke cigarette abatement using a multi-nozzles electrospray system exerted in precession mode at +11 kV and -11 kV. This mode was chosen for experiments because the spray plume was very broad, and the droplets were in the size range between 60 and 110 μm. They had demonstrated that the electrical charging of droplets and smoke particles allows an increase of the removal efficiency of particles from a gas; the removal efficiency of smoke particles (smaller than 1 μm) can be as high as 80–90% at water consumption of about 50 ml/m^3

Cross et al. [21] utilized a cylindrical 'wind tunnel' reactor (D = 650mm) working with air velocity in the range 0.5 to 1.25 m s^{-1}. The droplets were produced by an air assisted nozzle (model SU22/42 series manufactured by Spraying Systems Co.) able to produce droplet size ranges from 20 to 400μm. The droplet were charged by induction up to 2kV reaching a charge in the range of 0.2 and 3 mC/kg. The water in a range of 2 and 8 mL s^{-1}, was sprayed cross-flow respect to the air. Coal dust where utilized as particles dispersed and carried to the air. Two particle size distributions were studied; the smaller particles distribution ranges from 1 to 7μm and were not charged. The results obtained showed that the droplet charge allows an increase of particle efficiency from $73\%_w$ to $86.5\%_w$. Based on their results, the authors identified general rules to increase the abatement efficiency, but these results are specific to the design utilized and are difficult to generalize.

Capture of particle emitted by a marine diesel engine was studied by Ha et al. [62]. Collection efficiency was experimentally measured in an electrostatic seawater spraying scrubber varying the engine load and the applied voltage to the charging induction spray in a range of 0-5kV. Their results show that if both particles and

droplets are charged of opposite polarity, the collection efficiency can reach values of about 93-95%$_w$.

Wang et al. [63] studied the dust deposition on a fixed collector. Only inertial impaction and electrostatic attraction was considered in the model. The problem was solved in a two-dimensional geometry. The experimental system consisted in a horizontal tube where a liquid monodispersed aerosol were produced and charged. The aerosol size were in the range of 2-50μm. A fixed and charged stainless-steel ball was used as collector. Five balls in the range of size of 2.31-6.34mm were used. The authors reported the results in terms of Stokes and Coulomb numbers as made by Adamiak et al [64] and Jaworek et al. [65]. The results obtained show a good agreement with experiment and theoretical data.

CFD simulations were performed by Adamiak et al [64] and Jaworek et al. [65]. They used a numerical algorithm to simulate dust particle deposition on a charged spherical collector. The algorithm was able to trace simultaneously the mutual movement of a charged droplet and a charged particle in three dimensions. They solved Navier-Stokes equations for a gas in laminar flow considering the Stokes drag, gravity and electrostatic forces. The results of simulation showed that the process was controlled by the Stokes (St), Coulomb (Co), and Reynolds (Re) numbers. They showed that for low St number and high Coulomb number the electric forces can significantly improve deposition; on the contrary, for high St number, the electric forces are negligible. The Re number, instead, in all cases had a secondary effect on particle deposition. In addition, the image forces were important only at very short distances between a particle and a droplet, and practically did not affect the shape of the precipitation space. The results obtained in this work were not verified experimentally.

Zhao and Zheng [66] modeled a cylindrical Wet Electrostatic Scrubber (diameter=6m, height=2m) considering Brownian diffusion, interception, inertial impaction and electrostatic forces. The authors used Monte Carlo approach for population balance modeling. The particle distribution considered range from 0.08μm to 10 μm, while

mean droplet size range from 0.5 to 1.5mm. The air and water flow rate was respectively 61072m^3/h and 3m^3/h. The temperature was fixed at 160°C and droplet evaporation was not considered. The droplet and particles charge were modeled on the basis of the field charging. The obtained results showed an increase of particle abatement for fine particles (<1μm) due to electrostatic forces.

Carotenuto et al. [67] used an analytical model to predict the maximization of particle removal efficiency in industrial Wet Electrostatic Scrubbers. The proposed model considered the overall collision efficiency as the result of inertial impaction, directional interception, Brownian diffusion, electrostatic interactions, thermophoresis, and diffusiophoresis. The work analyses the effect of different processes parameters: contact time, specific water consumption, water/gas relative velocity, size and charge of sprayed droplets. Moreover, the model has been validated by a comparison with different experimental data available in literature, both for charged and uncharged scrubbers. Then it is applied to a reference case study to obtain generalizable results. As regards micrometric particles, the model has shown that the collection efficiency increases for higher water/gas relative velocity, with a small effect of droplet diameter and a moderate increase with the droplet charge. On the contrary, for submicron particles, the water/gas velocity plays a secondary role in the capture mechanisms, while a substantial increase of collection efficiency has been observed by improving the droplet charge level and reducing the droplet size. With reference to the actual performances of water spraying and charging devices, the model predicts that a collection efficiency as high as 99.5% can be obtained reliably in a few seconds with a water consumption of 100ml/m^3 by adopting droplet diameters around 100μm and charge to mass ratio from 1 to 3mC/kg, corresponding to droplet charge equal to 10-30% of Rayleigh limit.

II.3. Considerations on literature results

From a critical review of the experimental and theoretical investigations reported in literature, the following consideration can be highlighted:

- Experimental investigations on WES processes are often executed on pilot-scale reactors with the use of spray nozzles that generally produce wide size and charge distributions. These approach provides results closer to industrial needs and allow to verify the effective increase of the efficiency due to electrostatic contributions, but the droplet size and charge distribution and the fluid dynamic of such reactors can be complex, due to the presence of stagnant zone or preferential pathways, resulting in a in very complex modeling of the wet electrostatic scrubbing process.
- In order to optimize the performance of WES reactor, an appropriate process modeling is essential to understand what are the main physical parameters that govern the particle collection and what are the best options to improve the particle capture efficiency.
- Experimental results on the mechanisms that govern the capture of particles by scrubbing droplets were executed under model conditions that are far from real industrial applications; a typical experimental system is the collection of a liquid aerosol (and so perfect spherical drop) on a fixed collector.
- Very few results are available for submicron particles. Moreover the measure of particle size distribution and concentration is often carried out in terms of mass concentration; this approach increase the effects the largest particles that are weighted to the third power of their diameter, so that submicron particle concentration is negligible and may even fall within the error of determination of the measure.
- Theoretical model on particle scavenging were generally not explicitly verified in the submicron range.

Based on these considerations, the next chapter introduces a new experimental methodology aimed to highlight the effects of the main physical properties involved in the wet electrostatic scrubbing on submicron particle capture. Experimental tests are therefore presented and discussed in details on the basis of theoretical models on wet electrostatic scrubbing available in the pertinent literature.

CHAPTER III - Materials and methods

The experimental methodology is based on the adoption of a lab scale WES device operated in controlled hydrodynamic conditions in order to evaluate the effects of specifics physical properties (like droplet charge, particle charge, etc.) on the WES particle capture efficiency.

The experimental setup consider the adoption of an electrospray (the charged droplet generator) operating in dripping mode to produce a train of droplets, with controlled size and charge, which scrubs the gas (produced by the combustion of an incense stick and purposely charged by corona discharge at opposite polarity then droplets) contained in a closed vessel. The use of a discontinuous unit instead of a continuous one, was related to the low number of droplets produced by the electrospray and to the low particle abatement velocity in the system. This aspect does not means that the particle capture velocity of a single droplet is slow, but simply that the water flow rate is not sufficient to achieve a total particle abatement compatible with a continuous reactor. This aspect can be better explained through the forthcoming experimental evidences. This approach requires the construction of a suitable experimental apparatus to generate a train of droplets and the particle-laden gas, and to measure the particle concentration in the reactor volume over the scrubbing time.

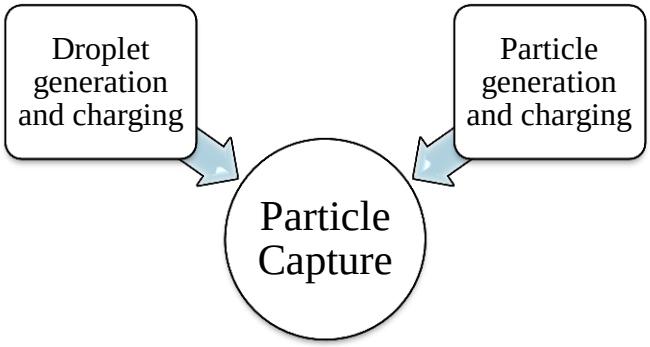

Figure III-1: Block diagram of the experimental approach

Due to the difficulties to make all these measurement during wet electrostatic scrubbing tests, the characterization of the physical properties of the charged droplet and charged particles, in particular in terms of size distribution and charge, need the development of specific experimental protocols and apparatus.

For this reason the experimental activity was carried out in three different steps in order to evaluate

- charge and size distribution of the drops;
- charge and size distribution of the particles;
- the particle abatement during the scrubbing time in the reactor due to the interactions between charged particles and droplets.

In the following the experimental rig, preliminary results and the experimental procedure are explained for the three experimental studies.

III.1. Experimental rig for droplet charge and size characterization

The droplet charging and spraying unit consists in a needle put coaxially to a grounded steel flat ring, encased in a PTFE box, with the tip at 1 mm below ring's lower surface. The needle is connected to a high voltage power supply device (Bertan mod. 230-20R). The assembly of the charged droplets generator is reported in Figure III-2.

Two needles were used in this study, one with a conical shape tip (hereafter simply called *conical needle*) that was purposely constructed by means of a precision lathe, and another flat shape tip (hereafter simply called *flat needle*); the dimensions of the needles are reported in Figure III-3

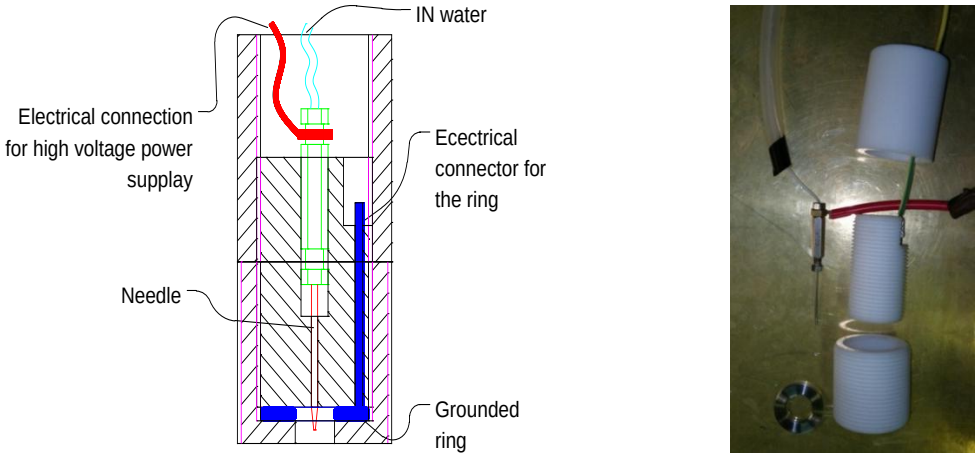

Figure III-2: Charged droplets generator assembly

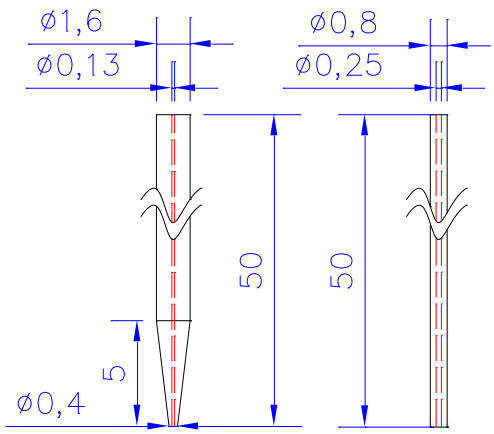

Figure III-3: Needle dimensions in millimeters

The liquid was fed into the needle using a Plexiglass® pressurized water tank. The tank pressure was monitored by a digital pressure gauge (Nordgren mod. 33D) with a precision of 1 mbar; the flow rate was monitored and adjusted with a rotameter (Rota Yokogawa mod. RAGK41) operating between 0.15 ml/min and 2.2 ml/min. The pressure in the tank can be set to a fixed value by a regulator valve. The liquid used in the experiments was distilled water with the addition of NaCl, to modify the electrical

conductivity, and of a surfactant to reduce water surface tension. Water electric conductivity was measured with an Elmertron conductivity meter (mod. CPC-401).

To characterize the properties of the charged droplets, the electrospray was operated in free air and the droplets drip into a Faraday cup. Images of the falling droplets were acquired by a high speed black and white CCD camera (Allied Vision Technologies mod. GC650), with an exposure time of 8 μs. To optimize the optical measure, a halogen lamp was placed in front of the camera, on the rear part of the falling droplets. Light intensity can be adjusted modifying the voltage supply with a DC transformer from 0 to 10V. The camera was connected to a PC for data logging. The stored videos were converted in frames and post-processed using Image Pro Plus® software to measure drops diameters and generate a droplet size distribution. At least 100 frames were analyzed for each test. A homemade Faraday Cup connected to an electrometer (Keithley, mod. 6514) was used to measure the spray current generated by the falling of the droplets. The experimental set up and a picture of the system are reported respectively in Figure III-4 and Figure III-5.

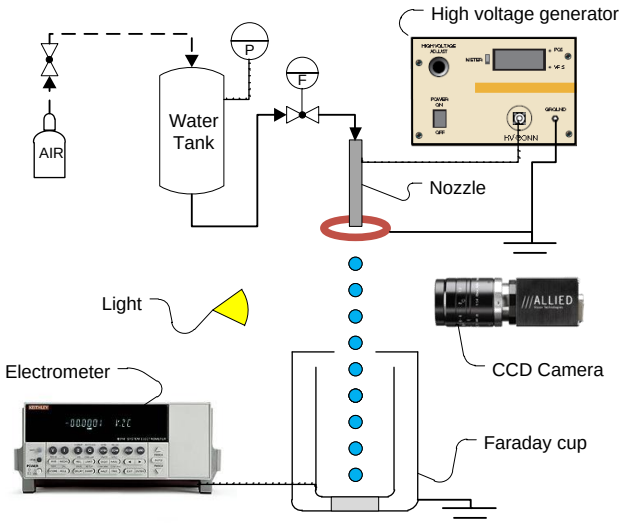

Figure III-4: Experimental apparatus for droplet characterization

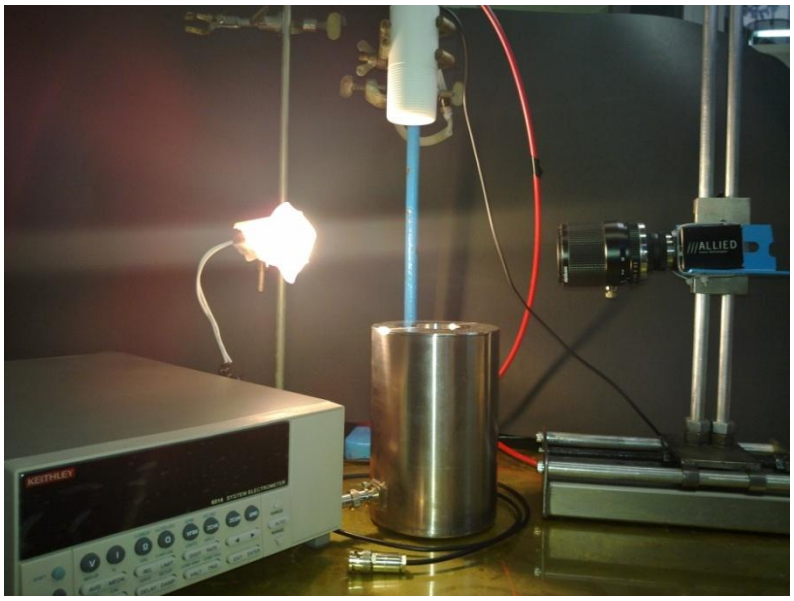

Figure III-5: Picture of the experimental apparatus for droplets characterization

III.1.1. Preliminary results on droplet charging

The experiments, as mentioned before, were carried out by operating the electrospray in dripping mode. In this regime, the emission of droplets may occur at regular time intervals, without the creation of satellites droplets, so that all the droplets have the same size and charge [68]. At a fixed flow rate, if the applied voltage is increased starting to zero, the droplet size decreases up to the formation of satellites droplets, as shown in Figure III-6.

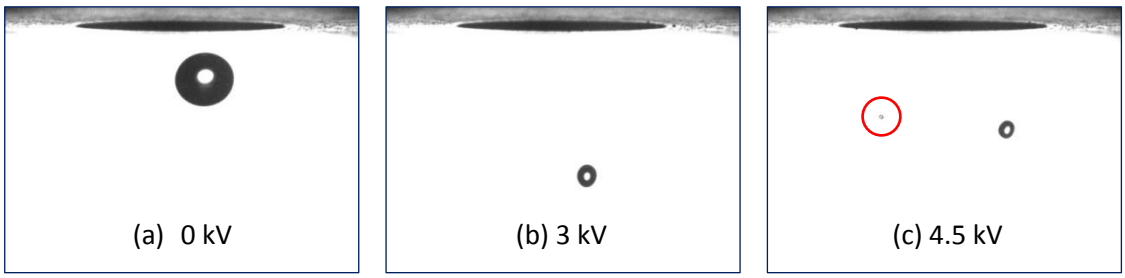

Figure III-6: Droplet reduction due to voltage increase up to the formation of satellite droplets (c). The upper part of each picture is the charged droplets generator box

The charge of these droplets can be very different compared with the main droplets [69]; that is an unwanted phenomena. Then, it was decided that the upper limit of the applied voltage adopted in the experiments corresponds to the voltage beyond which satellite droplets appear. A surfactant (TWEEN 80 at 0.32%w) was added to reduce surface tension and, therefore, the formation of satellites droplets.

Both the conical and the flat needles used operated in the so-called *outer wetting mode* [70]; therefore, the droplets grow on the needle tip adhering to the base area of the needle (see Figure III-7). In this case, droplet dimensions are related to needle outside diameter and on its surface tension.

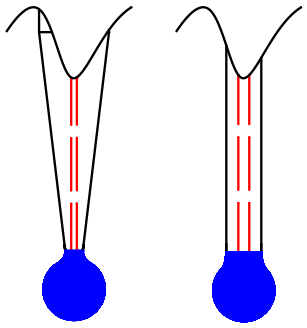

Figure III-7: Schematic representation of the wetting mode

The internal diameter of the needle is instead important for the transition from a discontinuous mode, the dripping, to the formation of a jet (not a spray). At a fixed internal diameter and no applied voltage, increasing the flow rate the falling frequency increase up to the formation of a jet. Clearly, the smaller the inner diameter of the capillary is, the lower will be the flow rate at which the jet appears. This flow rate represents the upper limit at 0kV.

Both water flow rate and applied voltage have than an upper limit linked to practical constraints. In addition, minimum constraints exist for the variables. The minimum value of applied voltage investigated is zero Volts; negative polarity was not investigated because the particles will be charged with this polarity. Nevertheless, literature investigations reveal that droplet size and charge should be substantially the

same (except for the polarity) for positive and negative applied voltage in dripping mode [68].

About the water flow rate, theoretically, a minimum value does not exist, but is evident that by decreasing the flow rate also the number of droplets produced tends to decrease, becoming incompatible with the study of particle abatement.

III.1.2. Experimental protocol for droplet characterization

This section indicates the procedures used to perform the tests for drops size and charge measurements. These procedures were based on several preliminary tests and were extensively proved to assure their consistency and robustness.
A list of operations executed during the tests is reported below:

Test preparation

1. The water tank is washed out with distilled water to remove any residual impurity from the system.
2. The tank is filled with water at the desired conductivity (previously prepared).
3. Air compressed is feed into the tank up to a desired pressure by the regulation valve.
4. Electric power supply is tuned to the desired voltage.
5. Water flow rate is adjusted by means of the rotameter (the needle starts to drip).
6. The camera and the halogen lamp are switched on.
7. The light is adjusted to improve the contrast on the droplet contours
8. The camera focus is regulated. To check the focus, a number of droplet sampling images are made.

Camera calibration

1. A calibrated scale is put below the needle; in this way the droplets fall on a portion of the calibrated scale wetting a portion of it.

2. A number of sampling image are made to verify that also the calibration scale is in focus.
3. An image of the calibrated scale is stored and it will be used in the post-processing as the reference for droplet measuring.

Test execution

During the dripping the following data are acquired:

- Video of the droplets, dripping from the nozzle, are recorded through the fast CCD camera and video for data post-processing are logged (sampling time of 150s).
- The current transferred by charged droplet falling in the faraday cup is measured with the electrometer for a sampling time of 20s.

Power supply is switched off to stop tests. If other tests must be performed, the procedure start to point 4, otherwise the water tank is emptied and washed with distilled water.

Post-processing of data

1. Video files captured are converted into frames;
2. Specific frames of droplets (>100 frames per sample) are manually selected; each frame selected contains a single droplet.
3. The reference image captured during the calibration is elaborated in the software Image Pro Plus® to provide a reference length in the software.
4. Droplets frame are inserted in the software and automatic processed by means of a homemade macro.
5. The results of the elaboration (Droplet mean size and standard deviation, droplet mean aspect ratio and standard deviation) are stored in a specific excel file.
6. The data acquired by the electrometer (current during the time) are elaborated.

III.2. Experimental rig for particle charge and size characterization

The particles used in the experiments were produced burning an incense stick placed in a closed glass modified washer box (Figure III-8). Air compressed, oilless and free of particles, was used as carrier gas. The air flow rate was measured and adjusts using a rotameter (Rota Yokogawa mod. RAGH01) operating between 0.5 and 5 m^3/h. Only a portion of the air was sent into the washer to avoid particle concentration above the upper detection limit of the particle size analyzer. Particle concentration was controlled by diluting the air at the exit of the washer and, in case, purging part of it.

Air and particles were sent to a wire and tube charging unit. This consists of an electrically grounded metal tube of 100 mm length and internal diameter of 29 mm with a coaxial wire of 500µm connected to high voltage power supply (Bertan mod. 230-20R). The particle flowing in the charging unit become charge due the presence of corona discharge established between the wire and the tube. The particle residence time in the corona discharge was modified by changing the air flow rate and the effective length of the wire shielding both the metal tube and the wire with some PTFE cylinder of different length and a PTFE tube (ID 1mm OD 2.5mm) respectively [71] (Figure III-9).

The current provided to the wire was measured by the high voltage power supply and was displayed on the instrument with a precision of 1µA. In addition, to evaluate possible current leakage, the current that flowed from the metal tube and the ground was also measured using a microammeter with a precision of 0.1 µA (Mitec mod. 6730).

The charging unit was coupled with a quiet tube (L=100 mm) that housed a hole to insert the sampling probe of the particle counter/size analyzer or a humidity probe. The humidity probe utilized was a HP475 C1R model connected to the instrument Delta OHM DO 2003 Datalogger. During normal operation, the quiet tube was connected with the WES reactor and the hole was plugged.

To characterize particle size distribution and charge levels, the charging unit and the quiet tube were connected with a Dynamic Faraday Tube (henceforth called DFT). The DFT used in this work consists of two metal cylinders (made in AISI 316), electrically isolated by two Plexiglas cylinders. The external tube acts as a shield from electric noise while the internal tube was filled with fine mesh wire. The DFT was connected to the electrometer to measure the current from the charged particles.

The layout of the charging unit, quiet tube and DFT is reported in Figure III-10. A picture of the assembly is reported in Figure III-11.

Number and size distributions of the particles were measured with the Laser Aerosol Spectrometer TSI LAS-3340 that is able to measure particle size between 90 and 7500 nm, with maximum particles flow rate of 3000 particles/s. To this aim, air and particles were aspirated through an isokinetic sampling tube (the sampling flow rate was in the range of 30 and 55cm^3/min in function of the air flow rate utilized in the test), inserted in the quiet tube, and sent to the particle size analyzer.

Figure III-8: Incense stick box

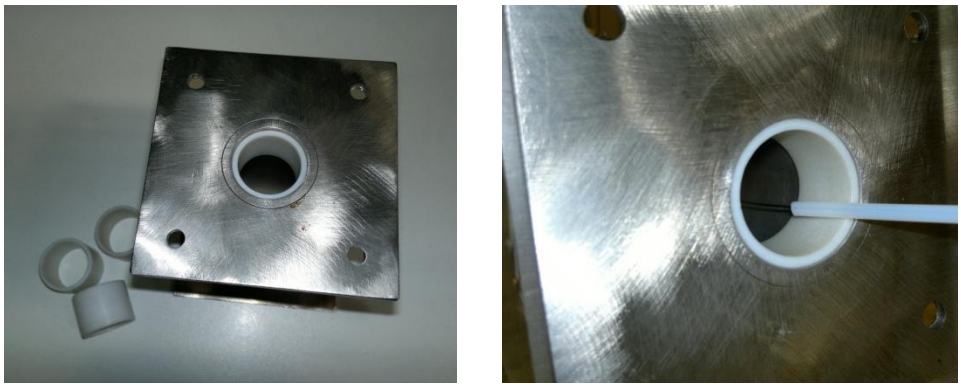

Figure III-9: Grounded tube and high voltage wire partially shielded by PTFE cylinders and PTFE tube respectively

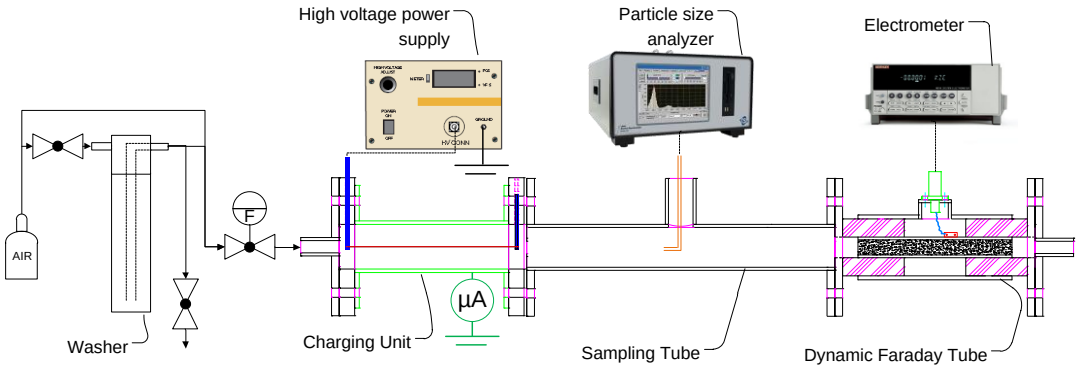

Figure III-10: Experimental apparatus for particles charge and size distribution measurements

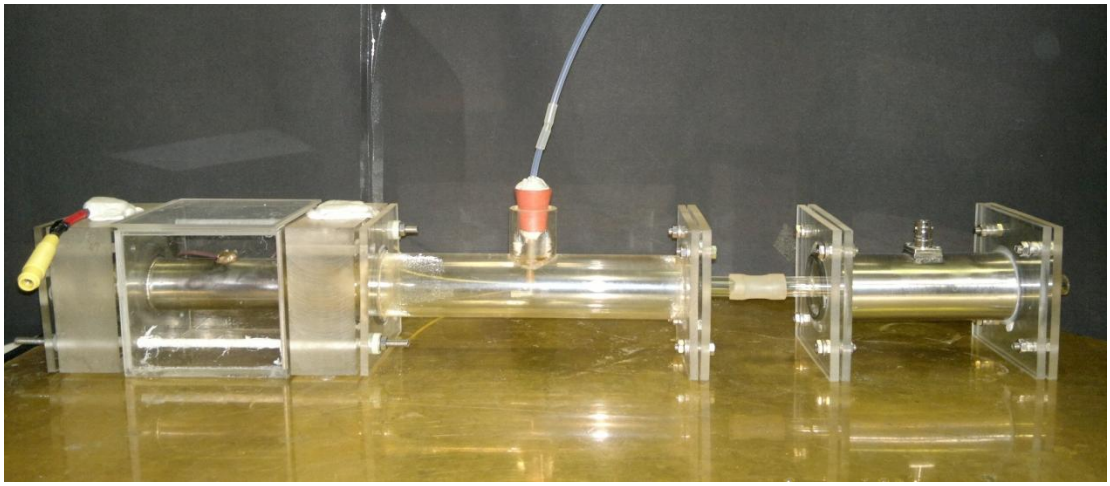

Figure III-11: Picture of the experimental apparatus for particles characterization

III.2.1. Preliminary tests on particle charging

Preliminary tests were carried out in order to optimize the experimental procedure and verify the limits of the system in terms of applied voltage. The tests were carried out at negative polarity applied to the charging unit to reduce back corona problems at high potentials. The minimum voltage for the charging unit corresponded at the voltage when corona discharge starts. This value can be calculate with the empirical formulas (II-16) and (II-18), corresponding in -9.18kV for the geometry utilized. This value was experimentally verified measuring the current transferred from the wire to the cylinder with the electrometer, increasing the voltage applied to the discharge electrode (the wire). This operation is displayed in Figure III-12.

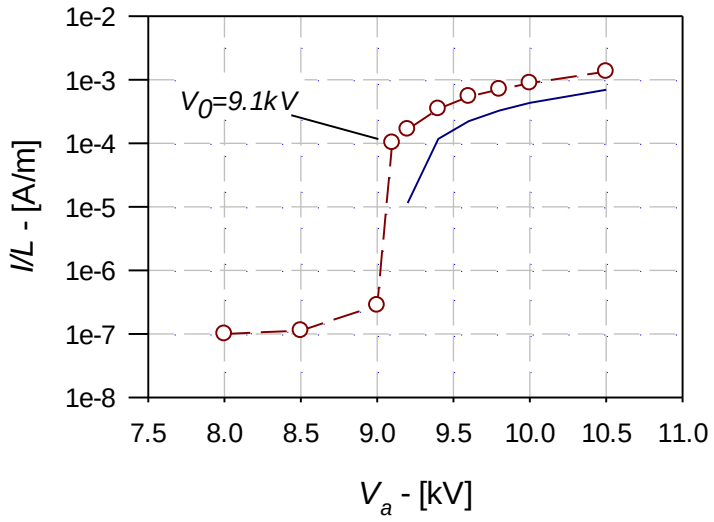

Figure III-12: Experimental discharge current (dash line) and theoretical prediction (solid line)

The dash line in Figure III-12 represents the experimental values of the normalized current provided and by the high voltage generator and measured by the electrometer. The experimental curve shows a sudden increase at 9.1kV that represent the starting point of the corona effect. This value is in perfect agreement with the theoretical value of 9.18kV for incipient corona discharge. In the Figure III-12 the theoretical prediction of the normalized current obtained from the equations (II-16) and (II-18) is also reported. The trends of the two curves are very similar, but the model gives an

underestimation of about 45%. Despite for the differences, it must be noticed that the current measured and provided to the high voltage generator can slightly change if the grounded surface of the charging unit shows particle deposits; this imposed frequently maintenance and cleaning of the unit. The upper limit for the voltage corresponds to the occurrence of the back corona; during preliminary checks, the maximum voltage tested was 13kV and at this voltage back corona, with the formation of shocks, were not present. Higher voltages were not investigated to avoid risks of electric shocks.

Other investigations were executed to verify the performance of the Dynamic Faraday Tube. Differently from the Faraday cup utilized for the droplet, the DFT have an inlet and an outlet for the air stream that makes quite difficult the shielding of the inner tube, which can actually read only the charge carried by the particles, from external noise. Another source of noise was related to free ions carried by the air and produced to the corona discharge. In order to have a good sensibility of the measure, the current related from the two noises must be lower than the current related to the charged particles. In Figure III-13 the effects of the two noises on the current measure are reported.

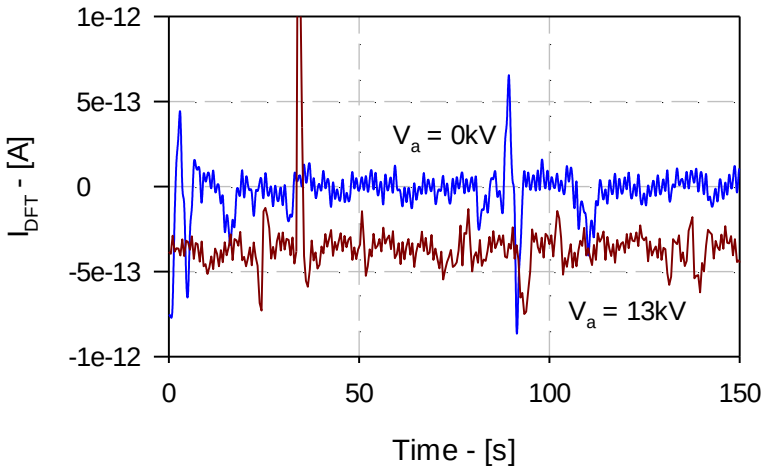

Figure III-13: Current measured at the DFT (without particles) at air flow rate of 2.7m^3/h at 0kV (blue line) and -13kV (red line)

The measure in Figure III-13 were carried out connecting in series the charging unit, the quiet tube and the Dynamic Faraday Tube and working at 2.7m^3/h. The blue curve represents the current measured at the DFT (I_{DFT}) in a sampling time of 150s and with no voltage applied. The signal shows random oscillation around 0A and a mean amplitude peak-to-peak of $2.3 \cdot 10^{-13}$A. When a negative polarity is applied to the wire (red line), the curve shifts in the negative region of a mean value of $-4.4 \cdot 10^{-13}$A, keeping a mean oscillation peak-peak of the same order of magnitude ($5.6 \cdot 10^{-13}$A). This measure reveals the presence of ions produced by the corona in the air. The two tests were carried out under the worst conditions of voltage applied and air flow rate in terms of noises; however the current recorded related to the two tests are negligible in comparison with the current transferred by the charged particles.

To justify this observation, the current due to particles charged at four voltage applied at the discharge electrode are reported in Figure III-14.

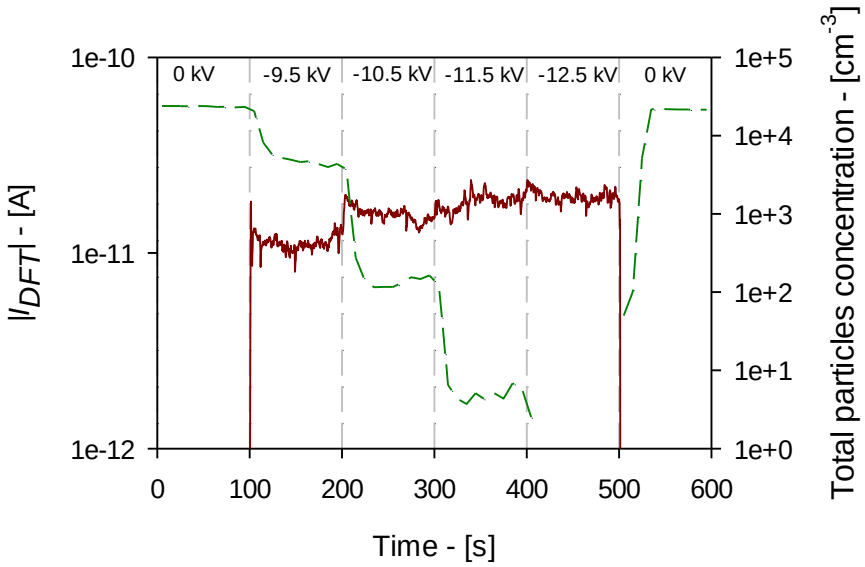

Figure III-14: Absolute values of the I_{DFT} due to charged particles (solid line) and total particle concentration (dash line) sampled during the time at 0, 9.5, 10.5, 11.5 and 12.5 kV. The mean velocity in the DFT is 8m/s.

The test reported in Figure III-14 was executed using the standard configuration of the experimental apparatus shown in Figure III-10. The air flow rate was set at 2.7m^3/h corresponding to a mean velocity of 8m/s.

The particle size distribution and the current at the DFT were recorded during the test. The voltage was increased of 1kV starting to 9.5 kV up to 12.5kV every 100s; other two steps at 0kV were executed as initial and final steps, resulting in a total of six stages. The solid curve in Figure III-14 represents the current measured at the DFT. The values of this current in the first and the last step, when no voltage is apply to the wire, have the same order of magnitude reported in Figure III-13 for the blue line ($\approx 10^{-13}$A), but are not visible for the log scale. When the voltage is applied, the current increases of more than two order of magnitude, reaching values of $\approx 10^{-11}$A; the further increase of apply voltage determines the increase of the current measured at the DFT due to higher particles charge levels up to reach stationary conditions. Therefore, the current measured in presence of corona discharge results always at least two orders of magnitude higher than the baseline, demonstrating that the background noise is negligible. The voltage increase, however, also affects measured particle concentration (dash line in Figure III-13): starting from 0kV the total particle concentration is about $2.3 \cdot 10^4$ particles/cm^3 and it decreases coherently with the increase of applied voltage, until it reaches zero for -12.5kV. Then the concentration returns to the initial value in the last step, when the high voltage is switched off.

The particle concentration decrease can be related to the abatement in the charging unit that, simply, works an electrostatic precipitator; but the result obtained at -12.5kV seem to be in contrast with the previous results: if the particles were not present, the DFT should read a current comparable to the background noise. Nevertheless, the current measured was similar to that observed in the presence of charged particles. This evidence reveals the presence of charged particles in the DFT that, therefore, do not reach the laser sensor of the particle size analyzer probably due to adhesion with the sampling tube.

This experimental problem reveals a limit of the experimental apparatus: if the particles are charged, the real particle concentration that flows in the DFT cannot be measured due to particle adhesion with the tube materials. In order to bypass the problem, a specific procedure was developed, providing a first step of measure of the

particle distribution without applied voltage, and a subsequent step with an applied voltage, in the range of 9.2-12.5kV, to charge the particles and the current transferred in the DFT. This procedure requires a sufficient stable particle concentration during the test; therefore, the measure of particles distribution in absence of voltage was executed before and after that the voltage was applied.

However, the particle concentration measured in absence of corona discharge is still not the real concentration that flows in the DFT when the voltage is applied, because the particle fraction lost in the charging unit, which works like an electrostatic precipitator, must be considered. Of course the length of the charging unit and the voltage applied were not enough to reach high particle abatement (never more than 20% under the worst conditions), but the particle fraction lost must be considered. Therefore the particle concentration measured in absence of electric field could be corrected in the post processing phase under the hypothesis of the classic Deutsch-Anderson equation reported in the paragraph II.2.1.2.3.

III.2.2. Experimental protocol for charged particles characterization

This section describes the procedures used to perform tests on the charged particles in order to evaluate on aerosol charge to mass ratio and a particle size distribution. A list of operations executed during the test is reported below:

Test preparation

1. Air flow rate is adjusted with the rotameter.
2. Flow rate sampled by the Laser Aerosol Spectrometer is adjusted in order to have an isokinetic sampling.
3. The incense stick is lit and pun in the washer.
4. Humidity and temperature of the carried gas are measured in the quiet tube.
5. High voltage is set at the desired value but not switched on.

6. Particle concentration is adjusted op to reach the maximum concentration readable to the instrument (3000 particles/s) that is a function of the flow rate imposed.

Test execution

7. The Laser Aerosol Spectrometer and the electrometer are started to record and store the data.
8. After 100s of sampling the high voltage generator is switched on at fixed voltage in the range 9.1-12.5kV.
9. During this step the current provided to the generator, and measured by the microammeter, are recorded.
10. After other 100s of sampling, the high voltage generator was switched off.
11. Finally other 100s of sampling at 0kV conclude the test.

Post-processing of data

12. The data acquired are elaborated in order to evaluate the aerosol charge to mass ratio

III.3. Experimental rig for particle abatement by wet electrostatic scrubbing

The experimental rig used in this part is described in Figure III-15. A picture of the experimental system is instead reported in Figure III-16. The core of the system is the WES reactor that consists in a Plexiglas® vertical tube with height of 200 mm and diameter of 100 mm. The chamber is designed to be firstly filled with a particle-laden gas and then closed, so that it operates in batch mode, similarly to the large scale experimental system developed by Balachandran, Jaworek and co-workers [60, 61]. The height and diameter of the chamber are selected to facilitate operation and maintenance procedures and allow easy introduction of probes.

The WES chamber is closed at the bottom and has a removable lid on the top that contains the nozzle box. This lid also houses two holes to insert a hygrometric probe and a hot wire anemometer. In the bottom of the reactor a hole is also present to drain water. The lateral surface of the cylinder presents a hole (D =3 mm), to insert the sampling probe for particle analysis. The sampling air aspirated by the particle size analysis after the analysis is recirculated at the exit of the instrument to the reactor through a further hole on the lid in order to mix the air in the closed system and homogenize particle concentration. This recirculation also avoids decrease of vessel pressure due to the air aspirated to the particle analyzer, which may also cause the entry of environmental air. The lateral surface of the reactor presents two 10 mm holes for gas inlet and outlet; and it is covered with a grounded wire mesh to shield the vessel from external noise.

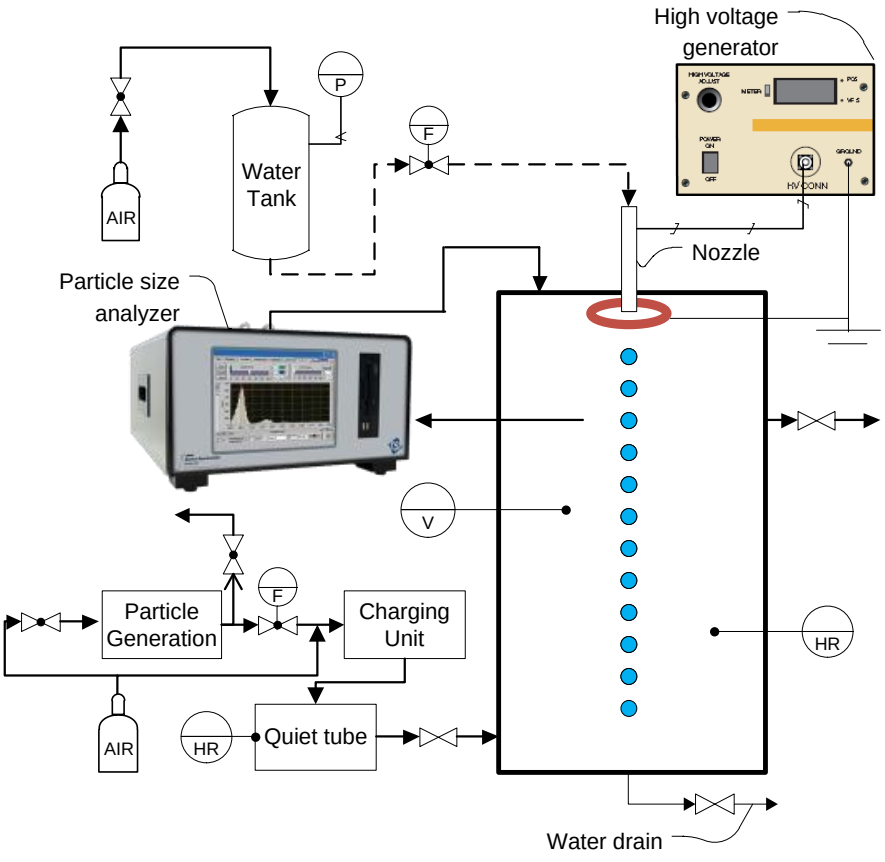

Figure III-15: WES reactor layout

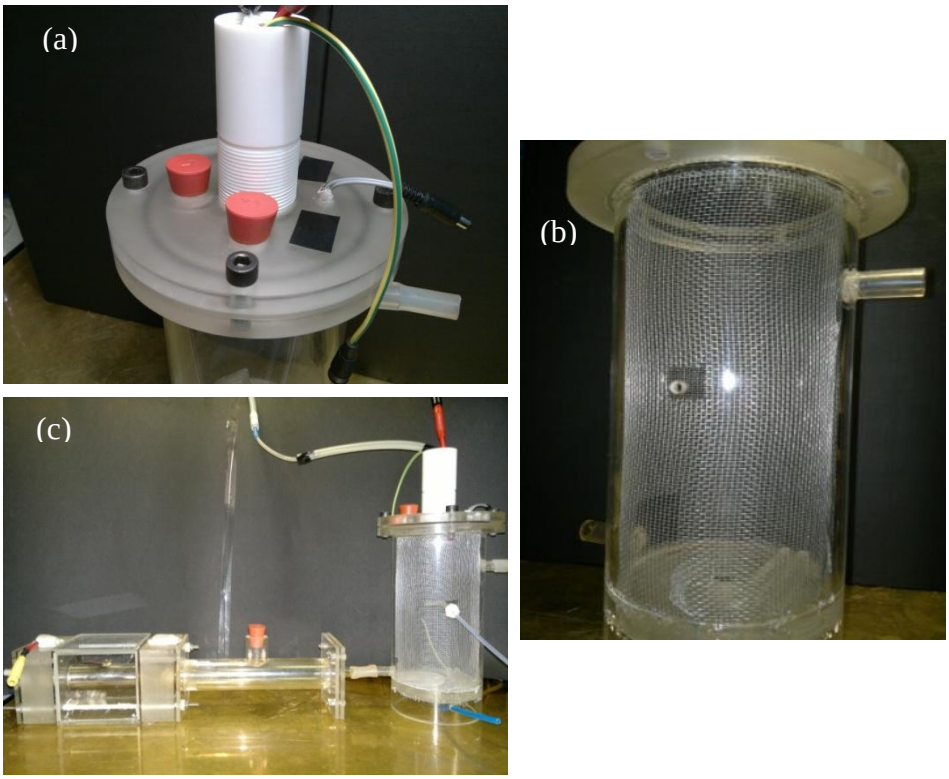

Figure III-16: Details of WES reactor (a-b) and complete system(c)

III.3.1. Preliminary experimental results on particle abatement

In this section, preliminary results on particle abatement in the batch reactor, used to in order to optimize the experimental procedure and verify the limits of the system, are reported.

In Figure III-17 the typical charged particle abatement due to charged droplets is reported; the concentration during the time in absence of droplets is reported too.

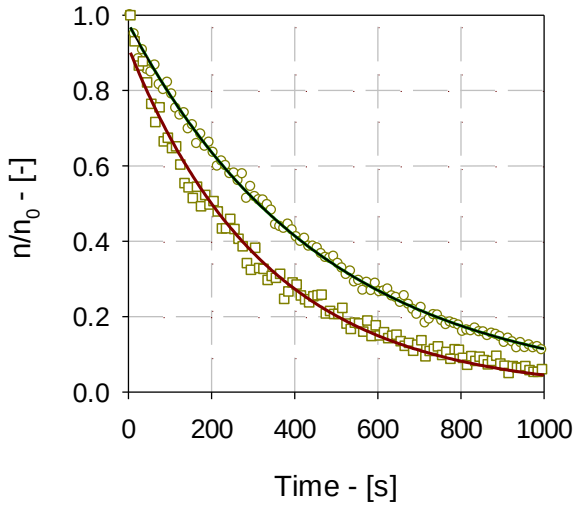

Figure III-17: Charged particle concentration (d_p=200nm) during the time in presence of charged droplets (q=100pC D=1.7mm, square symbols) and without droplets (circle symbols)

The square symbols in Figure III-17 represent the normalized particle concentration during the scrubbing time, while the circle symbols are instead referred to the concentration in the reactor without droplets. From an analysis of the results, four aspects should be highlighted:

- The characteristic times required to achieve appreciable particle abatement are of the order of hundreds of seconds; therefore these time are incompatible with a continuous system; this justify the adoption of a batch reactor.
- Both experimental trends in Figure show an exponential decay trend. The same behavior is verified for all investigated particle size; moreover, working at different experimental conditions like different droplet size or droplet charge, the two curves can move down or move up to overlap, but they always have an exponential decay trend.
- Also in absence of water droplets, particle abatement in the reactor is relevant. This can be linked to a natural particle adhesion on the reactor walls, an effect that is enhanced to the charge on the particles. In addition, the electric field near the electrospray, kept at a polarity opposite of that of particles (which

have a negative charge), can contribute to the particles abatement. The particle abatement due to these contributions (henceforth called *baseline* contribution) is unwanted, but is impossible to eliminate.

- When the droplets are present, the particle concentration decrease more quickly due to the sum of the further contribution of the droplet. Henceforth, the particle abatement related to all the effects will be referred as a *total* contribution. In order to evaluate the particle removal only due to the droplets, (*droplets* contribution) the contribute of all the other effects, not related to the droplets (i.e. the *baseline* contribution), must be take into account.

The particle abatement due only to the droplet can be calculated subtracting the baseline contribution to the total one. Formally this operation could not be executed directly on the data reported in Figure III-17 because they are obtained in two different experiments at initial concentration that, despite similar, are different.

To overcome this difficulty it is necessary to analyze the data from a kinetic point of view. Since the data in Figure III-17 are well described by an exponential decay trend (and this if true for all particle size experimental measured), reporting the data in logarithmic coordinate they are well fitted by a straight line as shown in following Figure.

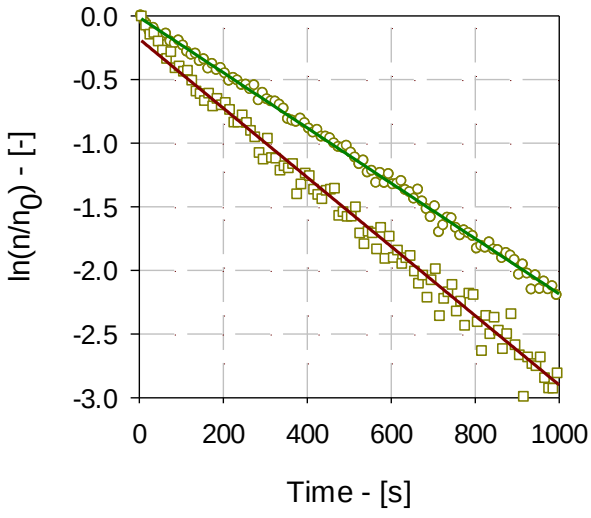

Figure III-18: Data of Figure III-17 reported in logarithmic coordinate

The elaboration of the experimental data in logarithmic coordinate represents the characteristic solution of a first order kinetic in particle concentration. Therefore, the differential equation and its solution can be written as:

$$\frac{dn}{n} = -\Lambda t \quad and \quad n|_{t=0} = n_0 \tag{III-1}$$

$$ln\left(\frac{n}{n_0}\right) = -\Lambda\, t \tag{III-2}$$

The constant Λ in the equations represent the slope of the two straight lines and it does not depend on particle concentration. Is therefore possible to conclude that, in order to evaluate only the droplet contribute on particle abatement, the difference from the two slopes in Figure III-18 can be used, then results:

$$ln\left(\frac{n}{n_0}\right) = -\Lambda_d\, t = -(\Lambda_t - \Lambda_b)t \tag{III-3}$$

$$\eta_d = 1 - \exp(-\Lambda_d\, t) = 1 - \exp[-(\Lambda_t - \Lambda_b)t] \tag{III-4}$$

Where η_d represent the particle abatement efficiency due only to the droplet in the reactor, Λ_t and Λ_b are respectively the slopes of the straight lines obtained due to the total contributions and baseline contribution, while Λ_d is the difference between the two slopes and is representative of the particle abatement contribution only due to the droplets.

Therefore the evaluation of Λ_d needs the execution of two tests. Must be add that in the two tests, the inlet particles coming from the charging unit could have a different charge distribution (as will be discussed in paragraph IV.3.2) and therefore the difference Λ_t - Λ_b can be effect by big errors. To overcome this problem, the two tests can be concentrated in a unique experiment split in two parts. In a first step, the particle concentration can be measured in presence of droplets. In a subsequent step, the baseline contribution can be monitored in absence on droplets, by simply switching off the water flow rate at the charged droplets generator but leaving the high

voltage at the needle to consider the baseline effect due to the electric field at the tip. An example of the particle abatement obtained with this methodology is reported in Figure III-19.

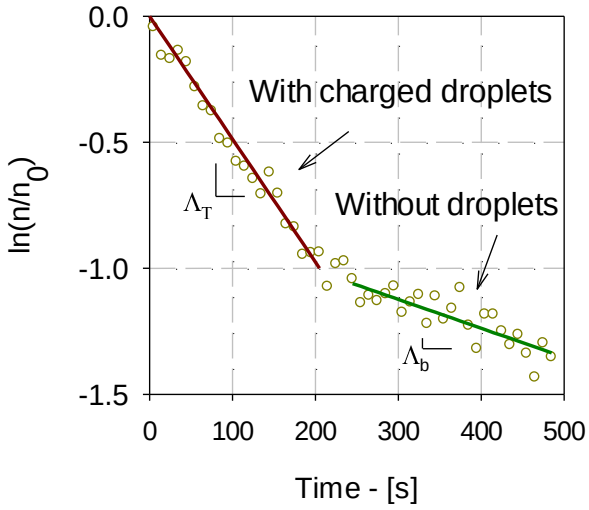

Figure III-19: Particle abatement (d_p=300nm) during the time in presence of charged droplets (q=70pC, D=1.2mm, red line) and without droplets (green line)

As for the previously case, the Figure III-19 show that the presence of falling droplets produce higher particle abatement velocity than those in absence of droplets.

From an analysis of the preliminary results reported, three aspects it is worth to highlight:

- Experiments demonstrate that the particle abatement due to the droplets follows a classic first order kinetic described by an exponential decay trend. This result is consistent with the theoretical prediction as reported in the paragraph II.2.1.3, therefore, for comparison, Λ_d represent the particle scavenging coefficient.
- The experimental apparatus do not allow the control of initial particle concentration; therefore, all the tests are carried out at initial concentration that could be different from test to test. Nevertheless experimental data reveal that, in the investigated range, the particle abatement velocity follow a first order

kinetic, allowing to assume its independence of this rate to the initial concentration.

- The particle abatement efficiency in the reactor is a function of the scrubbing time; therefore, due to different particle abatement velocities and different scrubbing time, the best way to present the data is by considering the scavenging coefficient that are independent upon the test duration. Therefore, the results of the particle abatement experimentation will be presented and discussed in terms of droplet scavenging coefficients.

III.3.2. Experimental protocol for particle abatement

This section indicates the procedure used to perform tests on particle abatement in order to evaluate the droplets scavenging coefficients for each particle size analyzed. A list of operations executed during the test is reported below:

Test preparation

1. The water tank is washed out with distilled water to remove any residual impurity from the system.
2. The tank is filled with water at the desired conductivity (previously prepared).
3. Air compressed is feed into the tank up to a desired pressure by the regulation valve.
4. Electric power supply to the charged droplets generator is tuned to the desired voltage and switched on.
5. Water flow rate is adjusted by means of the rotameter (the needle starts to produce charged droplets).
6. Air flow rate for the charging unit is adjusted through the rotameter.
7. Flow rate extracted to Laser Aerosol Spectrometer is adjusted at 90cm^3/min; this flow rate provide a good particle mixing in the reactor due to the air recirculation.
8. The incense stick is lit and pun in the incense stick box.

9. Humidity and temperature of the carried gas are measured in the quiet tube.
10. High voltage at the particle charging unit, assembled in order to have a wire length of 38mm, is adjusted at the desiderate voltage.
11. Particle concentration is adjusted op to reach the maximum concentration readable to the instrument.

Test execution

12. When the concentration reach the desiderate value the inlet and outlet of the reactor was plugged.
13. The Laser Aerosol Spectrometer starts to record and store the data.
14. The particle size distribution is displayed on the monitor of the LAS, when the concentration of the particle reaches about the half, the water to the charged droplets generator is switched off.
15. In this step the particle abatement due to baseline effects is monitored; the test is stopped when the particles distribution reach values near the zero.

Post-processing of data

16. The data acquired by the Laser Particle analyzer are sent to the PC and elaborated in order to evaluate the total and baseline scavenging rate. These results allow to calculate the droplet scavenging coefficient.

CHAPTER IV - Experimental results and discussion

IV.1. Introduction

In the following, the main results obtained during the experiments are reported. The results are organized in three sections: the first two are related to the experimental results on the characterization of the charged droplets and particles, while the third section the results of the experiments on wet electrostatic scrubbing are reported. The experimental results will be also used to allow the proper utilization of the theoretical models reported in the paragraph II.2.1, aimed to the comprehension of the physics that govern the wet electrostatic scrubbing process.

IV.2. Experimental results on droplet characterization

IV.2.1. Scope of experimental section

The objective of this experimental part is to identify sets of operational conditions that, applied to the charged droplets generator, allow to generate a stable and reproducible train of droplets. In fact, by varying some parameters (dimensions of the needles, needle typology, water electrical conductivities, surface tension, high voltage applied to the charged droplets generator, water flow rate) droplets dimension, charge and falling frequency could change [72] providing different operating conditions that can be adopted to study particle abatement in different experimental settings.

IV.2.2. Experimental results on droplet charging

On the basis of the experimental procedure illustrated in the paragraph III.1.2, the effects of liquid flow rate, applied voltage, and liquid electric conductivity on droplet size and charge were systematically investigated for both conical and flat the needles. Tests have been carried out with water at different electric conductivities, at different flow rates and by varying voltage level.

Water electrical conductivity was modified by adding NaCl salt to distilled water in order to mimic the electrical conductivity of a tap water and that of half of seawater.

During the tests the current acquired by the electrometer were elaborated in order to evaluate the charge to mass ratio of the droplets. An example of the current acquired during the dripping is reported in Figure IV-1.

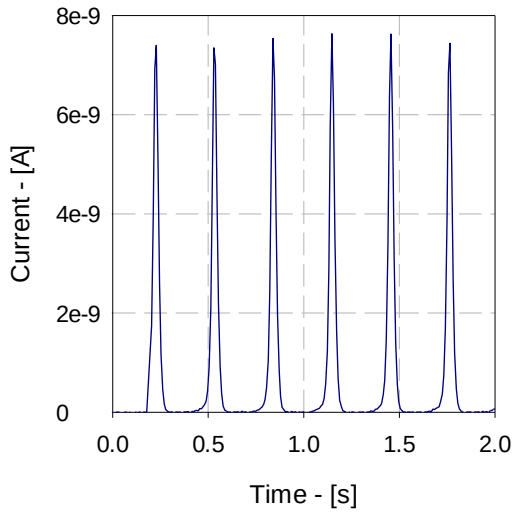

Figure IV-1: Example of current acquired during the dripping

In the Figure IV-1 each peak represents the falling of a droplet and the area below the peak is the correspondent charge. In order to improve the quality of this measure, the electrometer was set on the maximum reading rate of 5000 Hz. The Droplet Charge to Mass Ratio (D-*CMR*) was calculated according to the equation (IV-1).

$$D - CMR = \frac{q_{exp}}{m} = \frac{\int_0^{t_s} A(t)dt}{\rho_w Q_w t_s} = \frac{\sum_{i=0}^{n} A_i \Delta t_i}{\rho_w Q_w t_s} \qquad \text{(IV-1)}$$

Where t_s is the sampling time fixed for all the tests in 20s.

The charge to mass ratio is a variable widely used to quantify the amount of charge transferred and is a property of the spray; due to different size and dynamic of formation, the actual *D-CMR* of each droplet in a spray with a wide size distribution

can be quite different from that of the average spray. However, in the dripping mode regime, where the droplet have roughly the same size, the *D-CMR* evaluated with the equation (IV-1) also correspond to the actual charge to mass ratio of the single droplet.

In Figure IV-2 droplet diameter and charge to mass ratio are reported for the conical needle at two water electric conductivity and three water flow rates. The results show a droplet size reduction with water flow rate and applied voltage. On the contrary droplet charge to mass ratio increases by increasing water flow rate and applied voltage. These results are consistent with the classical theory of electrospraying: due to the rise of spray current achieved by increasing voltage, the droplet diameter is expected to decrease with the voltage [68]. Experimental results show that the water electric conductivity seems to have a negligible effect on the droplet diameter, probably due to a limited effect of salt concentration on the liquid surface tension in the investigated conditions. Similarly there is a limited variation of droplet charge with water conductivity.

Figure IV-2 show also a contraction of the analyzed voltage range, which skips from 0-3kV at 0.50 ml/min to 0-1.8 kV for 1.50 ml/min. This is the due to the needs of avoiding the formation of satellites droplets as mentioned in the previous CHAPTER III - .

In Figure IV-3 the results on droplet size and *D-CMR* for the flat needle are reported. The patterns of droplet size and charge are similar to those observed in Figure IV-2. This needle, however, presents a lower tendency to form satellites droplets, so that the voltage investigated can be increased up to 4.2kV for the flow rate of 1.4mL/min. In addition, the transition from dripping mode to the jet mode was shifted up due to a higher needle internal diameter, allowing working at a flow rate up to 2.00mL/min.

By comparing the results of Figure IV-2 and Figure IV-3, it is evident that the flat needle is able to produce smaller droplets at higher charge to mass ratio, thanks to its intrinsic stability to work at higher voltage and flow rate.

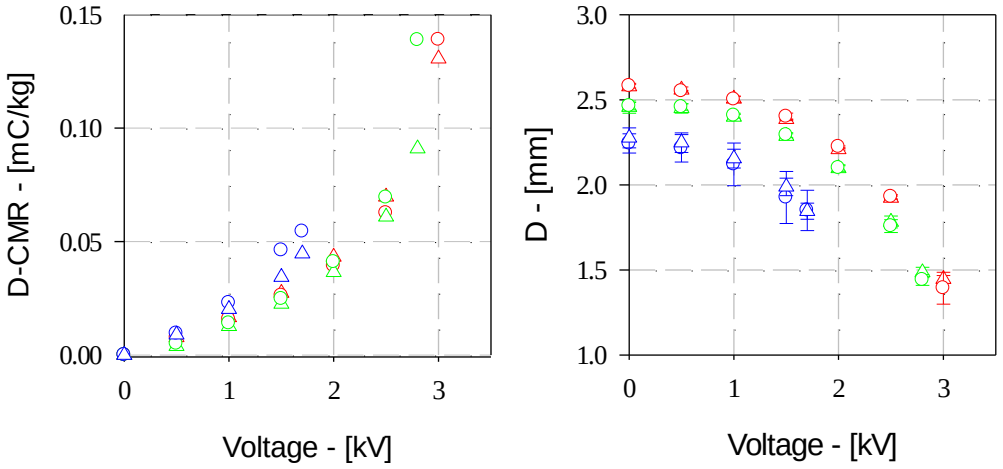

Figure IV-2: Droplets diameter and charge to mass ratio for the conical needle at water flow rates of 0.50, 1.00 and 1.50mL/min (respectively red, green and blue symbols) at water electrical conductivities of 1.0 mS/cm (circles) and 20.0 mS/cm (triangles)

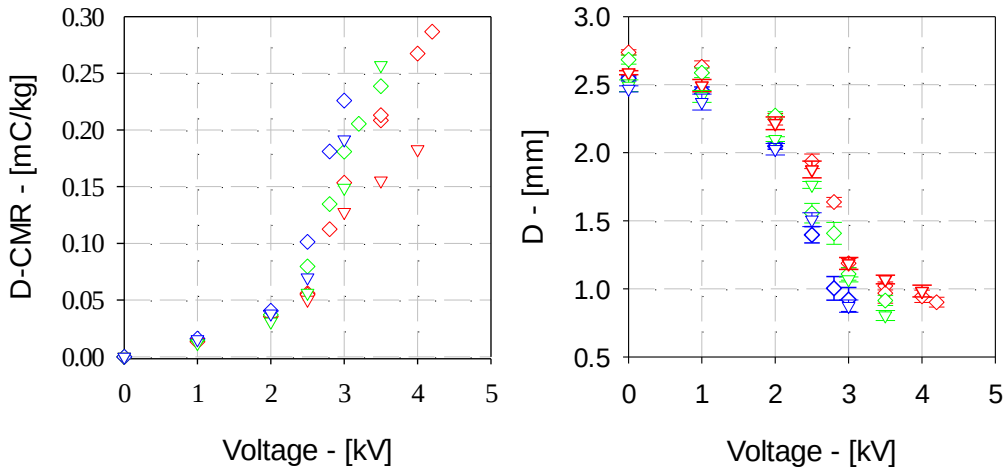

Figure IV-3: Droplets diameter and charge to mass ratio for the flat needle at water flow rates of 1.40, 1.85 and 2.00mL/min (respectively red, green and blue symbols) at water electrical conductivities of 1.0 mS/cm (diamonds) and 20.0mS/cm (triangles)

Starting from the results of droplet charge to mass ratio and droplet diameter, the droplet charge q can be evaluated by the equation (IV-2).

$$q = CMR\ \frac{\pi D^3}{6} \tag{IV-2}$$

In order to evaluate droplet charge, experimental values were fitted by appropriate equations that correlate *D-CMR* and droplet diameter to the voltage applied V_E. In particular, the best fitting for the evaluation of the droplet *D-CMR* was found as the sum of two exponential equations with four parameters as reported below:

$$D - CMR = a \exp(b\, V_E) + c \exp(d\, V_E) \tag{IV-3}$$

Where V_E must be expressed in kV and *D-CMR* results in mC/kg. The fitting equation and the parameters have no physical meaning and are only adopted for their descriptive ability. The coefficients of the regression for the two needles are reported in Table IV-1 and Table IV-2.

Q_w [mL/min]	σ [mS/cm]	a	b	c	d	R^2
0.50	1.0	4.55E-03	1.12	0	1	0.995
0.50	20.0	4.32E-03	0	1.93E-03	1.41	0.989
1.00	1.0	9.65E-04	1.16	2.55E-03	1.16	0.994
1.00	20.0	9.14E-04	0	1.99E-03	1.49	0.977
1.50	1.0	5.09E-03	1.42	0	1	0.978
1.50	20.0	4.47E-03	1.36	0	1	0.979

Table IV-1: Regression coefficients for D-CMR in mC/kg for the conical needle

Q_w [mL/min]	σ [mS/cm]	a	b	c	d	R^2
1.40	1.0	7.49E-03	7.72E-1	0	1	0.947
1.85	1.0	3.52E-03	1.01	3.95E-3	1	0.966
2.00	1.0	2.00E-03	1.58	0	1	0.993
1.40	20.0	5.92E-3	7.27E-1	4.94E-3	7.27E-1	0.932
1.85	20.0	2.41E-3	1.34	0	1	0.991
2.00	20.0	4.12E-3	1.12	0	1	0.999

Table IV-2: Regression coefficients for D-CMR in mC/kg for flat needle

The best fitting for the estimation of the droplet diameter was instead found in the equation (IV-4).

$$D = a + \mathrm{b}\, V_E{}^{c} \qquad \text{(IV-4)}$$

Where V_E must be expressed in kV and D results in mm. The coefficients of the regression are reported in Table IV-3 and Table IV-4.

Q_w [mL/min]	σ [mS/cm]	a	b	c	R^2
0.50	1.0	2.56	-5.04E-2	2.81	0.997
0.50	20.0	2.55	-3.79E-2	3.11	0.989
1.00	1.0	2.45	-4.65E-2	2.94	0.993
1.00	20.0	2.46	-4.37E-2	3.05	0.995
1.50	1.0	2.24	-1.30E-1	2.12	0.960
1.50	20.0	2.27	-1.04E-1	2.60	0.897

Table IV-3: Regression coefficients for droplet diameter in mm for the conical needle

Q_w [mL/min]	σ [mS/cm]	a	b	c	R^2
1.40	1.0	2.83	-2.96E-1	1.38	0.940
1.85	1.0	2.87	-1.92E-1	1.86	0.962
2.00	1.0	2.57	-1.06E-1	2.55	0.986
1.40	20.0	2.66	-0.20	1.59	0.938
1.85	20.0	2.52	-9.70E-2	2.33	0.978
2.00	20.0	2.46	-5.72E-2	3.03	0.998

Table IV-4: Regression coefficients for droplet diameter in mm for the flat needle

The results of the elaboration are reported in Figure IV-4 and Figure IV-5 expressed as droplet charge and droplet charge on the maximum theoretical charge dictated by the Rayleigh limit (equation (II-1)).

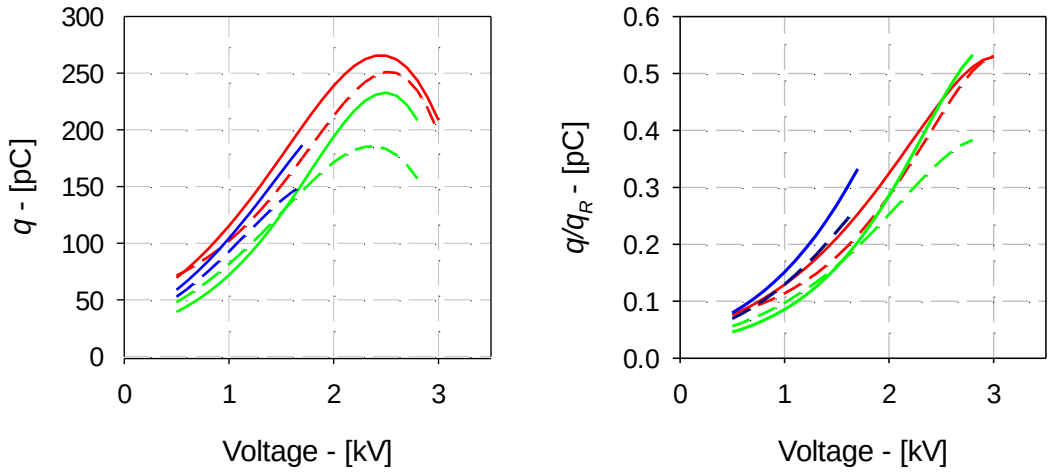

Figure IV-4:Droplet charge and droplet charge on Rayleigh limit for the conical tip needle at water flow rates of 0.50, 1.00 and 1.50mL/min (respectively red, green and blue lines) at water electrical conductivities of 1.0 mS/cm (solid line) and 20.0 mS/cm (dash line)

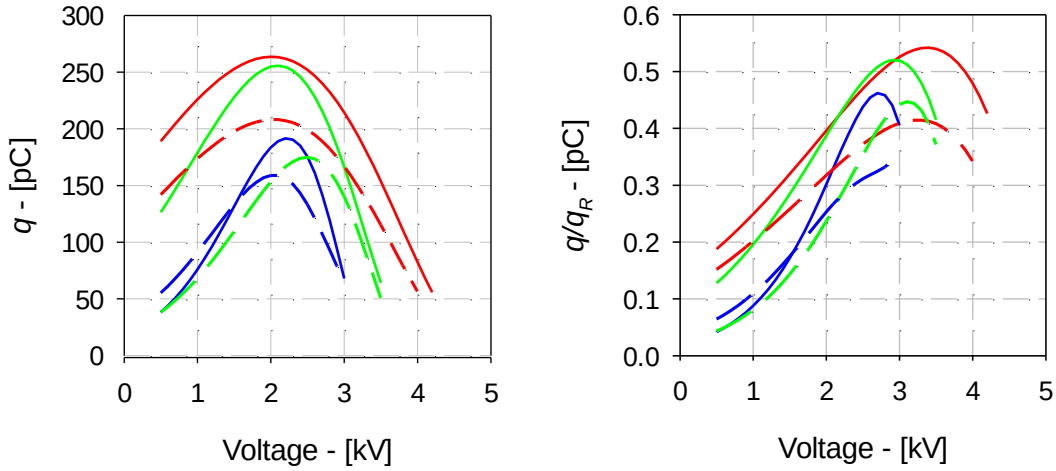

Figure IV-5: Droplet charge and droplet charge on Rayleigh limit for the flat tip needle at water flow rates of 1.40, 1.85 and 2.00mL/min (respectively red, green and blue lines) at water electrical conductivities of 1.0 mS/cm (solid line) and 20.0 mS/cm (dash line)

The droplet charge in Figure IV-4 and Figure IV-5 shows a non-monotonic trend, with a maximum of droplet charge at about 2.5 kV for the conical needle and 2kV for the flat one. The effect of the water flow rate is similar to the previous cases: lower values

of Q_w correspond to higher values of droplet charge. The droplet charges compared with the Rayleigh limits reveal that the dripping mode is able to produce very charged droplet up to the half of the maximum levels.

Since the results obtained depend on the needle dimensions, the operating variables and the fluid utilized, a reliable comparison of the results obtained in dripping mode with the results in literature is meaningless. Nevertheless, the results obtained by Jaworek and Krupa [22] on the dripping mode showed a similar qualitative trend of the droplet charge ant its diameter, and the order of magnitude of the two variables are the same.

IV.3. Experimental results on particle characterization

IV.3.1. Scope of experimental section

The objective of this experimental section is to characterize the amount of charge carried by the particles that flow through a corona discharge. As for the droplet charge, also the particle charge represent a fundamental parameter that must be evaluated or estimated in order to model the interactions between charged droplets and particles in the wet electrostatic scrubber. Differently from the case of the droplets produced in dripping mode, the particles generated by combustion have a wide size distribution. In this case, the evaluation of the aerosol charge to mass ratio does not give specific information on the particles charges. In fact, the charge acquired by a particle in a corona discharge depends upon its size, resulting in a particle charge distribution.

In order to estimate the particles charge, an experimental value of charge to mass ratio, obtained in specific and know conditions, can be compared with the theoretical value obtained integrating the theoretical charge carried by particles that flow in a corona discharge by the classical equation of field and diffusion charging mechanisms. The comparison between theoretical and experimental charge to mass ratio allow an estimation of the particle charge distribution. This is the approach utilized during the

experimentation; the results obtained based on this approach are reported in the following paragraph.

IV.3.2. Experimental results on particle charging

In Figure IV-6 the typical particle size distribution produced by an incense stick is reported.

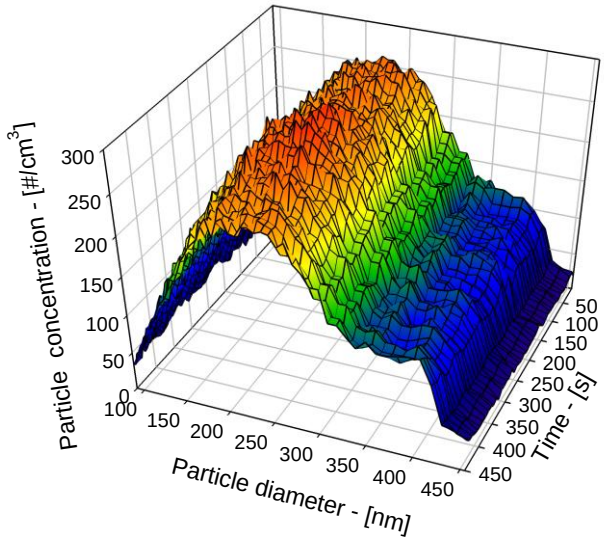

Figure IV-6: Incense typical particle size distribution during burning time

The distribution ranges between 90 and 450nm and presents a peak around 230nm. Particle concentration depends on both air flow rete sent to the incense stick box and the diluting flow rate. Instead, particle size distribution depends only on the flow rate sent to the washer due to its effect on the combustion regime; however, in the investigated range, it is almost constant. Particle size distribution is also quite stable during the combustion.

An example of experimental result obtained following the experimental protocol described in the paragraph III.2.2 is shown in Figure IV-7.

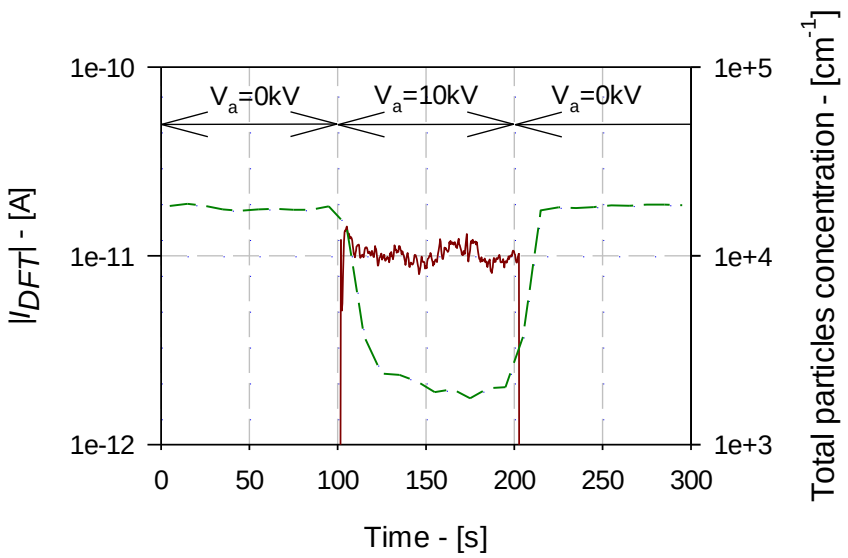

Figure IV-7: Measure of current at DFT and total particle concentration at $Q=2.6m^3/h$, $V_a=10kV$, $L=18mm$

The Figure IV-7 shows a quite constant particle concentration during the first and the last step when no voltage is apply. When the voltage is apply to the wire, the particle concentration decreases while the current measured at the DFT quickly increase up to 10^{-11}A.

The average value of Particle Charge to Mass Ratio (*P-CMR*) can be calculated by the equation (IV-5).

$$P-CMR=\frac{\bar{I}_{\mathrm{Ex-DFT}}}{Q\int_0^{\infty}\bar{\psi}_{p,c}(d_p)\,\frac{\pi {d_p}^3}{6}\,\rho_p d d_p} \qquad \text{(IV-5)}$$

The integral in the equation represents the total mass concentration of particles carried by an air flow rate *Q;* $\bar{I}_{Ex-DFT}$ is, instead, the mean value of the current measured at the dynamic faraday tube when the voltage is apply. The term $\bar{\psi}_{p,c}(d_p)$ is the mean particle distribution that real flow through the DFT and that cannot be directly measured due to problems detailed in paragraph III.2.1. This distribution can be evaluated starting by a mean particle distribution measured in absence of electric field

and correcting it by taking into account the fraction of particles captured in the charging unit. This concept is summarized in the following equation.

$$\bar{\psi}_{p,c}(d_p) = \bar{\psi}_p(d_p)(1 - \eta_c) \quad \text{(IV-6)}$$

The parameter $\bar{\psi}_p(d_p)$ in the equation is the mean particle size distribution measured when no voltage is applied to the discharge electrode and η_C is the particle capture efficiency in the charging unit evaluated by Deutsch-Anderson equation discussed in paragraph II.2.1.2.3.

A theoretical value of particle charge to mass ratio *P-CMR*$_{th}$ can be evaluated using a correlation to theoretically estimate the current $\bar{I}_{DFT}$ in the eq. (IV-5). The charge of the particles acquired in the corona discharge can be predicted by the theoretical field and diffusion charging models, resulting in a theoretical current that should be compared with that measured at the DFT. This current, $\bar{I}_{Th-DFT}$, is calculated with the formula (IV-7).

$$\bar{I}_{Th-DFT} = Q \int_0^{\infty} \bar{\psi}_{p,c}(d_p) q_p(d_p)\, dd_p \quad \text{(IV-7)}$$

Where $q_p(d_p)$ is the charge of a particle of diameter d_p calculated with the equation (II-15).

Tests, for a total of 45 experiments, were carried out varying the high voltage applied to the wire from 9.2 to 12kV, the air flow rate from 2 to 2.7m^3/h and the length of the discharge electrode in the range of 18 - 100 mm. The variations of the operating variables essentially influence the value of two fundamental parameters: the particle residence time in the corona discharge t_r and the ionic concentration N_i. The increase of both variables produces higher particle charge levels. The experimental results are than reported in function of the product of the two parameters as shown in Figure IV-8, where experimental and theoretical results of *P-CMR* are shown.

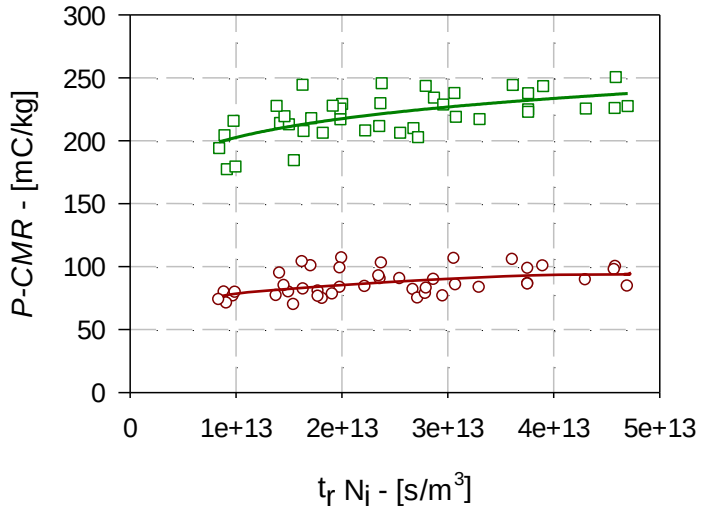

Figure IV-8: Experimental (○) and theoretical (□) results on particle charge to mass ratio. The two lines represent the data regressions

In Figure IV-8 the circle symbol refers on experimental results elaborate using the equation (IV-5). The trend of these data show an increase coherent to the increase of the product $t_r \cdot N_i$. Theoretical results, the square symbols, also follow the same trend.
It must be pointed out that each experimental or theoretical data summarize the charge of a particle distribution obtained under the specific circumstances of each test. These can slightly change from test to test, resulting in different charge, producing the scattered data that appear in Figure IV-8.

The same result in Figure IV-8 can be also described in terms of Particles Charge to Surface Ratio (P-CSR) defined as:

$$\mathrm{P-CSR} = \frac{\bar{\mathrm{I}}_{\mathrm{DFT}}}{\mathrm{Q}\int_0^{\infty} \bar{\psi}_{\mathrm{p,c}}(\mathrm{d_p})\,\pi \mathrm{d_p}^2\,\mathrm{dd_p}} \qquad \text{(IV-8)}$$

Equation (IV-8) can be used to evaluate both the theoretical and experimental value of *P-CSR* simply considering $\bar{I}_{Th-DFT}$ or $\bar{I}_{Ex-DFT}$ as the mean current. The result of the elaboration is reported in Figure IV-9.

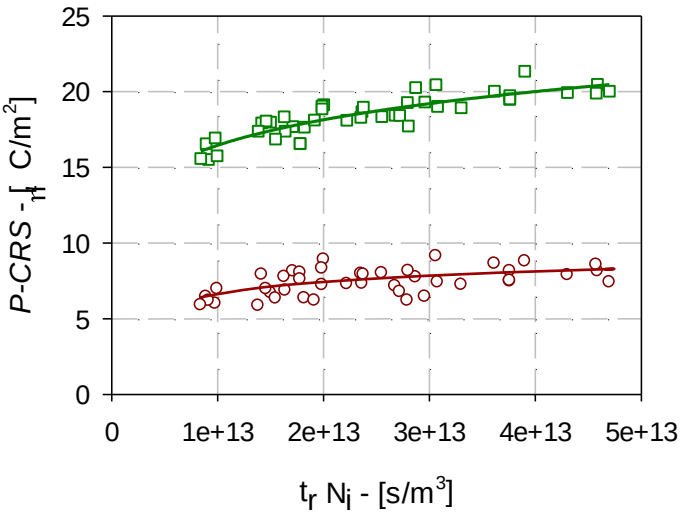

Figure IV-9: Experimental (○) and theoretical (□) results on particle charge to surface ratio. The two lines represent the data regressions

The data in Figure IV-9 are less scattered, demonstrating the importance of the total particle surface on the charging level of the aerosol. This result is consistent with the prediction of the field charging mechanism, which is proportional of the square of the particle diameter.

Both the results reported for *P-CMR* and *P-CSR* show an overestimation of the theoretical model respect to the experimental results. In order to quantify the difference between the results, the ratio of experimental and theoretical data can be considered in function of the product $t_r \cdot N_i$. This is done by comparing the ratios *Exp. P-CMR/ Theo. P-CMR* and *Exp. P-CSR/ Theo. P-CSR*. In both cases, after simplifications, these ratios become equal to the ratio between $\bar{I}_{Ex-DFT}$ and $\bar{I}_{Th-DFT}$ because the total particle mass and the total particle surface in the equations (IV-5) and (IV-8) simplifies. In the following the ratio between experimental and theoretical *P-CMR* are reported in function of the product $t_r \cdot N_i$, the experimental mean current $\bar{I}_{Ex-DFT}$ vs theoretical mean current $\bar{I}_{Th-DFT}$ is reported too.

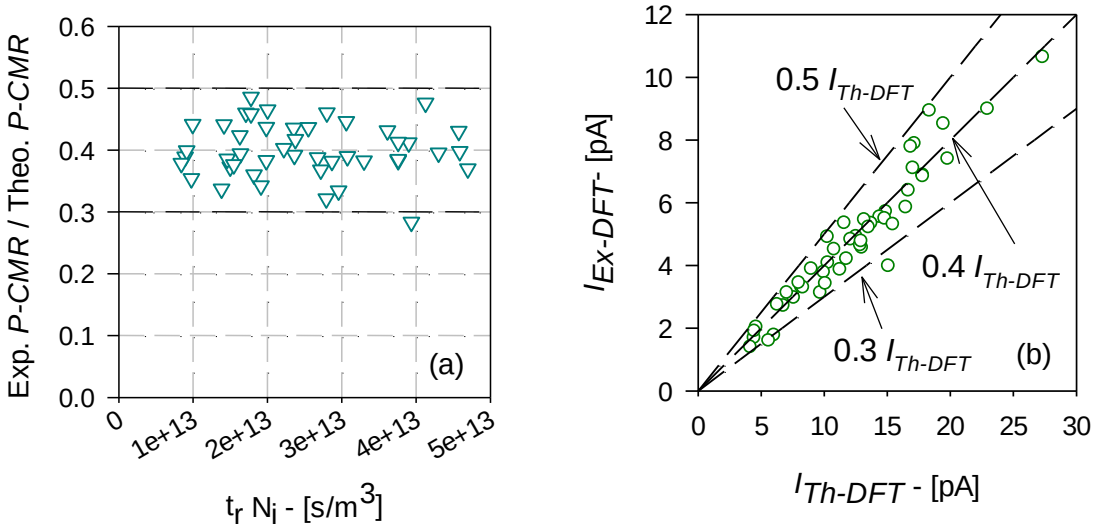

Figure IV-10: Ratio of experimental and theoretical particle charge to mass ratio in function of the product of the residence time and ion concentration (a), and experimental values of mean current measured at the DFT vs. the predicted values obtained by equation (IV-7) (b)

Both the results in Figure IV-10 provide the same information: the theoretical model tends to overestimates the experiments for a multiplicative factor ranging between 0.3 and 0.5. This gap can be related to an overestimation of the particle charge predicted by field and diffusion charging, that are simplified models and should be effected by errors (for example the diffusion model is accurate to within a factor of two in the range of for $Ni \cdot tr$ examined [35]). In order to align theoretical results on the experimental one, a correction factor ω ranging between 0.3 and 0.5 can be used to the models of particle charging. Than the charge on a particle of diameter d_p can be estimated as:

$$q_p(d_p) = \omega[q_f(d_p) + q_d(d_p)] \qquad \text{with } 0.3 < \omega < 0.5 \qquad \text{(IV-9)}$$

The equation (IV-9) therefore adopted the classical equation of field and diffusion charging, with an experimental correction factor that will be utilized to estimate the charge of the particles traveling through the charging unit.

This approach, in practice, corresponds to spread uniformly the overall difference between theoretical prediction and experimental results on the entire particle size distribution. This means that a certain particle is charged to a level that corresponds to 0.3-0.5 times the theoretical value independently on its size. Of course, this ratio can be different from two particles of different sizes, but the particle size distribution of the incense stick is not wide and this approximation can be considered valid.

Two examples of the theoretical particle charge distribution obtained with the field and diffusion charging modified with the experimental correction factor ω are reported in Figure IV-11.

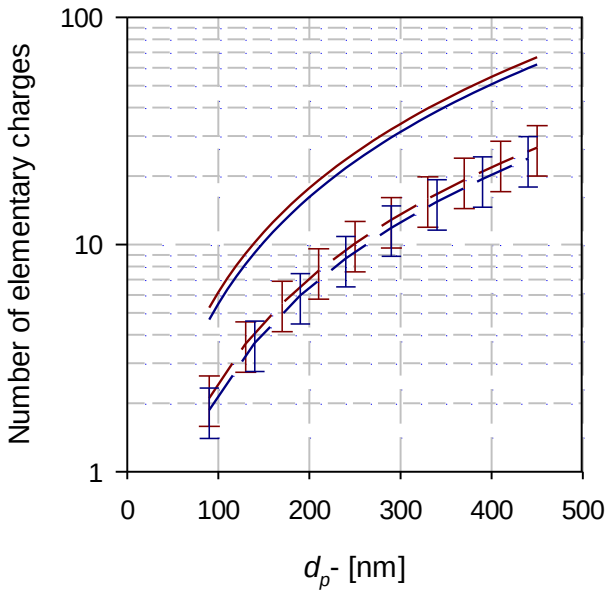

Figure IV-11: Example of original particle charge by equation (II-15) at $t_r \cdot N_i = 4.5 \cdot 10^{13}$ s/m^3 (solid red line) and $t_r \cdot N_i = 9.9 \cdot 10^{12}$ s/m^3 (blue solid lines) and the correspondent corrected particle charge by equation (IV-8) (dash lines)

The dashed lines in Figure IV-11 represents the corrected particle charge distribution that are scaled of a factor of 0.4 with respect the original prediction (solid lines), and the error bars are the uncertainty of the experimental measure corresponding to a 20% of same initial particle charge distribution (ω=0.3 and ω=0.5).

The two dash lines reported in Figure IV-11 are representative of the two extremes of particle charging investigated. In spite of the variation of all the operating variables (voltage applied, length of the wire and air flow rate) the difference between the two curves is small resulting in a low sensibility of the particle charge on ionic concentration and particle residence time in the range investigated. On the one hand, this low sensibility on particle charge distribution upon the operating parameters, limits the range of particle charge investigable for particle abatement experiments, on the other hand, it improves the reproducibility of the tests in the same experimental conditions. Indeed this evidence reduces the experimental errors on the evaluation of the charge particle distribution that is always included between the two dash curves in Figure IV-11.

IV.4. Experimental results on wet electrostatic scrubbing

IV.4.1. Scope of experimental section

The objective of this experimental section is to investigate the influence of the main physical parameters on the wet electrostatic scrubbing. On the basis of the main experimental and theoretical results of literature, the main physical parameters that can influence the submicron particle abatement are:

- Droplet electric charge – q
- Droplet diameter – D
- Droplet concentration in the reactor – N
- Particle size - d_p
- Particle concentration - n
- Particle electric charge - q_p

The influence of the aforementioned variables on the particle abatement was systematically investigated.

In particular, tests were carried out at ambient pressure, temperature and humidity and for one particle charge distribution. Indeed, the air temperature and humidity level are two important parameters due to their influence upon phoretic contribution. However, the effects of these two variables are important only in presence of high temperature and vapor fraction gradient. In these conditions the droplet evaporation is promoted and the phoretic collection efficiency can be significant. Both phoretic and droplet dynamics determine the final results of scavenging tests in a complex way, so that, in these tests, it was decided to avoid these additional effects and to focus attention only on the electro-hydrodynamics interactions only. Therefore, tests were carried out at ambient temperature (T_R≈15-25°C), and humidity levels in the range of HR≈18-22%. In this case, a reliable comparison with classical scavenging models is possible. Further details on the effect of the both temperature and humidity on droplet evaporation are reported in paragraph IV.4.2

With reference to the particle electric charge, the paragraph IV.3.2 was concluded with a modified particle charge model that is able to estimate the charge acquired by a particle in specific charging conditions. The results also show that the mean experimental error made during the estimation was higher than the variation of the particle charges due to the different charging conditions (see Figure IV-11). Therefore, it was chosen to operate always in the same charging condition that are V_a=9.3kV, L=38mm and Q=2.7m^3/h corresponding to $t_r \cdot N_i \approx 1.0 \cdot 10^{13}$s/m^3, that are about the lower limit for particle charging. This operating condition was also chosen with the objective to minimize possible adhesion problems in the sampling tube connected to the particle size analyzer.

In order to model the experimental results obtained on particle abatement, the models presented in the paragraph II.2.1 need to be adapted to the experimental system; this elaboration is presented in the following paragraph. In the subsequent paragraph, the experimental data obtained on particle abatement are presented and the results obtained are compared with theoretical predictions.

IV.4.2. Lab-scale WES modeling

In the paragraph II.2.1.3, the equations to model the abatement of particles in wet electrostatic scrubber were reported. The model predicts that particle scavenging rate is proportional to the particle concentration, resulting in an exponential decay trend during scrubbing time that, in the case of the batch reactor, represents the duration of the test.

All the complexity of the modeling is resumed in the scavenging coefficient, in the equation (II-27), which is valid for a generic droplet size distribution. In the case of single droplet size the scavenge coefficient can be simplified as follow.

$$\Lambda(d_p) = \frac{\pi}{4}(D + d_p)^2\left[U_d(D) - u(d_p)\right]E(D, d_p)N \qquad \text{(IV-10)}$$

The parameter *N* in the equation (IV-10) represents the droplet concentration in the reactor; $u(d_p)$ is the particle velocity in the reactor, that is formally a function of its size, and $U_d(D)$ is the droplet velocity. This latter parameter can vary during the falling of the droplet up to reach a stationary condition, but $U_d(D)$ can also vary due to droplet evaporation as the consequent of a different drag force on the droplet. Therefore, the scavenging coefficient should be considered a function of the axial coordinate of the reactor. In the following, some evidences will allow to reconsider this assertion.

Due to their small dimensions, the particle velocity in the reactor can be approximated to the air velocity; the air mixing in the reactor is due to the recirculation of the gas stream sampled to the LAS 3340. This velocity was experimentally measured by the anemometric probe and it results in a range of about 0.05 and 0.10m/s. These values, can be neglect if compared with droplet velocity; therefore, the droplet-particle relative velocity can be approximated by droplet velocity resulting then $U(D) \approx U_d(D)$.

The droplet concentration in the reactor, *N* in the equation (IV-10), can be calculated as:

$$N = \frac{6\,Q t_d/\pi D^3}{H_R \pi {D_R}^2/4} \tag{IV-11}$$

Where t_d is the droplet residence time in the reactor and can be calculated evaluating the dynamic of the falling droplet based on the models reported in paragraph II.2.1.1.1. The model provides the resolution of a system of four differential equations in order to calculate the temperature, the mass, the velocity and the position of a droplet during scrubbing time.

The initial conditions for the motion of the droplet (eq. (II-2) and (II-3) the thermal balance (eq.(II-4)) and the mass balance (eq.(II-5)) are:

$$X|_{t=0} = H_R \tag{IV-12}$$

$$v_i|_{t=0} = 0\ m/s \tag{IV-13}$$

$$T_d|_{t=0} = T_{d,0} \tag{IV-14}$$

$$m_d|_{t=0} = \frac{\pi {D_0}^3}{6}\rho_w \tag{IV-15}$$

The system of differential equations was solved under the assumptions of the classical rapid mixing model reported in Table II-1. A typical result of the model in terms of droplet velocity in the reactor is described in Figure IV-12.

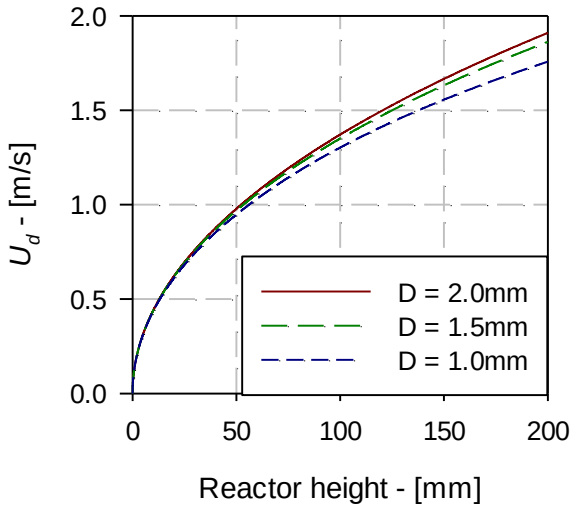

Figure IV-12: Droplet velocity along the axis of the reactor for three droplet size evaluated at T_R=25°C, T_d=25°C and HR=20%

In Figure IV-12 the falling velocity of three droplet size are reported. The initial conditions are similar of those in which particle abatement was studied. The curves are partially overlapped in the initial step and only in the final stage show some differences.

The very small variation between the falling velocities of different droplet sizes, reduces the possibility of investigating the effect of this parameter on the particle abatement. However, the pertinent literature (see paragraph II.2) revealed that this parameter should not influence the abatement of submicron particles. In order to simplify the effect of droplet velocity on the scavenging coefficient, an average integral is considered.

The very similar falling velocity for the investigated droplet size results in a close droplet residence time-range, which varies from 0.205 to 2.10s for droplet in the range of 2.0-1.0mm respectively. Due to this short time, the variation of droplet temperature and diameter result in small difference respect to the initial values, as shown in Figure IV-13.

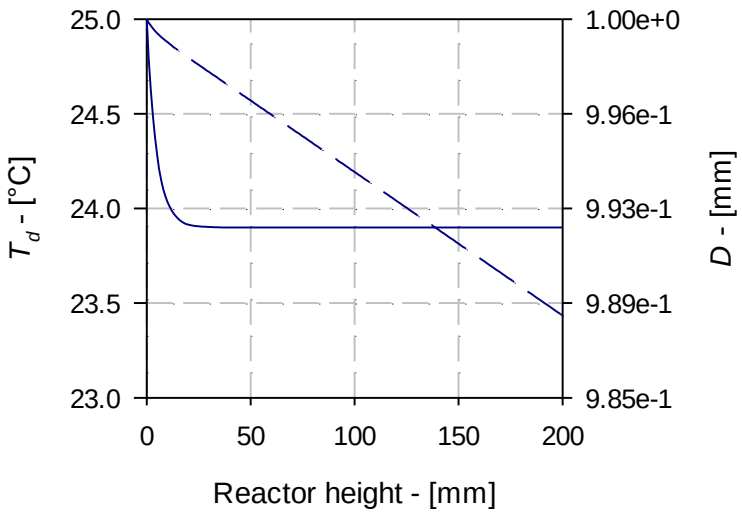

Figure IV-13: Droplet temperature (solid line) and diameter (dash line) along the axis of the reactor for D=1mm evaluated at T_R=25°C, T_d=25°C and HR=20%

In the Figure IV-13, the numerical results on droplet temperature and diameter for an initial droplet size of 1mm are reported; the results for higher droplet size are not

reported because the variation of the two parameters is less evident. The droplet temperature trend in the Figure (solid line) quickly decreases up to reach a stationary condition, while droplet size linearly decreases during its fall. As a consequence of the evaporation, at the bottom of the reactor the droplet diameter is reduced of only 1.2% of its initial size and the temperature decrease of 1.1°C. Due to this small variation, the droplet evaporation can be neglect and, for the droplet temperature, the stationary temperature can be considered.

Upon the assumption of negligible droplet evaporation and negligible particle velocity, and also simplifying the sum $D+d_p \approx$ D due to the small dimensions of the particle size compared to the droplet diameter, the scavenging coefficient reported in the equation (IV-10) con be further simplified as follow:

$$\Lambda(d_p) = \frac{\pi}{4} D^2 \bar{U} E(D, d_p) N \qquad \text{(IV-16)}$$

In order to evaluate the scavenging coefficient in the equation (III-1), the total collisional efficiency *E* must be calculated. In this study, inertial impaction, directional interception, Brownian diffusion and electrostatic interactions are considered; thermophoresis and diffusiophoresis are negligible at the experimental conditions studied as explained before. The equations to describe the different collisional contributions are reported in Table II-2; with reference to inertial impaction and directional interception, different models are present in literature, although the models reported provide very similar results [73]. In this work equations of Licht and Slinn are adopted, respectively.

IV.4.3. Results and discussion on particle capture

In this paragraph the experimental and theoretical results on particle abatement are reported; the experiment were carried out varying the set up conditions for the charged droplets generator, resulting in different droplet size, charge and concentrations. The charging conditions for the particle were instead kept constant as explained before.

For each test, the particle concentration and size distribution were measured and the results elaborated in order to evaluate the droplet scavenging coefficient for all the particle size analysed, using the methodology discussed in paragraph III.3.1. All the results are inserted in appendix, while in the following a generic test will be introduced and compared with the theoretical prediction. The comparison among the results will be instead carried out on selected particle size.

Before reporting the results on particle abatement due to charged particles, one test executed without voltage applied to the particle charging unit is shown in Figure IV-14.

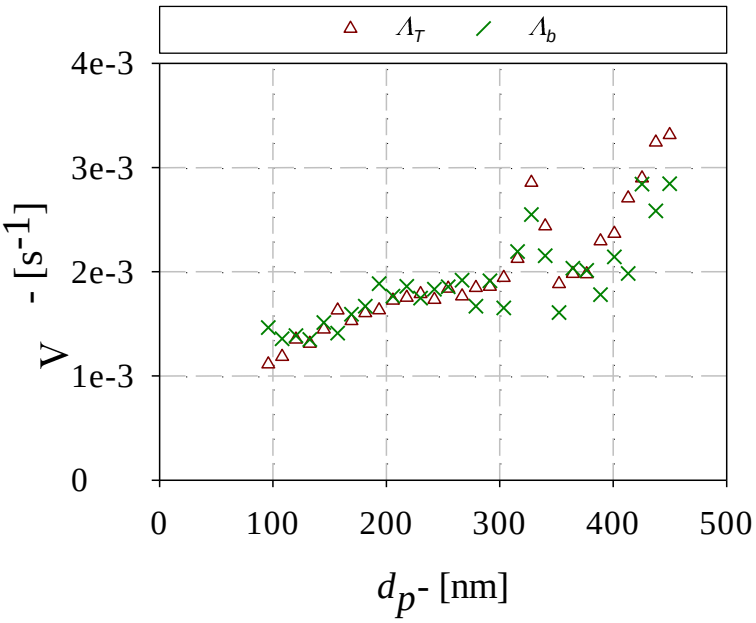

Figure IV-14: Experimental total and baseline scavenging coefficients. Experimental conditions: uncharged particles, D=0.9mm, q=79.4pC, N≈11000drops/m^3

Figure IV-14 summarizes the results of total and baseline scavenging coefficients (respectively triangle and × symbols) in presence of charged droplets and uncharged particles: if the particles are not charged the baseline contribution is always much higher than the droplet contribution on particle abatement and the difference between total and baseline scavenging coefficient, to evaluate the droplet contribution, cannot

be computed. Experiments at zero voltage applied to the charged droplets generator were not tested since in this condition the electrospray produces droplets too big in size and too small in falling frequency, making impossible to assess a difference between total and baseline scavenging coefficients.

The droplet contribution is instead quantifiable if the particles are charged. In Figure IV-15 the scavenging coefficients obtained in the same conditions used in Figure IV-14, but with charged particles, are reported.

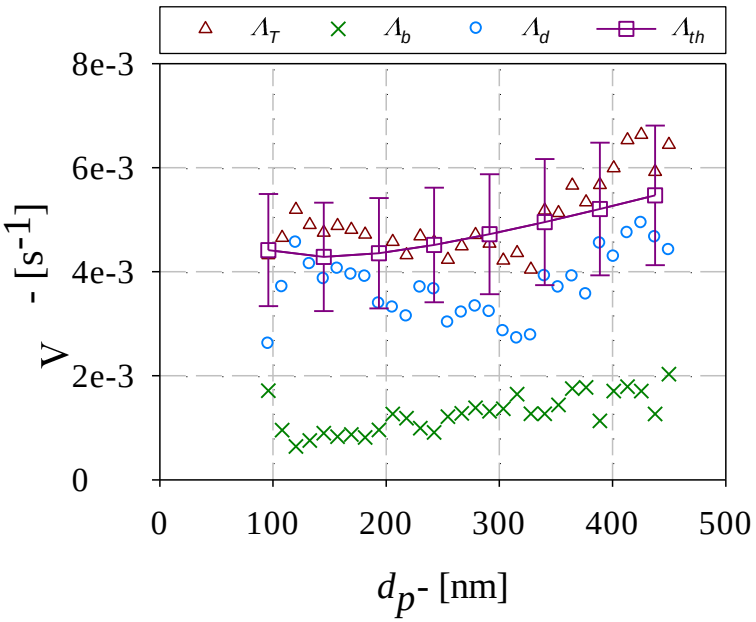

*Figure IV-15: Experimental and theoretical scavenging coefficients. Experimental conditions: charged particles, D=0.9mm, q=79.4pC, N≈11000drops/m^3.*Other conditions are reported in Appendix-Report 1

The presence of opposite charges on the particles produce strong differences between total and baseline scavenging coefficients; in fact total scavenging coefficient is higher than baseline scavenging coefficient, making possible to evaluate the droplet scavenging coefficients (circle symbols). These data show a well-defined decreasing trend in the range 120-300nm, while the trend increase in the range 300-450nm. It must be considered that the trend shown for the Λ_d is not always the same; sometimes the data monotonically increasing, while in other case, it presents a minimum in the

range 250-350nm. These differences are probably due to an incorrect estimation of the particle charging distribution.

In Figure IV-15, the theoretical prediction of the scavenging coefficients, obtained under the assumption discussed in paragraph IV.4.2, are reported too. The errors bars in the theoretical results summarize the uncertainty related to the particles charge and droplet size. Despite some differences, in Figure IV-15 experimental data and theoretical prediction show a good matching.

Experimental and theoretical results can be also compared in terms of particle size distribution at different scrubbing time; this matching is of course less precise due to random oscillations measured, but this representation is more immediate. Also in this case baseline and droplet contribution must be split from the total contribution. In order to consider the two contributions on particle abatement efficiency, the following notation is used.

With reference of the data reported in Figure IV-16, initial measured distribution is represented by the sum of red plus white bars in the illustration (a), while the distribution after *t* seconds, in presence of charged droplets, is shown simply by the white bars. Therefore the red bars represent the particle abatement after *t* seconds in the reactor. This portion can be split in two contributions: one due to the baseline contribution, and it is show as green bars in the illustration (b), while the contribution of the droplets is shown as blue bars in the histogram (b).

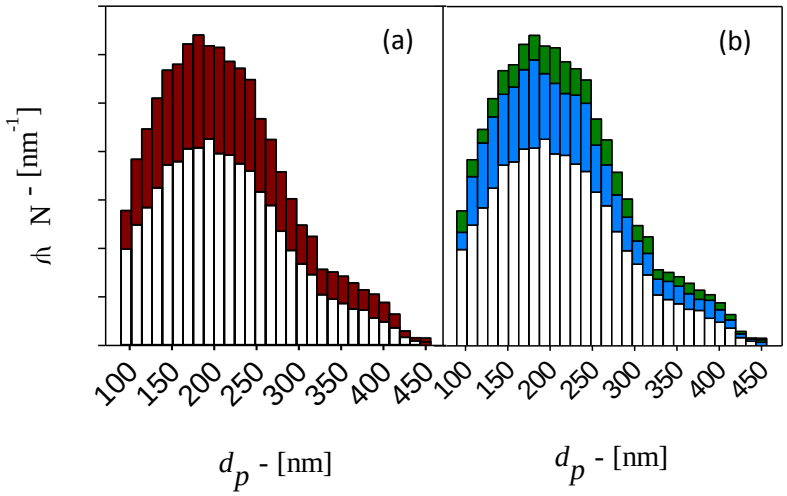

Figure IV-16:(a) Example of droplet initial (red + white bars); (b) particle abatement contribution divided in baseline contribution (green bars) and droplet contribution (blue bars)

The theoretical particle size distribution after *t* seconds from the initial condition can be compared with the white distribution. In this case the baseline contribution, that is not calculate and can be different from tests to tests, must be add to the theoretical prediction; in this case the following equation can be considered:

$$\Psi_{N-th}(d_p, t) = \Psi_N(d_p, 0)\left\{\exp\left[-\left(\Lambda_{th}(d_p) + \Lambda_b(d_p)\right)t\right]\right\} \qquad \text{(IV-17)}$$

Where $\Psi_N(d_p, 0)$ is initial experimental normalized distribution, while $\Psi_{N-th}(d_p, t)$ is the predicted distribution after t seconds of scrubbing.

In equation (IV-17) the experimentally determined baseline scavenging coefficient $\Lambda_b(d_p)$ was added to the theoretical scavenging coefficient $\Lambda_{th}(d_p)$ in order to consider the abatement due to the baseline contribution.

In Figure IV-17 the experimental and theoretical data, presented in Figure IV-15, are reported in terms of particle size distribution for four elapsed time from the starting time.

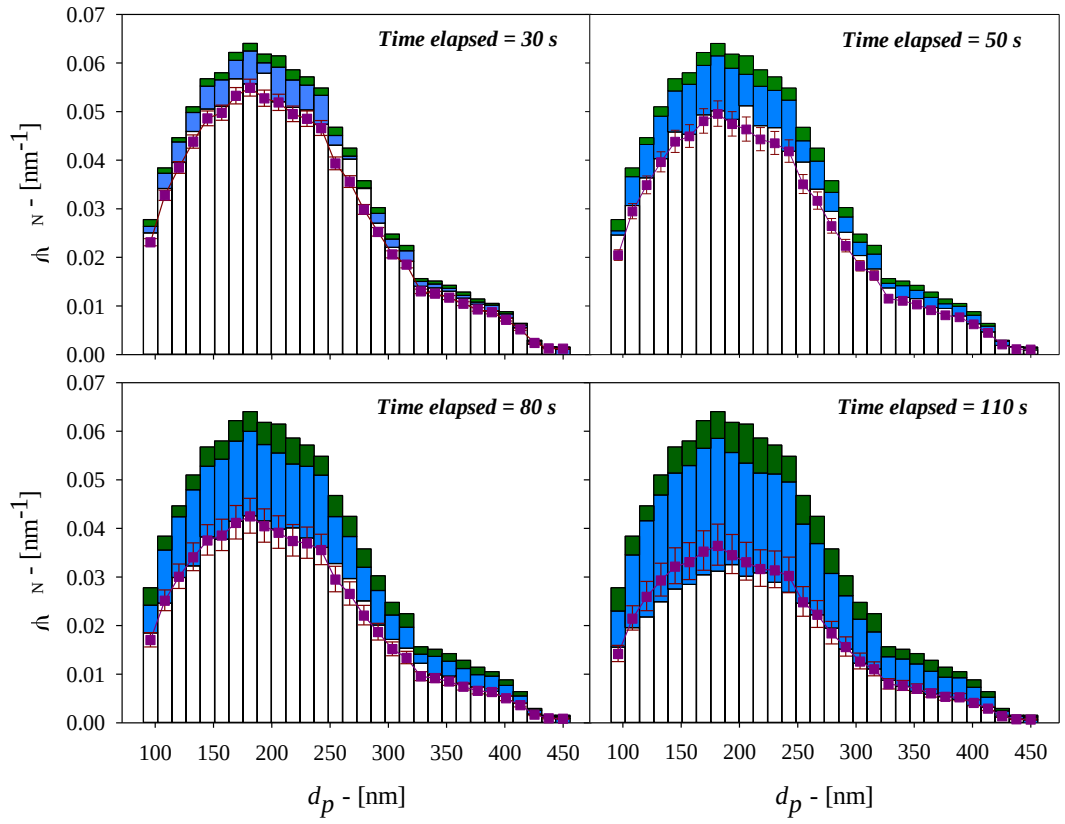

Figure IV-17:Theoretical (purple point) and experimental distribution after four time elapsed from initial distribution. Green bars=baseline contribution, blue bars=droplet contribution, white bars=distribution after the time elapsed. Experimental conditions: charged particles, D=0.9mm, q=79.4pC, N≈11000drops/m^3. Other conditions are reported in Appendix-Report 1

In Figure IV-17 the theoretical distribution is reported as purple points; the errors bars are related to the uncertainty on particle charge calculation. Also in the new representation of the data, the theoretical model shows a good prediction of the experimental data: the theoretical points follow the white bars during the scrubbing time with random oscillations around experimental values.

It is worth to analyse the droplet collision efficiency to evaluate which are the main theoretical contributions on particle capture as shown in the following.

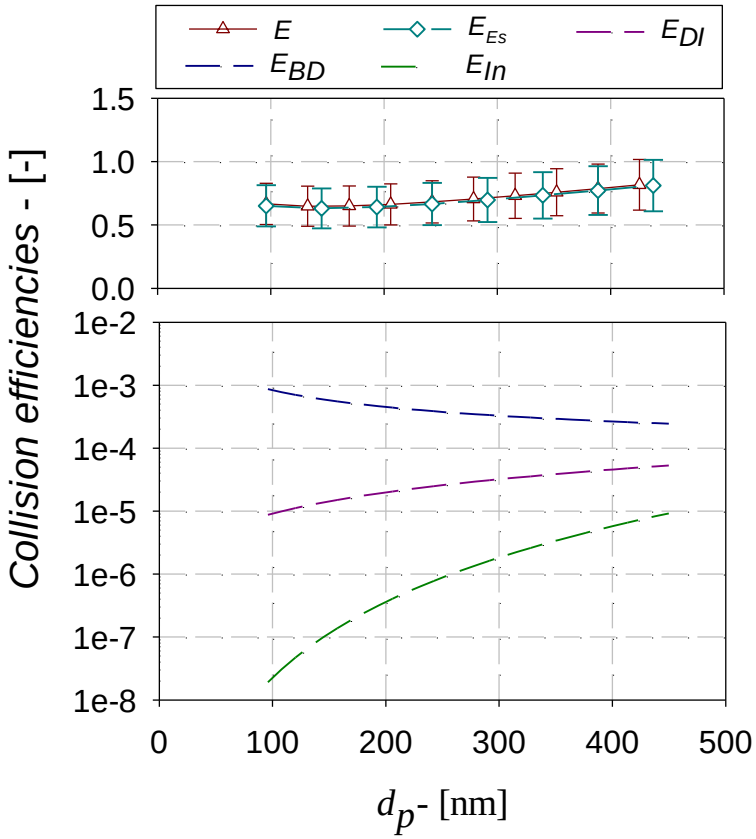

Figure IV-18:Collisional efficiencies for the results in Figure IV-15. Experimental conditions are reported in Appendix-Report 1

In Figure IV-18 the electrostatic, Brownian, interception and impact contributions are reported as dashed line. The uncertainty on particle charge estimation is reported in the electrostatic contribution as errors bars. The sum of all the contributions represents the total collision efficiency and is reported as a solid line. In the Figure V-18, Brownian contribution (blue line) shows a decreasing trend with the increase of particle size; on the contrary interception (purple line) and impaction (green line) contributions increase with particle diameter. Moreover, in this range of particle size, interception is higher than impact [67]. Nevertheless in the particle size range investigated, the electrostatic interactions represents the most important contribution to particle abatement resulting at least two orders of magnitude higher of all other contribution exanimated, and being almost overlapped with the total collision efficiency. This result was found for all the experimental tests.

Therefore, substituting the expression of the electrostatic interaction (eq. (II-47) in the scavenging coefficient previously obtained (eq.(IV-10)), a simplified scavenging coefficient can be evaluated, for a droplet concentration *N* of constant droplet size on the assumption of negligible droplet evaporation, as:

$$\Lambda(d_p) \cong \frac{4\, K_c\, C_c\, q\, q_c\, N}{3\, \mu\, d_p} \qquad \text{(IV-18)}$$

It is worth to note that the equation predicts a linear dependence between the scavenging coefficient and both droplet and particle charge, on the contrary the particle size show an inversed proportionality.

This last consideration seem to be in contrast with the result shown Figure IV-15, where the scavenging coefficients increase with the particle size. However, it should be considered that particle size is also affected on its charge with dependence more than linear as shown in Figure IV-11. As consequence, the increase of d_p produces an increase of the actual q_p/d_p ratio in the investigated conditions.

Unexpectedly, in the equation (IV-18) the droplet size does not appear and therefore it apparently does not influence the scavenging coefficient. However, its effect of droplet size is included in the droplet concentration *N* and in the droplet charge *q*.

Since the equation (IV-18) predicts a linear dependence on droplet charge, it should be useful to compare the test reported in Figure IV-15 with another experiment executed at different droplet charge level. In this test, the particle charge is *q*=100.8 pC and *N*=9417#/m^3 but the droplet size is the same of the previous case.

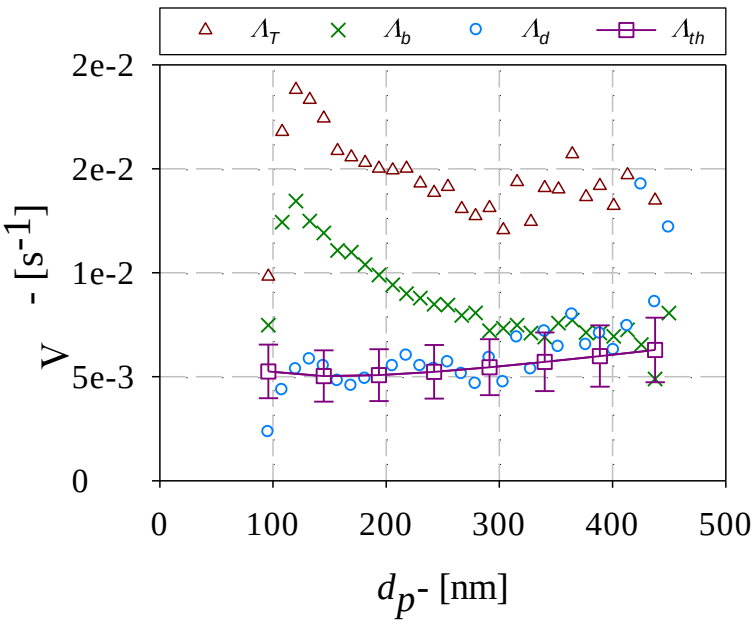

Figure IV-19:Experimental and theoretical scavenging coefficients. Experimental conditions: charged particles, D=0.9mm, q=100.8pC, N≈9500drops/m^3.Other conditions are reported in Appendix-Report 6

First of all, it is worth to note that in Figure IV-19 baseline scavenging coefficient Λ_b are higher than those reported in Figure IV-15. This is probably due to the higher voltage applied to the electrospray in the latter case: increasing the voltage the electric field established between the needle tip and the grounded ring are more intense and this effect can attract more particle that are charge at opposite polarity. Furthermore, Figure IV-19 shows that the theoretical predictions are consistent with the experimental droplets scavenging coefficients Λ_d.

In order to compare the two experiments reported in Figure IV-15 and Figure IV-19, the variation of droplet concentration and charge must be considered. As consequence the theoretical and experimental droplet scavenging coefficient for the two tests examined, are rearranged in terms of single droplet scavenging coefficients, simply dividing Λ_d and Λ_{th} on droplet concentration as reported in Figure IV-20.

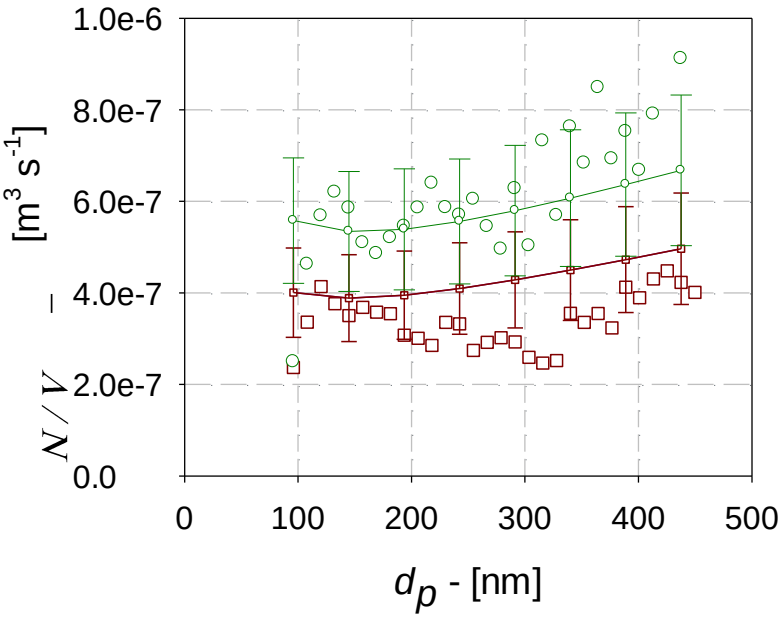

Figure IV-20: Theoretical (lines and error bars) and experimental values (points) of a single droplet scavenging coefficients for droplet charge q=100.8pC (circle points) and q=79.4pC (square points)

This figure summarizes the experimental and theoretical results of the scavenging coefficient of a single droplet of 0.9mm at the two charge levels. By this way, the actual difference between the two set of data is only related to the droplet charge level. The results confirm the linear dependence of the scavenging rate on the droplet charge: increasing the droplet charge to 25% (from 0.8E-7 to 1.0E-7mC) the droplet scavenging coefficient increase of about the same percentage.

The linearity of the scavenging coefficient on the droplet charge can be also verified for all the tests. For simplicity, three particle sizes were considered and experimental and theoretical results plotted in function of droplet charge. The results are displayed in Figure IV-21.

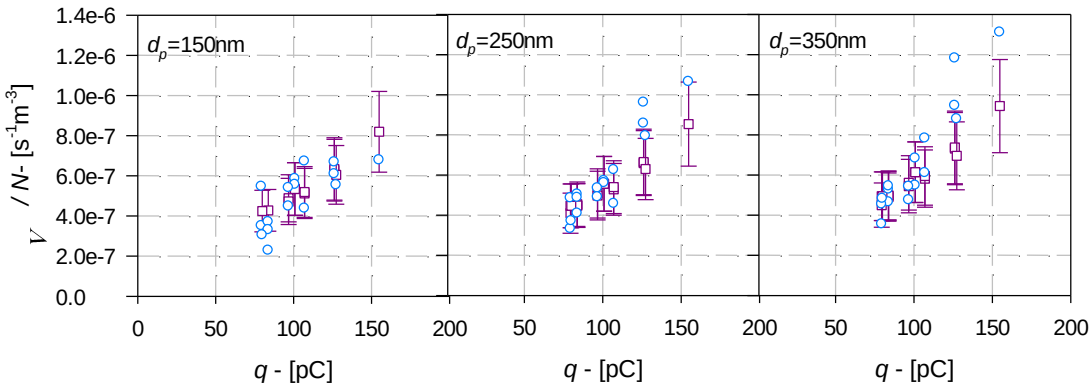

Figure IV-21:Effect of droplet charge on single droplet theoretical (square symbols) and experimental (circle symbols) scavenging coefficient for three particle size

Figure IV-21 summarizes the result obtained for all tests in terms of single droplet scavenging coefficient and for three particle size: 150, 250 and 350nm. The theoretical points show a linear dependence of the parameter Λ/N on the droplet charge, a trend that is also follow by experimental points, although sometimes the model prediction underestimate the experimental data.

The linearity of the scavenging coefficient on droplet concentration should be verified by plotting the data in terms of Λ/q on droplet. The theoretical and experimental results for three particle size are reported in Figure IV-22.

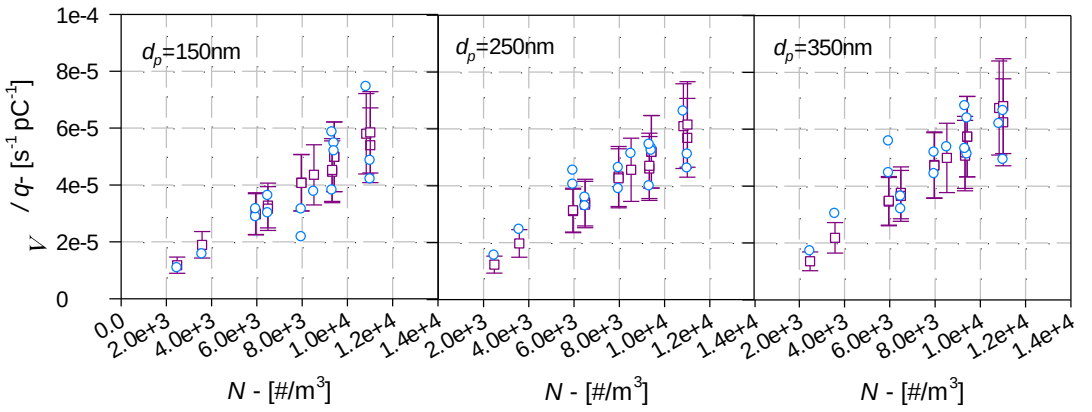

Figure IV-22:Effect of droplet concentration on theoretical (square symbols) and experimental (circle symbols) values of Λ/q for three particle size

The data reported in Figure IV-22 confirm the prediction of equation (IV-18): theoretical (square symbols) and experimental data (circle symbols) show a linear dependence on droplet concentration.

Finally, the data reported in the last two figures can be also elaborated in order to evaluate the collection efficiency in the wet electrostatic scrubber. Following the simplification of the theoretical model in the equation (IV-18), the particle capture efficiency can be written as:

$$\eta(d_p) \cong 1 - exp\left(-\frac{4\,K_c\,C_c\,q\,q_c\,N}{3\,\mu\,d_p}\,t_p\right) \qquad \text{(IV-19)}$$

Where the terms in the round brackets represent the scavenging coefficient multiplied for the particle residence time in the scrubber t_p.

Therefore, in the investigated particle size range, experimental particle abatement efficiency can be calculated and compared with the theoretical results using the simplified equation (IV-19). For each particle size and its charge, the particle abatement efficiency is a function of q, N and t_p; the addition of the further variables t_p make difficult to represent and compare the data. To overcome this problem it was chosen to plot the particle abatement efficiency after the fall of a fixed number of droplets for all the tests. When water flow rate and droplet size in know, it is possible to calculate the time corresponding to the fall of Ω droplets using the following equation.

$$t_p = \frac{\pi D^3}{6\,Q}\Omega \qquad \text{(IV-20)}$$

The equation (IV-20) should be inserted in the equation (IV-19) to calculate the theoretical collection efficiency.

It is worth to note that the product of droplet concentration N, defined in the equation (IV-11), and the time t_p, expressed by equation (IV-20), results in:

$$Nt_p = \frac{\Omega\,t_d}{H_R \pi {D_R}^2/4} \qquad \text{(IV-21)}$$

The product $N{\cdot}t_p$ simplifies in: reactor dimensions at the denominator (that are constants), droplet residence time in the reactor and the fixed number of falling droplet at the numerator. As discussed in the paragraph IV.4.2, the influence of t_p on droplet size can be neglected; therefore fixing the number of falling droplet, practically consists into fixing the product $N{\cdot}t_p$ for all the tests. As a consequence it is possible to compare the particle abatement efficiency as a function of a single variable, the droplets charges, after a constant number of falling droplets.

In order to compare the theoretical and experimental results in terms of particle capture efficiency, the experimental concentration must be filtered to consider only the abatement due to charged droplet. Therefore the experimental contribution is calculated on the basis of the following equation.

$$\eta_{exp} = 1 - \exp(-\Lambda_d\, t) \qquad \text{(IV-22)}$$

The comparison between theoretical and experimental data is reported in Figure IV-23.

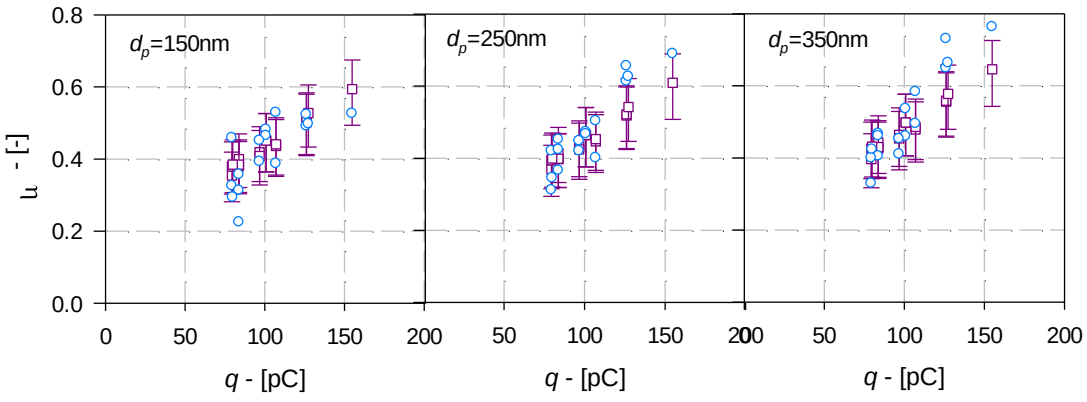

Figure IV-23:Theoretical (square symbols) and experimental (circle symbols) particle collection efficiency in the reactor after the falling of 40000droplets, in function of droplet charge and for three particle size

In Figure IV-23, the theoretical data obtained by eq. (IV-19) and experimental particle collection efficiency, resulting by (IV-21), after the falling of 40000 droplets are reported for three particle size.

The efficiency reported range between 20 and 80% with higher values for the higher droplet charge. Coherently to the theoretical prediction, the experimental data show an increase of the efficiency by increasing the droplet charge.

CHAPTER V - Conclusions

In the present work, a batch lab-scale WES device was designed, constructed and operated, in order to evaluate the effects of the main physical variables on the particle abatement. An electrospray exerted in dripping mode was used to produce monodispersed droplets; a wire-tube corona discharge was used to charge the particles produced by an incense stick. Due to intrinsic features of the experimental set-up, the research required two additional experimental set-up and procedures, in order to characterize droplet charges and sizes as well as the charges acquired by the particles.

The results of these preliminary activities were used to determine the physical parameters required to achieve a description of the experiments on wet electrostatic scrubbing of the particulate matter in different operating conditions.

The experiments demonstrated that the particle abatement rate of wet electrostatic scrubbing follows a first order mechanism in both particle and droplet concentration. This result is consistent with the theoretical prediction [67] and allows to consider a first-order rate equation in particle concentrations with a proportionality constant that coincides with the theoretical definition of the scavenging coefficient, Λ. This result, coupled with a dedicated experimental activity, drives to the conclusion that particle abatement due to the wet electrostatic scrubbing and contribution of the intrinsic device properties (baseline contribution), can be suitably determined. Therefore, the experimental results on wet electrostatic scrubbing in different operating condition can be better compared in terms of scavenging coefficient rather than in terms of global particle abatement efficiency.

Preliminary tests on particle abatement demonstrated that in presence of charged droplet and uncharged particles the capture velocity are very slow and the contribution of wet electrostatic scrubbing cannot be distinguished from that of the baseline, so that the actual particle abatement due to charged droplets cannot be measured. This means

that, in the investigated conditions, the effects of image charge on uncharged particle do not have a significative role on particle capture.

On the contrary, the experimental results highlighted the importance of the electrostatic interaction between droplet and particles when both of them are charged at opposite polarity. In these conditions, the Coulomb electrostatic attraction results the most important particle abatement mechanism. This result is also consistent with former evidences [55, 64, 65].

The experimental data were described using the classical theoretical model based on the particle population balance with additive collisional efficiencies, and the model is consistent with experimental data. On the basis of this result a simplified equation can be derived to calculate the particle abatement efficiency in our experimental rig:

$$\eta(d_p) \cong 1 - exp\left(-\frac{4\,K_c\,C_c\,q\,q_c\,N}{3\,\mu\,d_p}\,t_p\right) \qquad \text{(V-1)}$$

The validity of the equation (V-1) was demonstrated under different experimental conditions summarized in Table V-1.

Investigated physical variables	***Range***
Droplet charge to mass ratio, *D-CMR*	0.1-0.3 mC/kg
Droplet charge, *q*	70-160pC
Droplet diameter, *D*	0.9-1.3mm
Droplet concentration, *N*	3500-11000drop/m^3
Particle diameter, d_p	90-470nm
Total particles charge to mass ratio, *P-CMR*	≈75mC/kg
Number of elementary charge on particles, q_p/e	1-30

Table V-1: Range of the physical variables investigated at ambient temperature and ≈20% of relative humidity

The equation (V-1) was derived on the assumption of negligible droplet evaporation and negligible phoretic contributions; these conditions are common at ambient temperature and humidity, under which experiments were performed. Moreover the equation is referred to a single droplet size and *N* represents the concentration of droplets in the scrubbing vessel. If a dispersed spray was used, the total particle

capture efficiency should be integrated over the droplet size distribution and eq. (V-1) becomes:

$$\eta(d_p) \cong 1 - exp\left(-t_p \int_0^{\infty} \frac{4\, K_c\, C_c\, q(D)\, q_c\, \psi(D)}{3\, \mu\, d_p}\, dD\right) \qquad \text{(V-2)}$$

Therefore, equation (V-2) can be used to estimate particle abatement efficiency when a charged spry distribution is used to capture charges submicron particle at opposite polarity.

Regardless of droplet size distribution, the particle abatement efficiency depends upon three main parameters that are:

1. The ratio q_c/d_p - that depends upon the particle size that must to be captured and on the charge acquired by the particles. This charge can be related on the efficiency of the charging unit.
2. The product $q \cdot N$ – that mainly depends on the characteristics of the nozzle used and on the charging mechanism involved; the droplet residence time in the reactor is also important in order to maximize droplet concentration.
3. The particle residence time t_p – that depends on the geometry of reactor and on the air flow rate.

It must be pointed out that the design of the nozzle, and its droplet charging mechanism, represent a crucial step in the optimization of wet electrostatic scrubbing for industrial applications, because, at a given water flow rate, droplet charges and size distribution (and therefore the droplet numerical concentration in the reactor) depend upon the nozzle specifications. In particular, if the nozzle produces finer droplets, their concentration increases and, therefore, the particle abatement increases, as show to the equation (V-1) and (V-2). The reduction of the droplet size is generally considered as a way to increase the scrubbing efficiency and reduce the water consumption [67]. Nevertheless, the reduction of droplet size also reduces the maximum charge limit, which corresponds to the Rayleigh limit showed in Figure V-1.

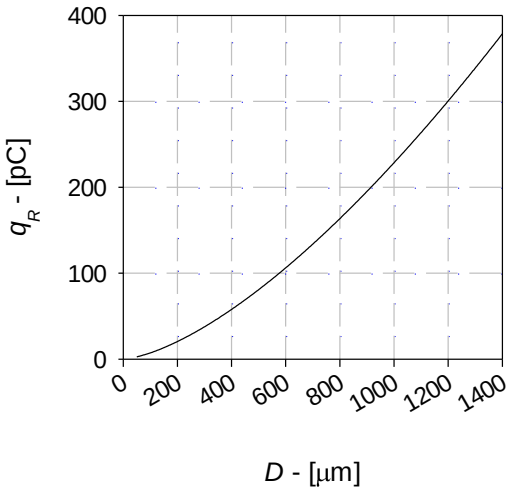

Figure V-1: Rayleigh charge limit in function of the water drop diameter

The Figure V-1 reports the maximum charge that a droplet could transport before it explodes in finer droplets. This is however a theoretical limit, but in practice charge levels for industrial nozzle up to 20-30% of Rayleigh limit are difficult to produce [67]. It must be noticed that during the experiments the lower droplet charge analysed was 70pC, a charge that cannot be supported by droplets finer than 500 µm.

According to the definition of Rayleigh limit charge, the reduction of the droplet size increase the droplet concentration (which is beneficial for the scrubbing efficiency) but it should reduce the droplet charge, which is detrimental for the scrubbing efficiency.

In order to evaluate the optimal conditions for wet electrostatic scrubbing, the equation (V-1) can be plotted as iso-efficiencies as a function of the droplet charge q and the number of scrubbing droplets, given by the product $N \cdot t_p$. The use of these three parameters encloses all the variables involved in the sizing of both scrubber dimensions and nozzle characteristics. In Figure V-2 is reported the theoretical particle abatement efficiency in function of q and $N \cdot t_p$, for particle of 250nm charged at 5 elementary charges; this charge level is very simple to obtain in a wire-tube charging unit and does not require too high level of corona discharge voltage. The equation (V-1) does not depend on droplet size, so some experimental points (discussed in Figure IV-23) were also reported in Figure V-2 for comparison.

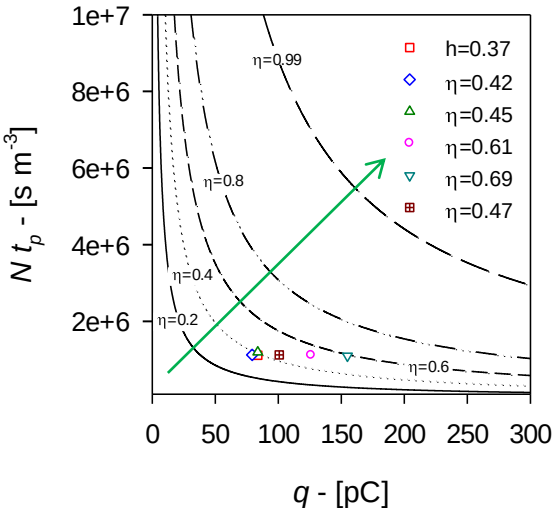

Figure V-2: Particle abatement efficiency calculated with the equation (V-1) in function of the product between droplet concentration N and droplet residence time t_p in function of the droplet charge q. The particle size considered is dp=250nm and its charged is q_p=5e Experimental points presented in Figure IV-23 are reported too

The Figure V-2 shows that the values of iso-efficiency follows a hyperbolic pattern, so that for low droplet charge, the product $N \cdot t_p$ must to be significantly heighten up to reach larger particle abatement efficiency; the opposite behaviour is valid for low values of $N \cdot t_p$. Therefore the optimal values of q and $N \cdot t_p$ are in the elbow of the curves as reported in Figure V-2.

Although in the industrial practice the optimal properties of the spray must be specifically tailored on the given application; as a general consideration, the optimal design of the electrified nozzle should follow the maximization of the product $q \cdot N$ for a fixed water flow rate. Such water flow rate can be either limited by spray properties, or by other considerations (droplet evaporation, optimal liquid distribution over the scrubber section, droplets entrainments, performances of contemporaneous absorption processes etc.) and must be fixed for each specific case. Starting from this selection, properties of the electrified spray can be suitably defined according to the aforementioned criteria for maximization of particle efficiency.

Acknowledgment

This work is financially supported by: the Italian Ministero dello Svilluppo Economico within the CNR-MSE partnership programme: Decreto MAP 23 marzo 2006 - CARBONE PULITO; the Programma FARO project: Sviluppo di dispositivi a getto sintetico per diverse applicazioni tecnologiche, of the University of Naples, Federico II, and by the CRUI-British Council British-Italian Partnership Programme For Early Career Researchers - Development of a High Efficiency Clean-up Technology to Reduce Submicron Particle Emissions from Combustion Processes and Diesel Engines Exhausts (2009-2011).

The author thanks Dr. Claudia Carotenuto for her collaboration and Dr. Radu Beleca for its support in the preliminary experimental activities.

References

[1] D. Dockery and C. Pope, Outdoor air I: particulates, Topics in environmental epidemiology, 1997.

[2] V. Vestreng, K. Mareckova, S. Kakareka, A. Malchykhina and T. Kukharchyk, “Inventory review 2007. MSC-W Technical Report 1/07.,” Norwegian Meteorological Institute, Oslo, Norway, 2007.

[3] L. Morawska, S. Thomas, N. Bofinger, D. Wainwright and D. Neale, “Comprehensive characterization of aerosols in a subtropical urban atmosphere: particle size distribution and correlation with gaseous pollutants,” *Atmospheric Environment,* vol. 32, no. 14/15, pp. 2467-2478, 1998.

[4] R. Harrison, M. Jones and G. Collins, “Measurements of the Physical Properties of Particles in the Urban Atmosphere,” *Atmospheric Environment,* vol. 33, no. 309-321, 1999.

[5] J. Shi and R. Harrison, “Investigation of ultrafine particle formation during diesel exhaust dilution,” *Environmental Science & Technology,* vol. 33, pp. 3730-3736, 1999.

[6] J. Shi, D. Evans, A. Khan and R. Harrison, “Sources and Concentration of Nanoparticles (< 10 nm Diameter) in the Urban Atmosphere,” *Atmospheric Environment,* vol. 35, pp. 1193-1202, 2001.

[7] P. Wahlin, F. Palmgren and R. Van Dingenen, “Experimental studies of ultrafine particles in streets and the relationship to traffic,” *Atmospheric Environment,* vol. 35, pp. S63-S69, 2001.

[8] D. Neef, “The Development of a Global Maritime Emissions Inventory Using Electronic Monitoring and Reporting Techniques,” in *18th Annual International Emission Inventory Conference "Comprehensive Inventories - Leveraging Technology and Resouces"*, Baltimore, Maryland, 2009.

[9] L. B. Lester and E. Seskin, “An Analysis of the Association Between U.S. Mortality and Air Pollution,” *J. Amer. Statistical Association,* vol. 68, p. 342, 1973.

[10] M. H. Ali, J. S. Marks, D. F. Stroup and J. L. Gerberding, “Actual Causes of Death in the United States,” *The Journal of the American Medical Association,* vol. 291, no. 10, pp.

1238-1245, 2000.

[11] J. Schwartz, D. Dockery and L. Neas, “Is daily mortality associated specifically with fine particles?,” *Journal of Air and Waste Management Association,* vol. 46, p. 927–939, 1996.

[12] IPCC Third Assessment Report, “Climate Change 2001: The Scientific Basis”.

[13] V. Ramanathan and G. Carmichael, “Global and regional climate,” *Nature Geoscience,* vol. 1, pp. 221-227, 2008.

[14] NASA, “Soot and Global Warming,” Earth Observatory, 24 December 2003. [Online]. Available: http://earthobservatory.nasa.gov/IOTD/view.php?id=4082.

[15] J. Mc Kenna, Fine Particles (2.5 microns) emissions. Regulations, Measurement and Control, John Wiley & Sons, Inc., 2008.

[16] Integrated Pollution Prevention and Control, “Reference Document on Best Available Techniques in Common Waste Water and Waste Gas Treatment / Management Systems in the Chemical Sector,” http://eippcb.jrc.es/reference/cww.html, 2003.

[17] J. Seinfeld and S. Pandis, Atmospheric Chemistry and Physics, New York: Wiley, 1998.

[18] S. Law, “Embedded-electrode electrostatic induction spray charging nozzle: Theoretical and engineering design,” *Transactions of the ASAE ,* vol. 21, pp. 1096-1104, 1978.

[19] A. Arnold and B. Pye, Spray application with charged rotary atomisers, British Crop Protection Council. 109-117, 1980.

[20] A. Jaworek, W. Balachandran, A. Krupa, J. Kulon and M. Lackowski, Wet electroscrubbers for state of the art gas cleaning, Environmental science and technology 40(20), 6197-6207, 2006.

[21] J. Cross, J. Fowler and G. Fu, “Electrostatic Enhancement of water sprays for coal dust suppression,” Final report to the Health and Safety Trust ISBN 0 7334 2058 3, 2003.

[22] A. Jaworek and A. Krupa, Classification of the modes of EHD apraying, vol. 30, J. Aerosol Sci. Vol. 30, No. 7, pp. 873-893, 1999, pp. 873-893.

[23] I. Hayati, A. I. Bailey and T. F. Tadros, Investigations into the Mechanisms of Electrohydrodynamic Spraying of Liquids, Journal of Colloid and Interface Science, Vol.

117. No. 1, 1987.

[24] O. Lastow and W. Balachandran, Novel low voltage EHD spray nozzle for atomization of water in the cone jet mode, Journal of Electrostatics 65, 490-499, 2007.

[25] S. E. Law, “Agricultural electrostatic spray application: a review of signi"cant research and development during the 20th century,” *Journal of Electrostatics,* Vols. 51-52, pp. 25-42, 2001.

[26] R. S. Miller, K. Harstad and J. Bellan, “Evaluation of equilibrium and non-equilibrium evaporation models for many-droplet gas-liquid ¯ow simulations,” *International Journal of Multiphase Flow,* vol. 24, pp. 1025-1055, 1998.

[27] G. A. E. Godsave, “Studies of the combustion of drops in a fuel spray: the burning of single drops of fuel,” in *Proceeding of the Fourth Symposium (International) on combustion*, 1953.

[28] D. B. Spalding, “The combustion of liquid fuels,” in *Proceeding of the Fourth Symposium (International) of Combustion*, 1953.

[29] G. L. Hubbard, V. E. Denny and A. F. Mills, “Droplet evaporation: effects of transients and variable properties,” *Int. J. Heat Mass Transfer,* vol. 18, pp. 1003-1008, 1973.

[30] S. K. Aggarwal, A. Y. Tong and W. A. Sirignano, “A Comparison of Vaporization Models in Spray Calculations,” *AIAA JOURNA,* vol. 22, no. 10, pp. 1448-1457, 1984.

[31] R. L. Grimm and J. L. Beauchamp, “Evaporation and Discharge Dynamics of Highly Charged Multicomponent Droplets Generated by Electrospray Ionization,” *J. Phys. Chem.,* vol. 114, pp. 1411-1419, 2010.

[32] A. K. Kamra, R. V. Bhalwankar and A. B. Sathe, “Spontaneous breakup of charged and uncharged water drops freely suspended in a wind tunnel,” *J. Geophys. Res.,* vol. 96, no. 17, pp. 159-168, 1991.

[33] C. C. Chuang and K. V. Beard, “A numerical model for the equilibrium shape of electrified raindrops,” *J. Atmos. Sci.,* vol. 47, no. 1374-1389, 1990.

[34] R. V. Bhalwankar, A. B. Sathe and A. K. Kamra, “The evaporation of the charged and uncharged water drops suspended in a wind tunnel,” *Proc. Indian Acad. Sci.,* vol. 113, no. 2, pp. 129-138, 2004.

[35] W. C. Hinds, Aerosol Technology: Properties, Behavior, and Measurement of Airborne Particles, John Wiley & Sons, Inc.: New York, 1999.

[36] B. Y. H. Liu and H. C. Yeh, On the Theory of Charging of Aerosol Particles in an Electric Field., 1968.

[37] B. Y. H. Liu and A. Kapaddia, Combined Field and Diffusion Charging of Aerosol Particles in the Continuum Regime, J. Aerosol Sci., 9, 227-242, 1978.

[38] P. A. Lawless, Particle Charging Bounds, Symmetry Relations,and an Analytic Charging RateModelfor theContinuumRegime, J. Aerosol Sci., 9, 191-215, 1996.

[39] B. Benamer, E. Favre, A. Donnot and M. O. Rigo, "Finite Element Solution for Ionized Fields in DC Electrostatic Precipitator," in *Excerpt from the Proceedings of the COMSOL Users Conference*, Grenoble, 2007.

[40] M. Venugopalan, Reaction under plasma condition, 1971.

[41] O. V. Kim and P. F. Dunn, "Real-Time Direct Charge Measurements of Microdroplets and Comparison with Indirect Methods," *Aerosol Science and Technology,* vol. 44, pp. 292-301, 2010.

[42] R. D. Morrison, "The distribution of current in wire-to-cylinder corona," *Journal of Electrostatics,* vol. 6, pp. 349-360, 1979.

[43] A. D. Chistyakov, "The Permittivity of Water and Water Vapor in Saturation States," *Russian Journal of Physical Chemistry A.,* vol. 81, no. 1, pp. 11-14, 2007.

[44] H. J. White, Industrial Electrostatic Precipitation, Addison-Wesley, 1963.

[45] P. Saiyasitpanich, T. C. Kenner, M. Lu, S.-J. Khang and D. E. Evans, "Cylindrical Single-Stage Wet Electrostatic Precipitators," *Environ. Sci. Technol.,* vol. 40, pp. 7890-7895, 2006.

[46] W. Licht, Air Pollution Control Engineering: Basic Calculations for Particulate Collection, 2nd ed., Marcel Dekker: New York, 1988.

[47] W. Slinn, Precipitation scavenging. In: Atmospheric Sciences and Power Production (Chap 11), U.S. Dept. of Energy: Division of Biomed. Env. Res., 1983.

[48] H. Kim, C. Jung, S. Oh and K. Lee, Particle Removal Efficiency of Gravitational Wet Scrubber Considering Diffusion, Interception, and Impaction, Env. Eng. Sci., 18(2) 125,

2001.

[49] C. Jung and K. Lee, Filtration of fine particles by multiple liquid droplet and gas bubble systems, Aerosol Science & Technology, 29, 389, 1998.

[50] H. Davenport and L. Peters, Field studies of atmospheric particulate concentration changes during precipitation, Atmospheric Environment, 12, 997, 1978.

[51] K. A. Nielsen and J. C. Hill, "Capture of Particles on Spheres by Inertial and Electrical Forces," *Ind. Eng. Chem., Fundam.,* vol. 15, no. 3, pp. 157-163, 1976.

[52] K. Nielsen and J. Hill, "Collection of inertialess particles on spheres with electrical forces," *Ind. Eng. Chem., Fundam.,* vol. 15, no. 3, pp. 149-156, 1976.

[53] S. Grover, H. Pruppacher and A. Hamielec, "A numerical determination of the efficiency with which spherical aerosol particles collide with spherical water drops due to inertial impaction and phoretic and electric forces," *Journal of the Atmospheric Sciences,* vol. 34, p. 1655, 1977.

[54] H. Kraemer and H. Johnstone, "Collection of aerosol particles in presence of electrostatic fields," *Ind. Eng. Chem. ,* vol. 47, pp. 2426-2434, 1955.

[55] A. K. Barlow and J. Latham, "A laboratory study of the scavenging of sub-micron aerosol by charged raindrops," *Quart. J. R. Met. Soc.,* vol. 109, pp. 763-770, 1983.

[56] G. W. Penney.U.S. Patent Patent 2,357,354, 1944.

[57] M. J. Pilat, S. A. Jaasund and L. E. Sparks, "Collection of Aerosol Particles by Electrostatic Droplet Spray Scrubbers," *Environmental Science,* vol. 8, 1974.

[58] P. Metzler, P. Weiß, H. Büttne and F. Ebert, "Electrostatic enhancement of dust separation in a nozzle scrubber," *Journal of Electrostatics,* vol. 42, no. 1-2, pp. 123-129, 1997.

[59] A. Krupa, A. Jaworek, T. Czech, M. Lackowski and J. Luckner, "Dust Particles Removal by Wet-type Electrostatic Scrubber," in *11th Conf. ELECTROSTATICS*, Edinburgh, 2003.

[60] W. Balachandran, A. Jaworek, A. Krupa, J. Kulon and M. Lackowski, "Efficiency of smoke removal by charged water droplets," *Journal of Electrostatics,* no. 58, pp. 209-220, 2003.

[61] A. Jaworek, W. Balachandran, M. Lackowski, J. Kulon and A. Krupa, "Multi-nozzle electrospray system for gas cleaning processes," *Journal of Electrostatics,* no. 64, p. 194–

202, 2006.

[62] T. H. Ha, O. Nishida and H. Fujita, “Enhancement of diesel particulate matter collection in an electrostatic water-spraying scrubber,” *J. Mar. Sci. Technol.,* vol. 15, p. 271–279, 2010.

[63] H. Wang, J. Stukel and K. Long, “Particle deposition on spheres by inertial and electrostatic forces,” *Aerosol Sic. Technology,* vol. 5, no. 4, pp. 391-408, 1986.

[64] K. Adamiak, A. Jaworek and A. Krupa, “Deposition Efficiency of Dust Particles on a Single, Falling and Charged Water Droplet,” *IEEE TRANSACTIONS ON INDUSTRY APPLICATIONS,* vol. 38, no. 3, 2001.

[65] A. Jaworek, K. Adamiak and A. Krupa, “Deposition of aerosol particles on a charged spherical collector,” *J. Electrostatics,* Vols. 40-41, pp. 443-448, 1997.

[66] H. Zhao and C. Zheng, “Modeling of Gravitational Wet Scrubbers with Electrostatic Enhancement,” *Chem. Eng. Technol.,* vol. 31, no. 12, pp. 1824-1837, 2008.

[67] C. Carotenuto, F. Di Natale and A. Lancia, “Wet Electrostatic Scrubbers for the Abatment of Submicronic Particulate,” *Chemical Engineering Journal,* vol. 165, pp. 35-45, 2010.

[68] A. Jaworek and A. Krupa, “Classification of the modes of EHD apraying,” vol. 30, no. 7, pp. 873-893, 1999.

[69] Z. Huneiti and W. Balachandran, “Effects of conducting liquid jet disintegration on specific charge of spray,” *Journal of Electrostatics,* no. 51-52, pp. 558-564, 2001.

[70] O. Lastow and W. Balachandran, “Novel low voltage EHD spray nozzle for atomization of water in the cone jet mode,” vol. 65, pp. 490-499, 2007.

[71] Y. Zhuang, J. Y. Kim, G. T. Lee and P. Biswas, “Experimental and theoretical studies of ultra-fine particle behavior in electrostatic precipitators,” *Journal of Electrostatics,* no. 48, pp. 245-260, 2000.

[72] Cloupeau, M. Cloupeau and B. Prunet-Foch, “ELECTROSTATIC SPRAYING OF LIQUIDS IN CONE-JET MODE,” *Journal of Electrostatics,* vol. 22, pp. 135-159, 1989.

[73] S. H. Park, C. H. Jung, K. R. Jung, B. K. Lee and K. W. Lee, “Wet scrubbing of polydisperse aerosols by freely falling droplets,” *Aerosol Science,* vol. 36, pp. 1444-1458, 2005.

[74] B. T. Mc Gann and S. C. Jennings, “The efficincy with which drizzle and precipitation sized drops collide with aerosol particles,” *Atmos. Environ.,* vol. 25A, pp. 791-799, 1991.

[75] M. A. Byrne and S. C. Jennings, “Scavenging of sub-micromiter aerosol particles by water drops,” *Atmos. Environ,* vol. 27A, pp. 2099-2105, 1993.

[76] T. S. Pranesha and A. K. Kamra, “Scavenging of aerosol particles by large water drops. Washout coefficient, half-lives, and rainfall depths,” *J. Geophy. Res.,* vol. 102, 1997.

[77] B. A. Tinsley, “Effects of image charges on scavenging of aerosol particles by cloud droplets and on droplet chargng and posible ice nucleation process,” *J. Atmos. Sci.,* vol. 57, pp. 2118-2134, 2000.

Appendix - Particle abatement Data

In this appendix the results on particle abatement are provided. For each test a report sheet is reported; it contains the experimental and theoretical scavenging coefficients, the theoretical collision efficiency and the distribution measured during the scrubbing time for the electrospray exerted in the conditions reported in the following table.

Report N°	$t_r \cdot N_i$ [s/m^3]	V_E [kV]	Q_w [mL/min]	U_d [m/s]	τ_r [s]	q [pC]	D [mm]	$D\text{-}CMR$ [mC/kg]	q/q_R [-]	N [#/m^3]
1	8.1E+12	3.7	1.87	0.944	0.211	79.4	0.90	0.208	0.41	11007
2	1.1E+13	3.7	1.87	0.944	0.211	79.4	0.90	0.208	0.41	10830
3	9.9E+12	3.5	1.87	0.951	0.210	83.7	1.00	0.160	0.36	7968
4	1.0E+13	3.5	1.87	0.951	0.210	83.7	1.00	0.160	0.36	8522
5	1.0E+13	3.5	1.84	0.951	0.210	83.7	1.00	0.16	0.36	7968
6	1.0E+13	4.0	1.60	0.944	0.211	100.8	0.90	0.265	0.52	9417
7	1.1E+13	4.0	1.60	0.944	0.211	100.8	0.90	0.265	0.52	9417
8	9.7E+12	3.0	1.87	0.956	0.209	126.1	1.10	0.181	0.48	5954
9	9.9E+12	3.0	1.87	0.956	0.209	126.1	1.10	0.181	0.48	5954
10	1.0E+13	2.8	1.87	0.964	0.207	154.8	1.30	0.135	0.45	3579
11	1.1E+13	3.0	1.84	0.944	0.211	80.0	0.90	0.208	0.41	11010
12	1.2E+13	2.5	2.00	0.969	0.206	127.3	1.70	0.064	0.30	2479
13	1.2E+13	3.5	1.87	0.940	0.213	107.0	0.95	0.237	0.50	9323
14	1.3E+13	3.5	1.87	0.940	0.213	107.0	0.95	0.237	0.50	9323
15	1.3E+13	3.0	1.87	0.940	0.213	96.7	1.07	0.137	0.38	6488
16	1.2E+13	3.0	1.87	0.955	0.209	96.7	1.07	0.137	0.38	6488

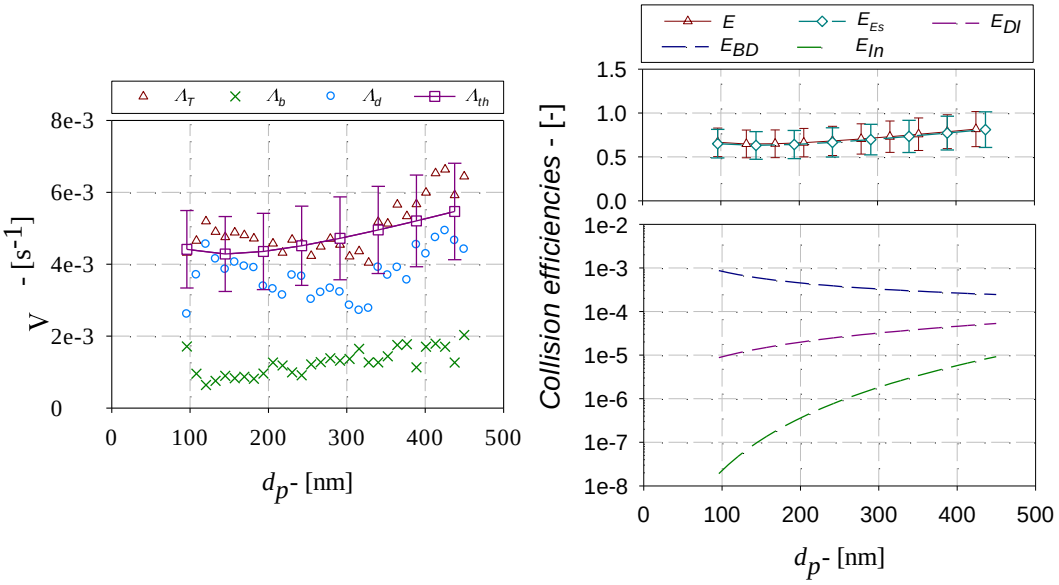
Λ_T
Λ_b
Λ_d
Λ_{th}
8e-3
6e-3
4e-3
2e-3
0
V - [s^{-1}]
0
100
200
300
400
500
d_p - [nm]
E
E_{Es}
E_{Dl}
E_{BD}
E_{In}
1.5
1.0
0.5
0.0
1e-2
1e-3
1e-4
1e-5
1e-6
1e-7
1e-8
Collision efficiencies - [-]
0
100
200
300
400
500
d_p - [nm]

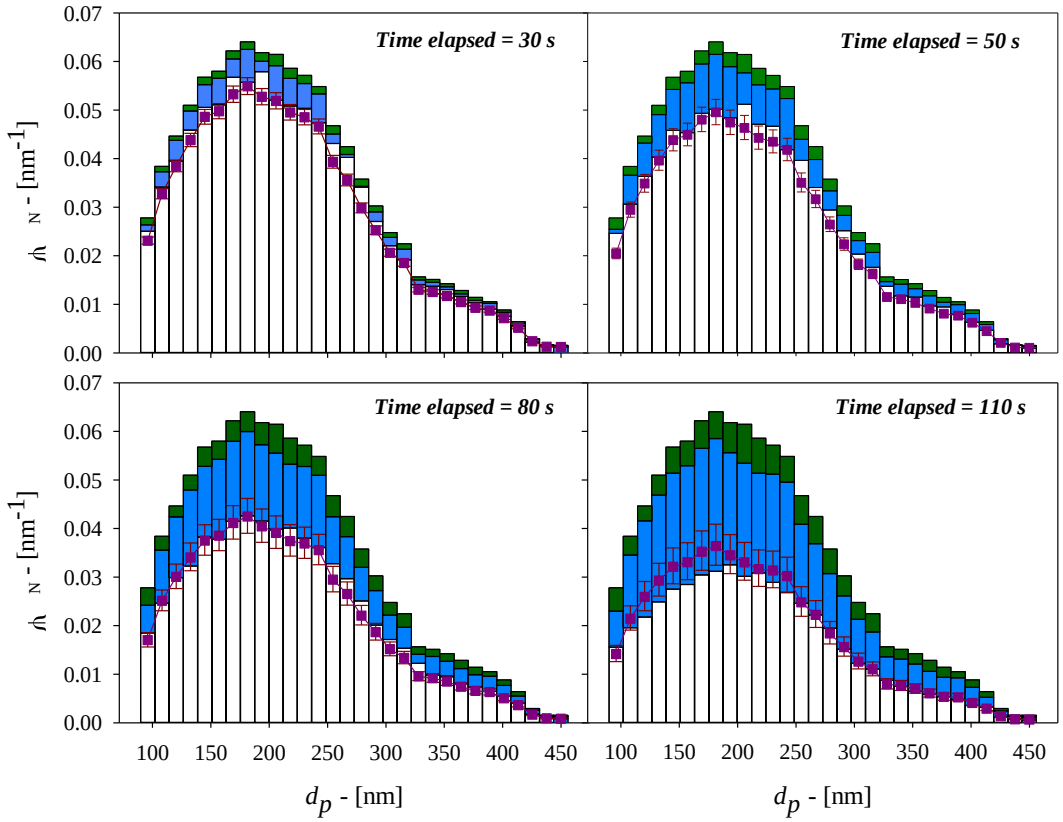
Time elapsed = 30 s
Time elapsed = 50 s
Time elapsed = 80 s
Time elapsed = 110 s
0.07
0.06
0.05
0.04
0.03
0.02
0.01
0.00
$\dot{n}_N$ - [nm^{-1}]
100
150
200
250
300
350
400
450
d_p - [nm]

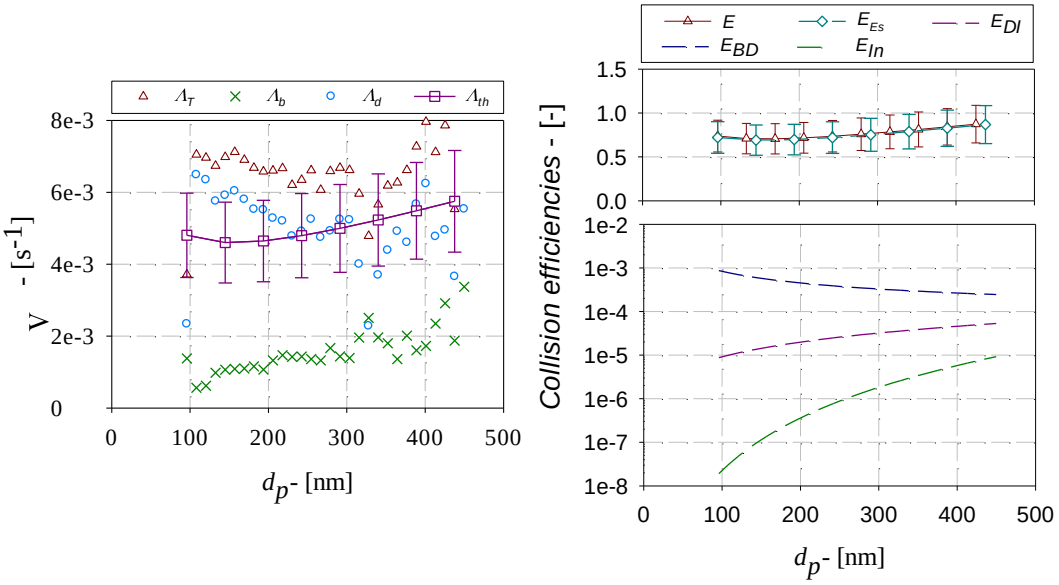
Λ_T
Λ_b
Λ_d
Λ_{th}
8e-3
6e-3
4e-3
2e-3
0
V - [s^{-1}]
0
100
200
300
400
500
d_p - [nm]
E
E_{Es}
E_{DI}
E_{BD}
E_{In}
1.5
1.0
0.5
0.0
1e-2
1e-3
1e-4
1e-5
1e-6
1e-7
1e-8
Collision efficiencies - [-]
0
100
200
300
400
500
d_p - [nm]

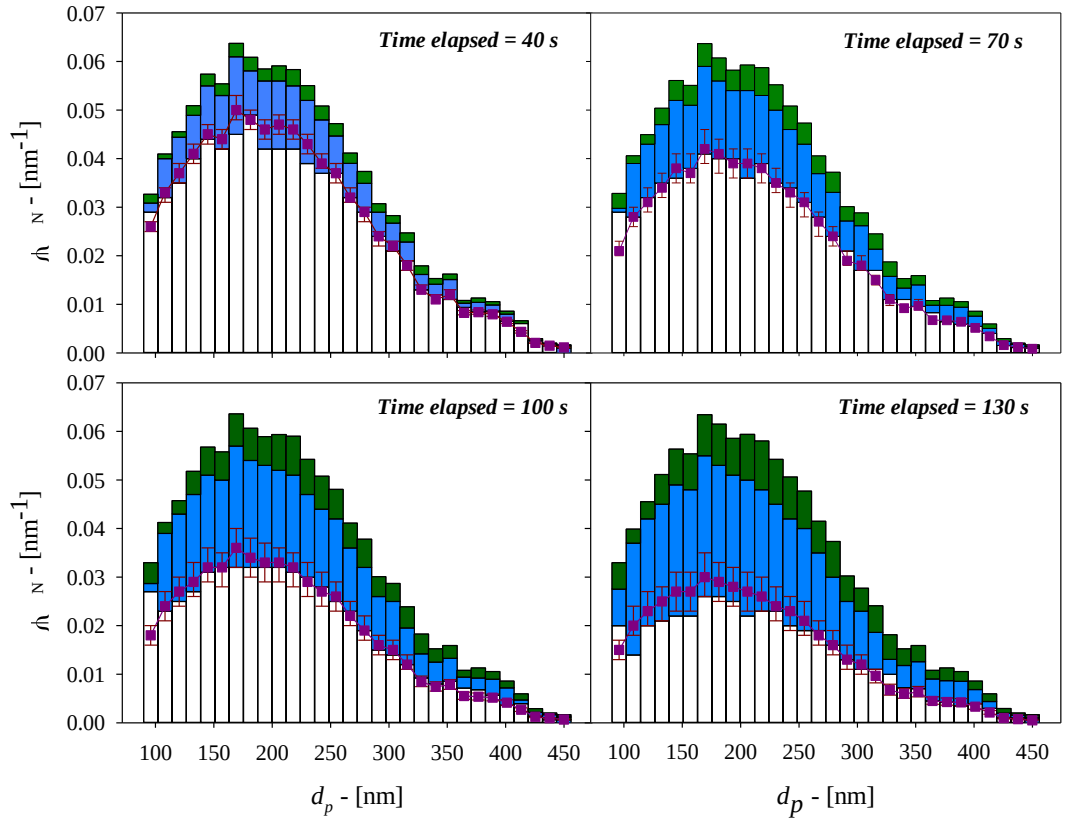
Time elapsed = 40 s
Time elapsed = 70 s
Time elapsed = 100 s
Time elapsed = 130 s
0.07
0.06
0.05
0.04
0.03
0.02
0.01
0.00
$\dot{n}_N$ - [nm^{-1}]
100
150
200
250
300
350
400
450
d_p - [nm]

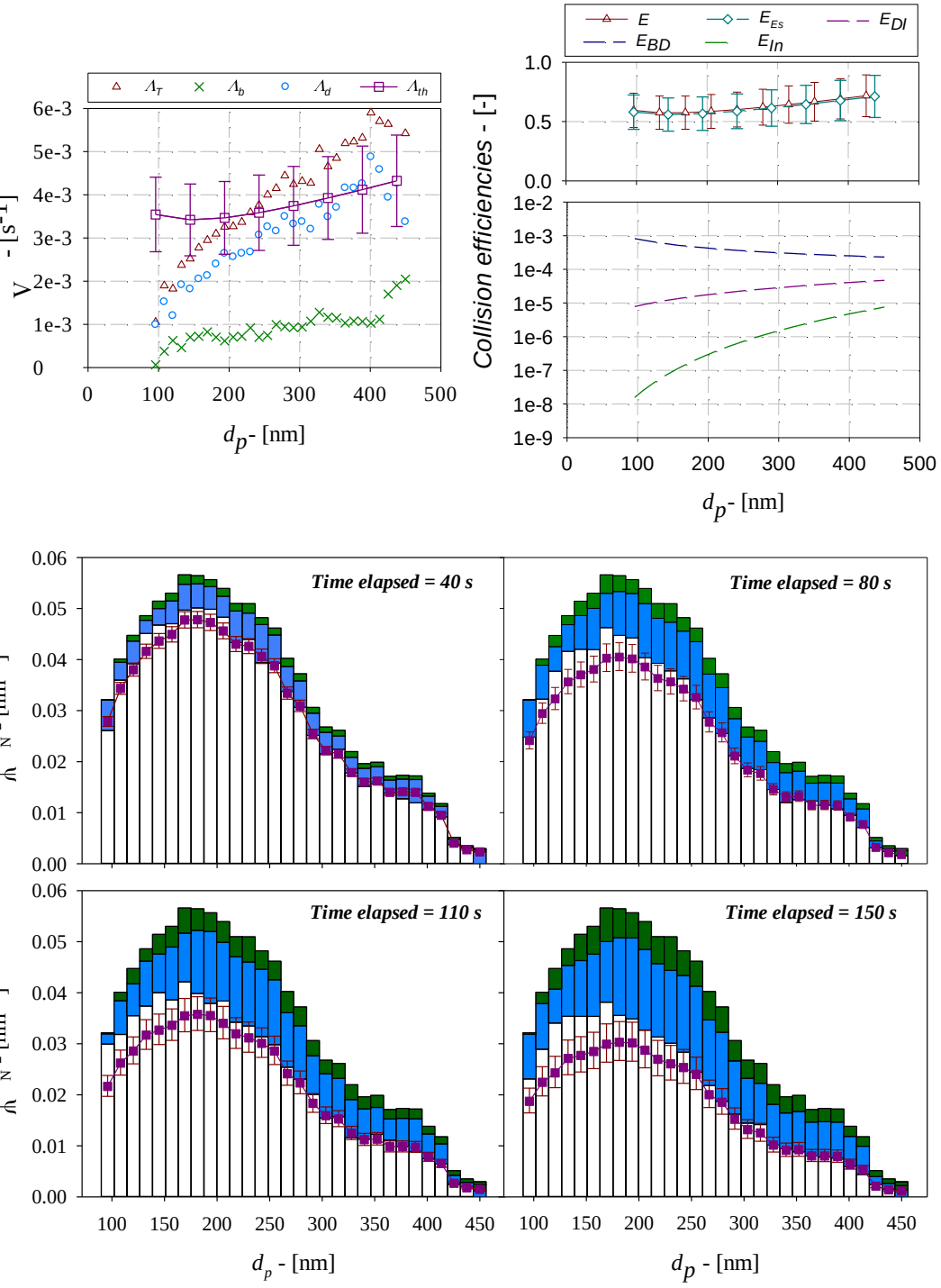
Λ_T
Λ_b
Λ_d
Λ_th
- [s-1]
d_p - [nm]
E
E_Es
E_DI
E_BD
E_In
Collision efficiencies - [-]
Time elapsed = 40 s
Time elapsed = 80 s
Time elapsed = 110 s
Time elapsed = 150 s
n_N - [nm-1]
d_p - [nm]

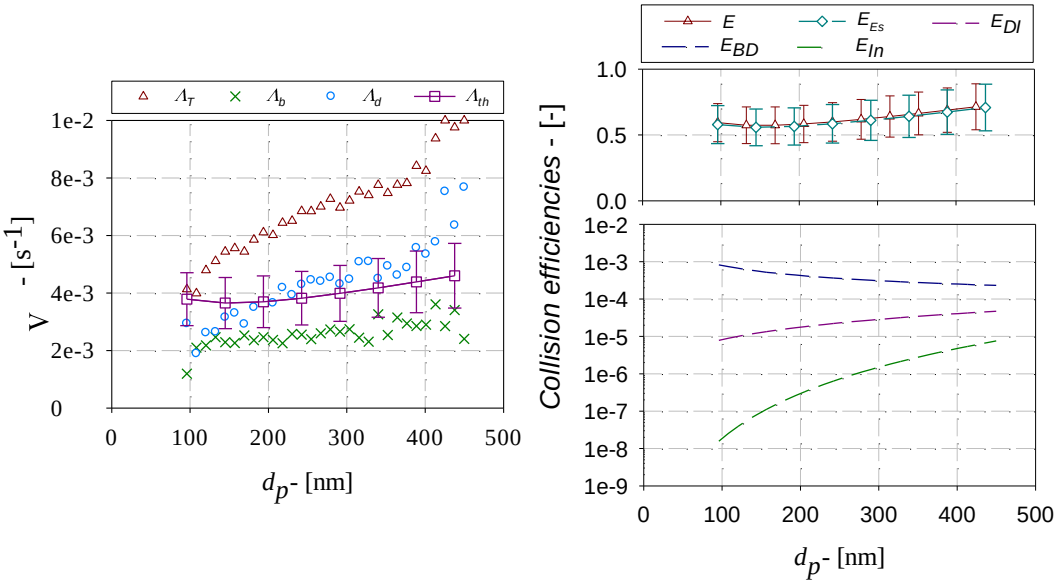
Λ_T
Λ_b
Λ_d
Λ_th
1e-2
8e-3
6e-3
4e-3
2e-3
0
V - [s-1]
0
100
200
300
400
500
dp- [nm]
E
E_Es
E_DI
E_BD
E_In
1.0
0.5
0.0
Collision efficiencies - [-]
1e-2
1e-3
1e-4
1e-5
1e-6
1e-7
1e-8
1e-9
0
100
200
300
400
500
dp- [nm]

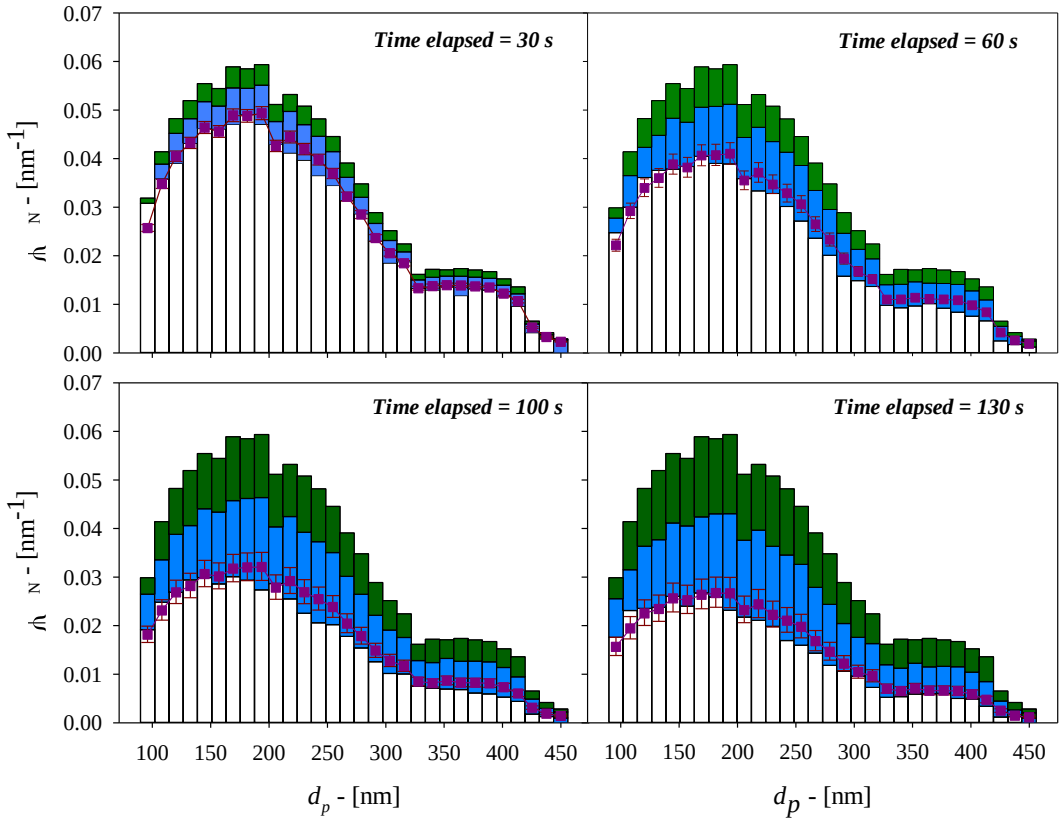
Time elapsed = 30 s
Time elapsed = 60 s
Time elapsed = 100 s
Time elapsed = 130 s
0.07
0.06
0.05
0.04
0.03
0.02
0.01
0.00
n N - [nm-1]
100
150
200
250
300
350
400
450
dp - [nm]

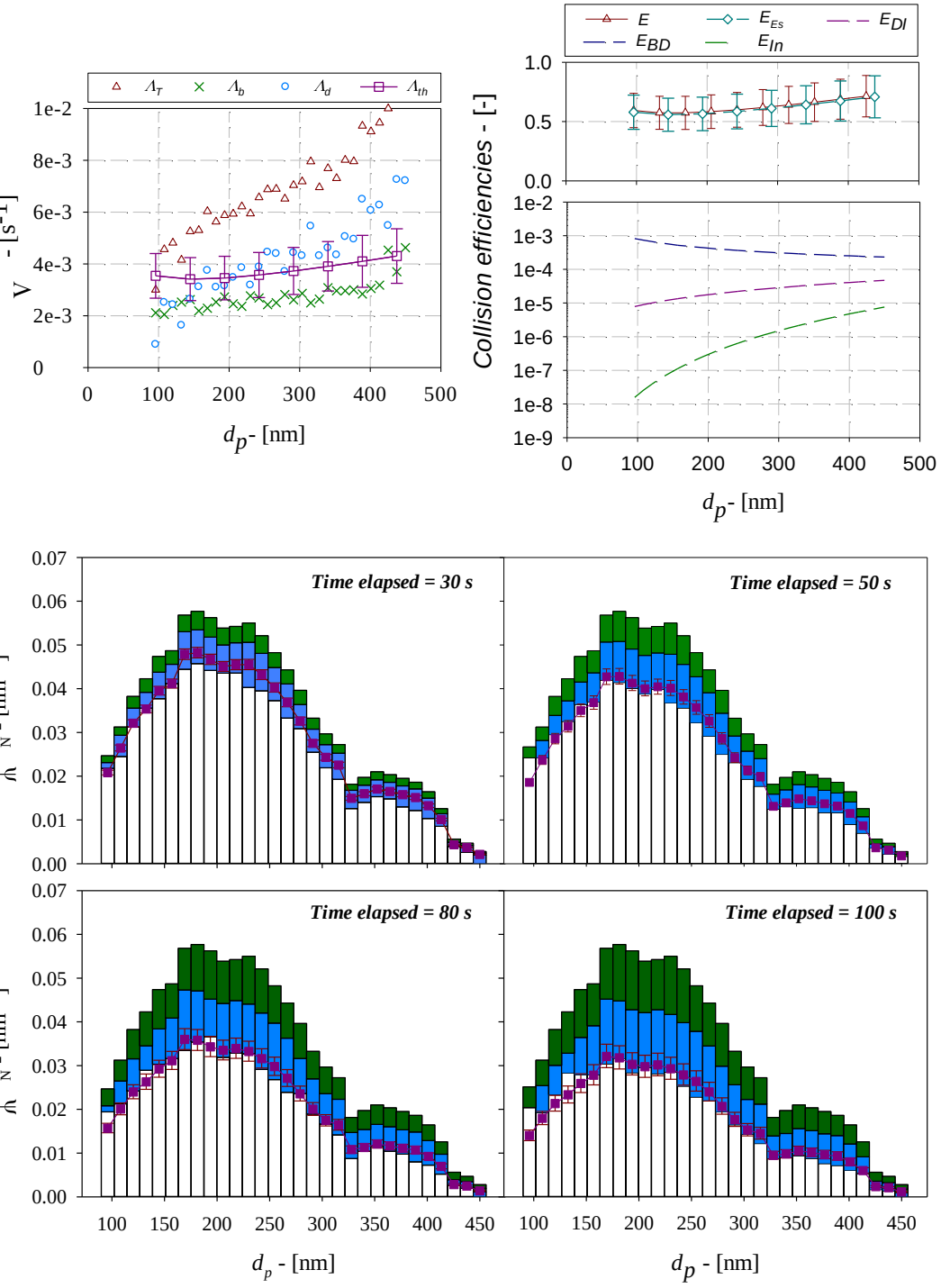
Λ_T
Λ_b
Λ_d
Λ_th
1e-2
8e-3
6e-3
4e-3
2e-3
0
V - [s-1]
0
100
200
300
400
500
dp- [nm]
E
E_Es
E_DI
E_BD
E_In
1.0
0.5
0.0
Collision efficiencies - [-]
1e-2
1e-3
1e-4
1e-5
1e-6
1e-7
1e-8
1e-9
0
100
200
300
400
500
dp- [nm]
Time elapsed = 30 s
Time elapsed = 50 s
Time elapsed = 80 s
Time elapsed = 100 s
0.07
0.06
0.05
0.04
0.03
0.02
0.01
0.00
N - [nm-1]
100
150
200
250
300
350
400
450
dp - [nm]

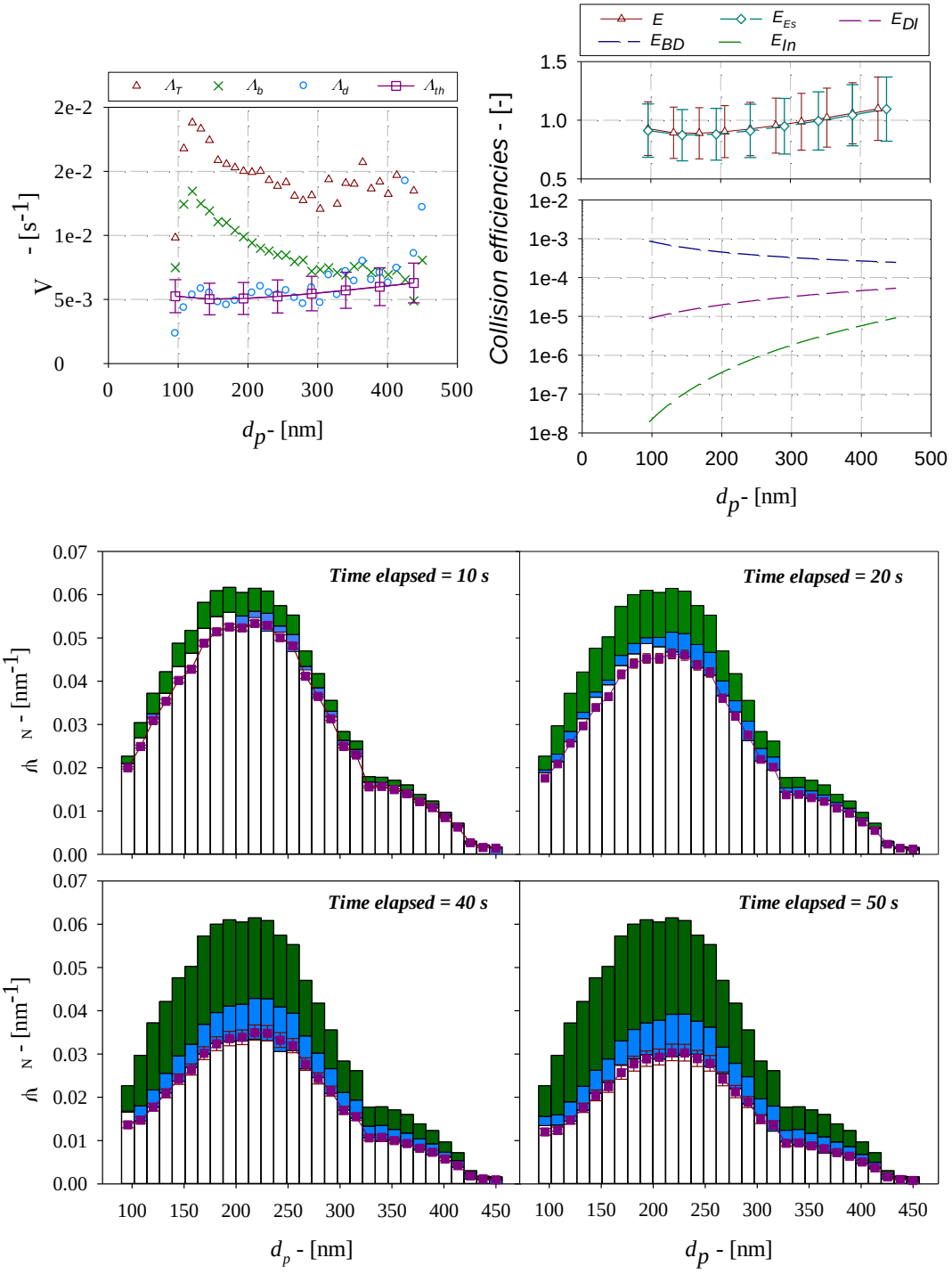
Λ_T
Λ_b
Λ_d
Λ_th
2e-2
2e-2
1e-2
5e-3
0
V - [s-1]
0
100
200
300
400
500
dp- [nm]
E
E_Es
E_Dl
E_BD
E_In
1.5
1.0
0.5
1e-2
1e-3
1e-4
1e-5
1e-6
1e-7
1e-8
Collision efficiencies - [-]
0
100
200
300
400
500
dp- [nm]
Time elapsed = 10 s
Time elapsed = 20 s
Time elapsed = 40 s
Time elapsed = 50 s
0.07
0.06
0.05
0.04
0.03
0.02
0.01
0.00
n N - [nm-1]
100
150
200
250
300
350
400
450
dp - [nm]

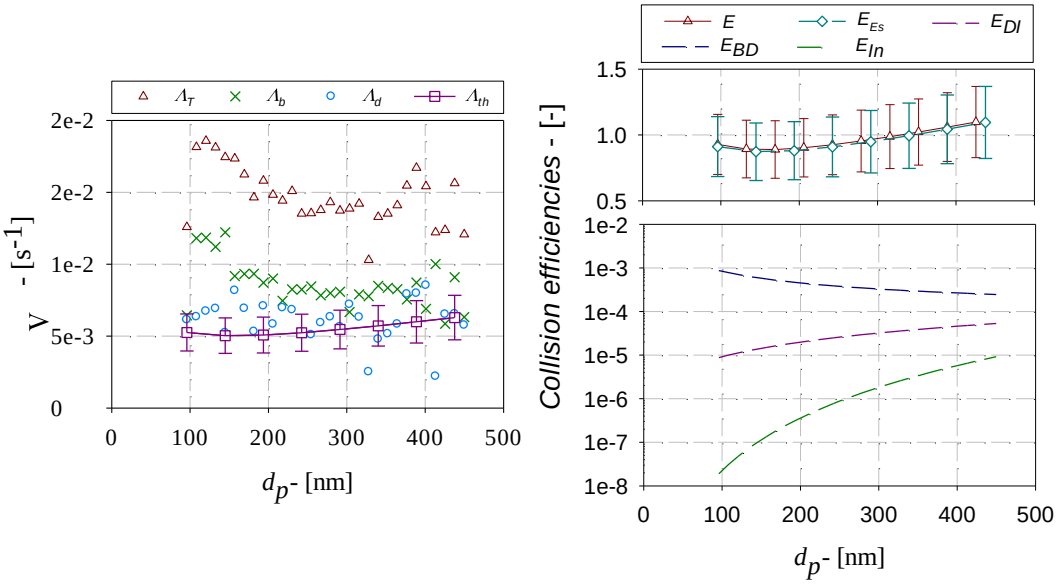
Λ_T
Λ_b
Λ_d
Λ_{th}
2e-2
2e-2
1e-2
5e-3
0
V - [s^{-1}]
0
100
200
300
400
500
d_p- [nm]
E
E_{Es}
E_{DI}
E_{BD}
E_{In}
1.5
1.0
0.5
1e-2
1e-3
1e-4
1e-5
1e-6
1e-7
1e-8
Collision efficiencies - [-]
0
100
200
300
400
500
d_p- [nm]

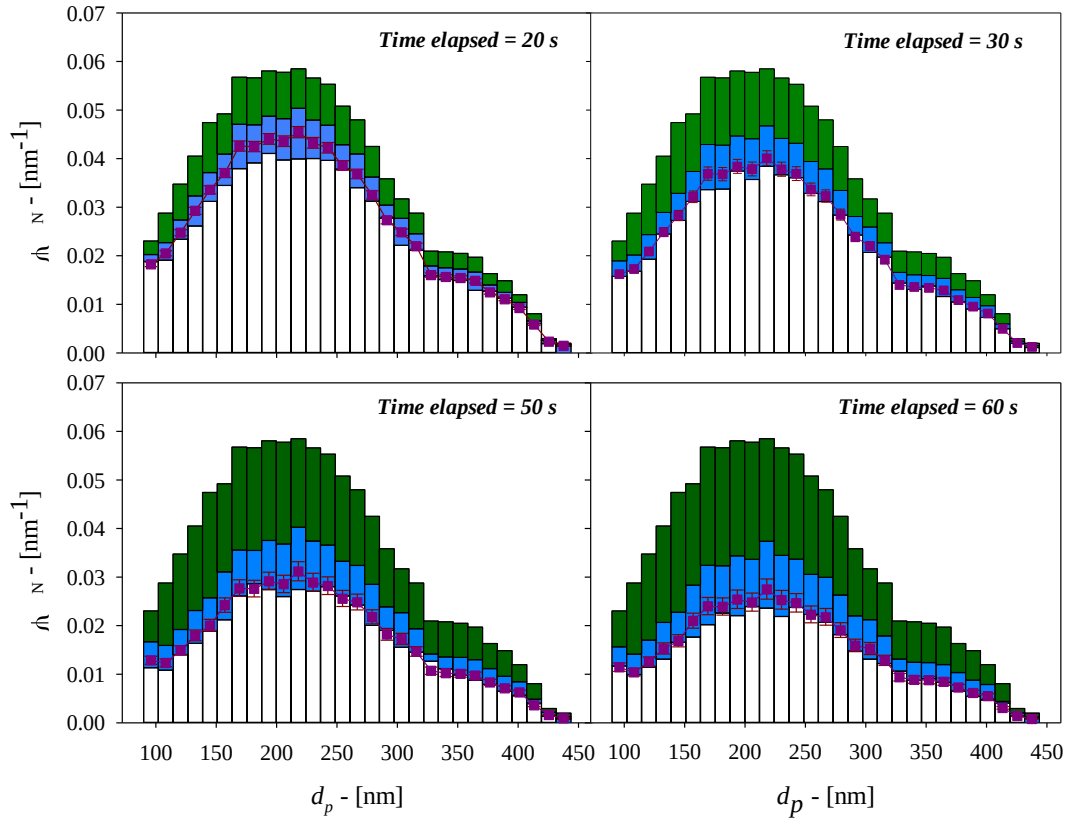
Time elapsed = 20 s
Time elapsed = 30 s
Time elapsed = 50 s
Time elapsed = 60 s
0.07
0.06
0.05
0.04
0.03
0.02
0.01
0.00
$\dot{n}_N$ - [nm^{-1}]
100
150
200
250
300
350
400
450
d_p - [nm]

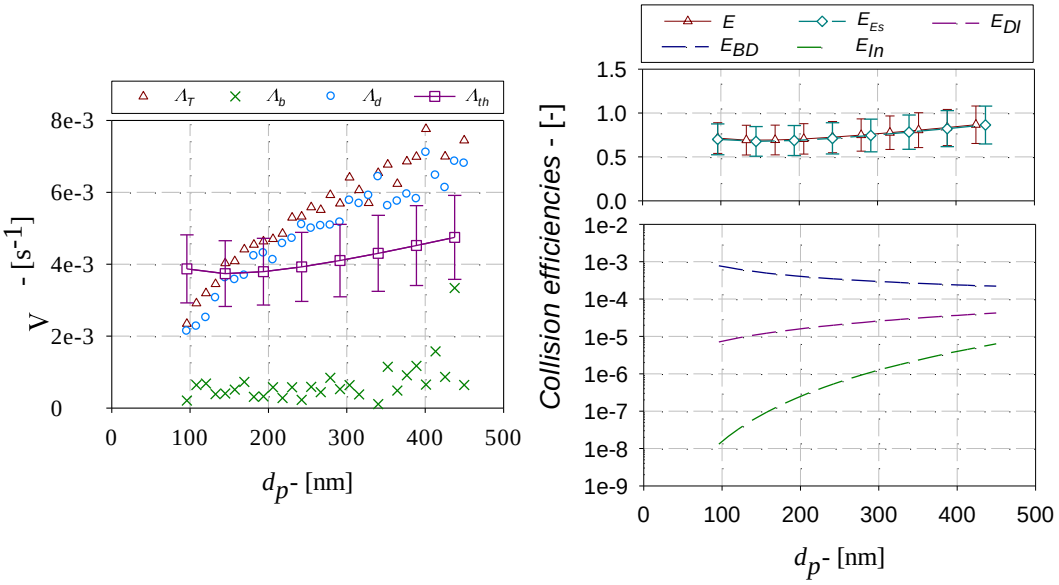
Λ_T
Λ_b
Λ_d
Λ_{th}
V - [s^{-1}]
d_p - [nm]
E
E_{Es}
E_{DI}
E_{BD}
E_{In}
Collision efficiencies - [-]
d_p - [nm]

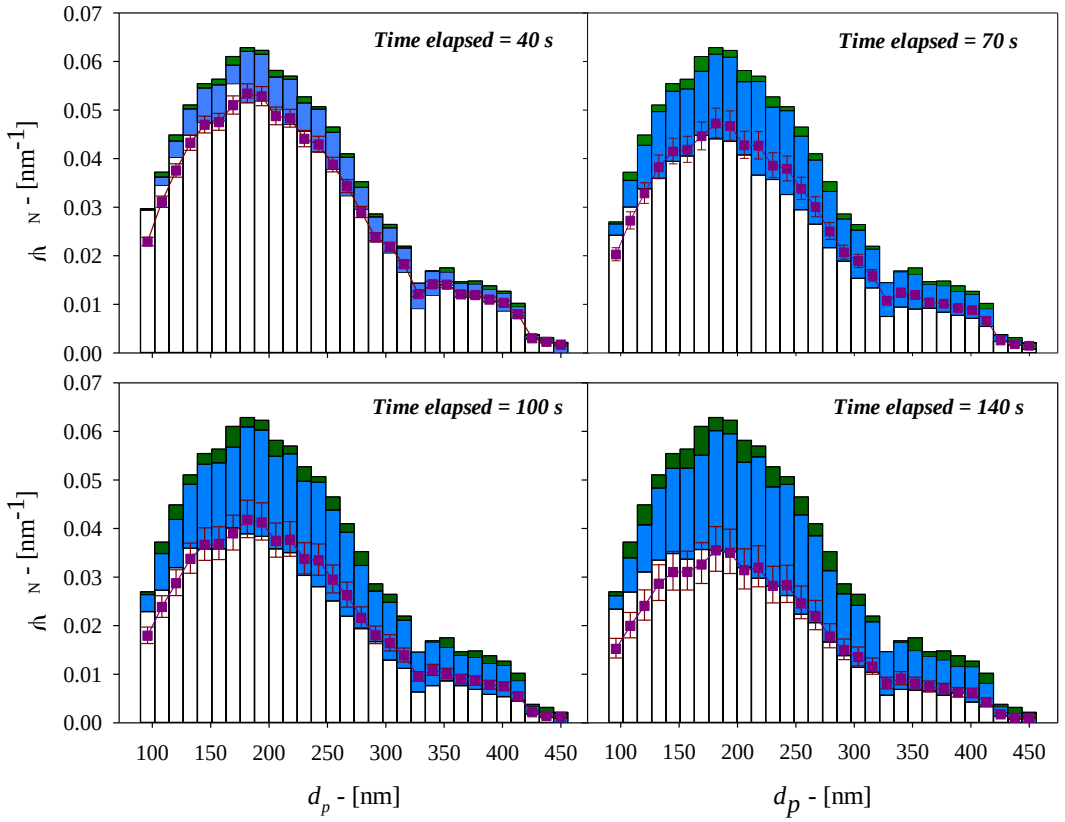
Time elapsed = 40 s
Time elapsed = 70 s
Time elapsed = 100 s
Time elapsed = 140 s
Λ_N - [nm^{-1}]
d_p - [nm]

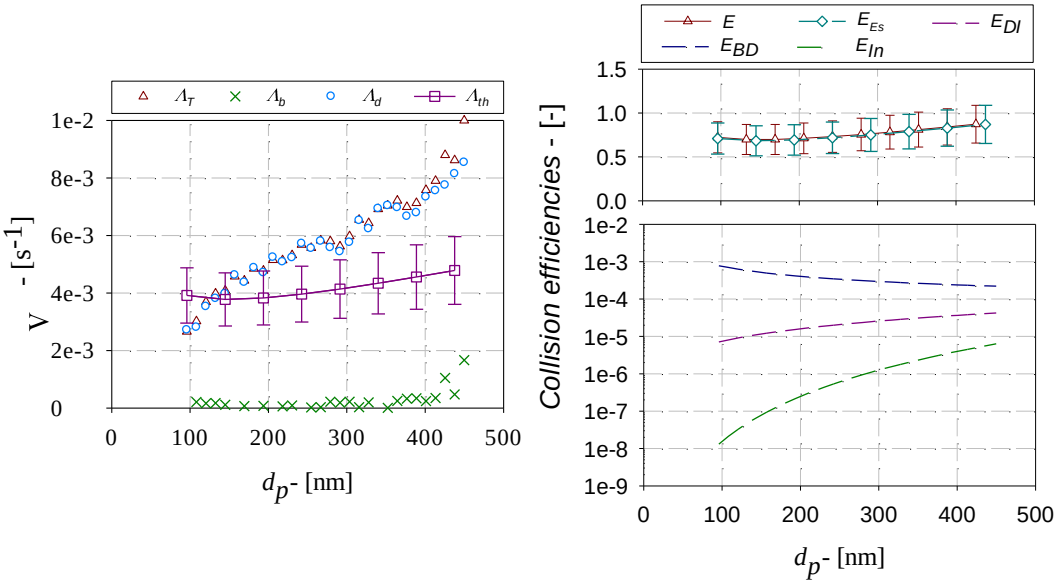
Λ_T Λ_b Λ_d Λ_{th}
1e-2
8e-3
6e-3
4e-3
2e-3
0
V - [s-1]
0 100 200 300 400 500
d_p- [nm]
E E_{Es} E_{DI}
E_{BD} E_{In}
1.5
1.0
0.5
0.0
1e-2
1e-3
1e-4
1e-5
1e-6
1e-7
1e-8
1e-9
Collision efficiencies - [-]
0 100 200 300 400 500
d_p- [nm]

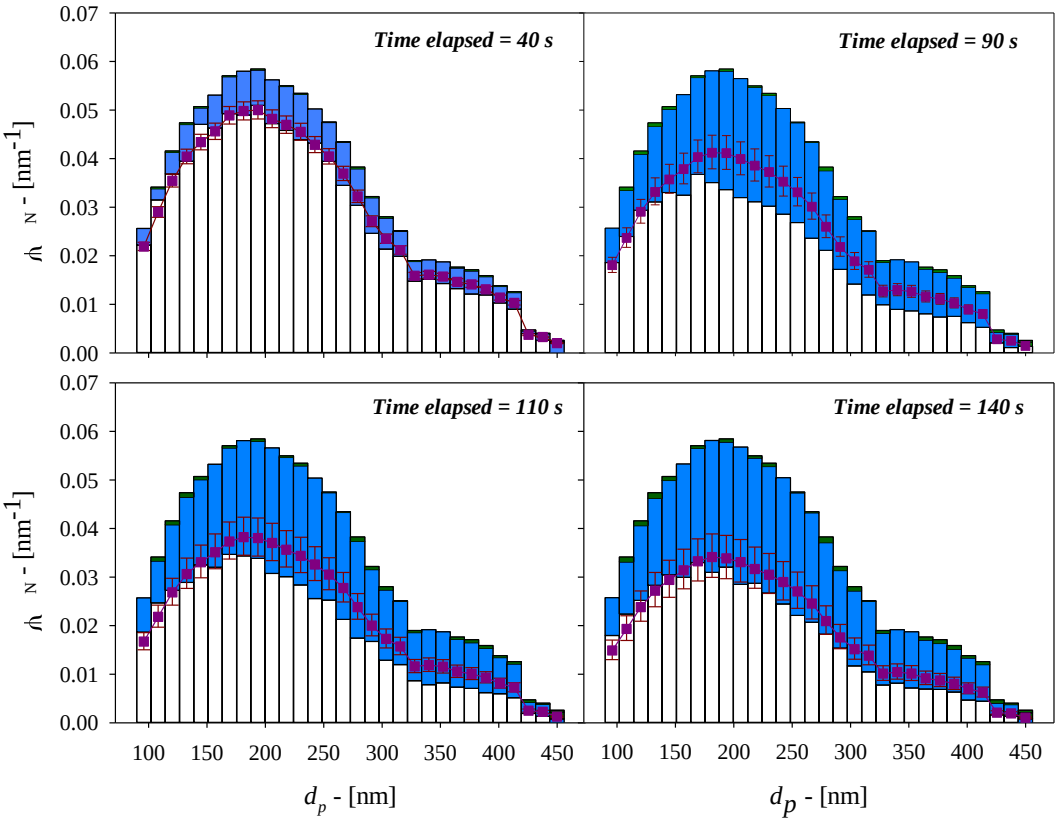
Time elapsed = 40 s
Time elapsed = 90 s
Time elapsed = 110 s
Time elapsed = 140 s
0.07
0.06
0.05
0.04
0.03
0.02
0.01
0.00
ΔN - [nm-1]
100 150 200 250 300 350 400 450
d_p - [nm]

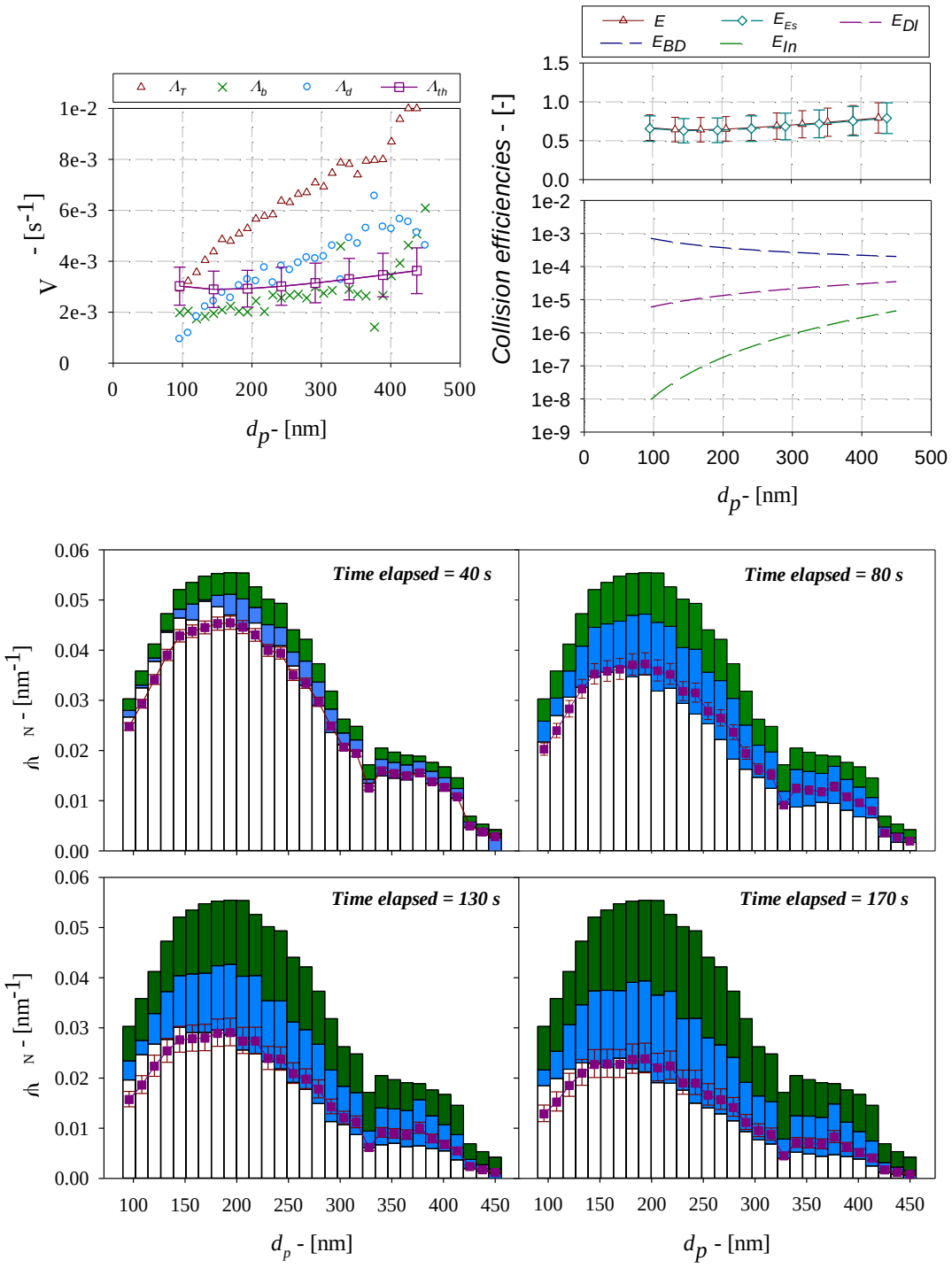
Λ_T
Λ_b
Λ_d
Λ_{th}
V - [s^{-1}]
d_p - [nm]
E
E_{Es}
E_{DI}
E_{BD}
E_{In}
Collision efficiencies - [-]
d_p - [nm]
Time elapsed = 40 s
Time elapsed = 80 s
Time elapsed = 130 s
Time elapsed = 170 s
h_N - [nm^{-1}]
d_p - [nm]

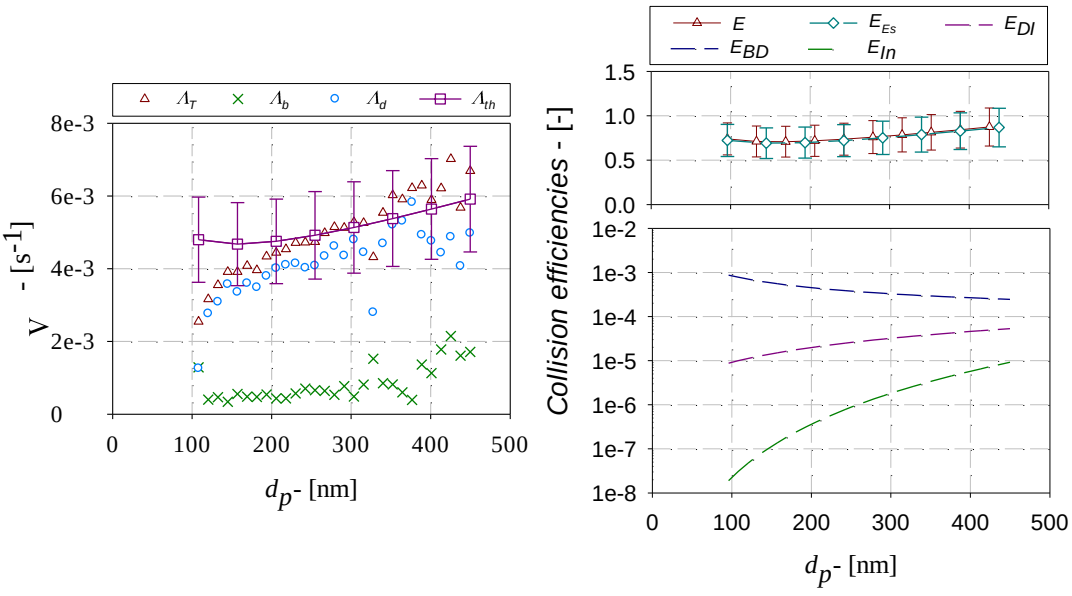
Λ_T Λ_b Λ_d Λ_{th}
8e-3
6e-3
4e-3
2e-3
0
V - [s^{-1}]
0 100 200 300 400 500
d_p- [nm]
E E_{Es} E_{DI}
E_{BD} E_{In}
Collision efficiencies - [-]
1.5
1.0
0.5
0.0
1e-2
1e-3
1e-4
1e-5
1e-6
1e-7
1e-8
0 100 200 300 400 500
d_p- [nm]

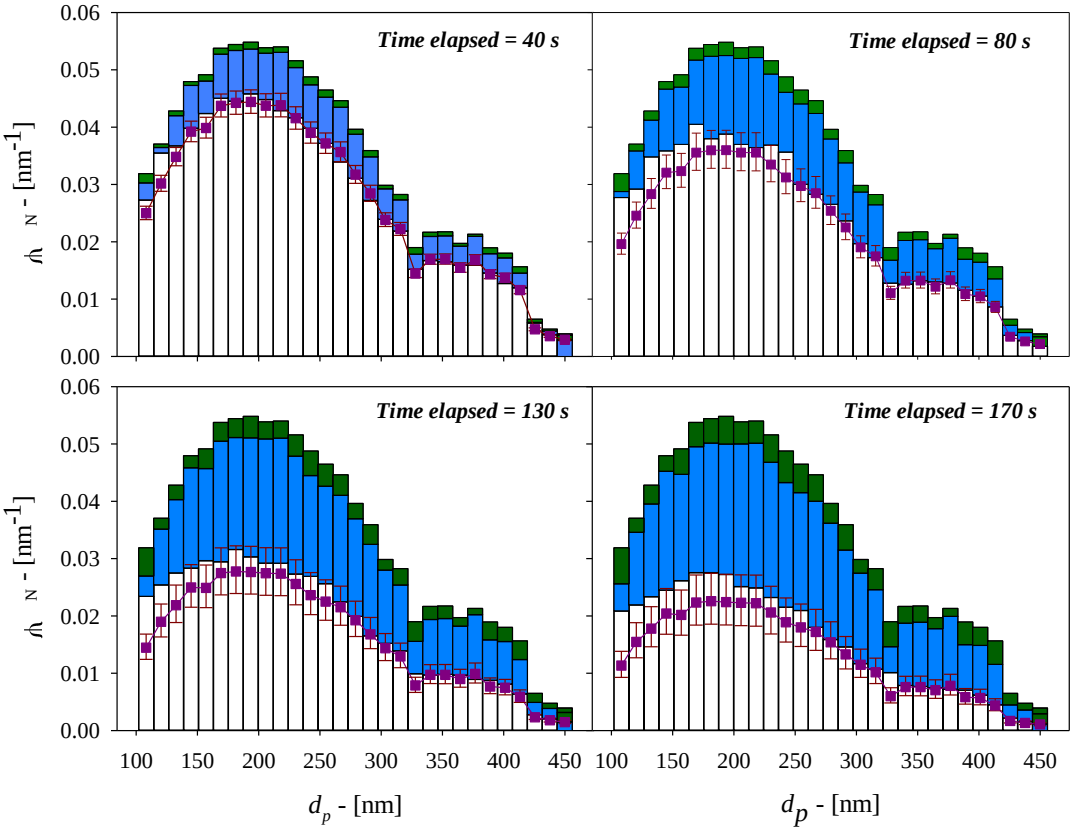
Time elapsed = 40 s
Time elapsed = 80 s
Time elapsed = 130 s
Time elapsed = 170 s
n_N - [nm^{-1}]
0.06
0.05
0.04
0.03
0.02
0.01
0.00
100 150 200 250 300 350 400 450
d_p - [nm]

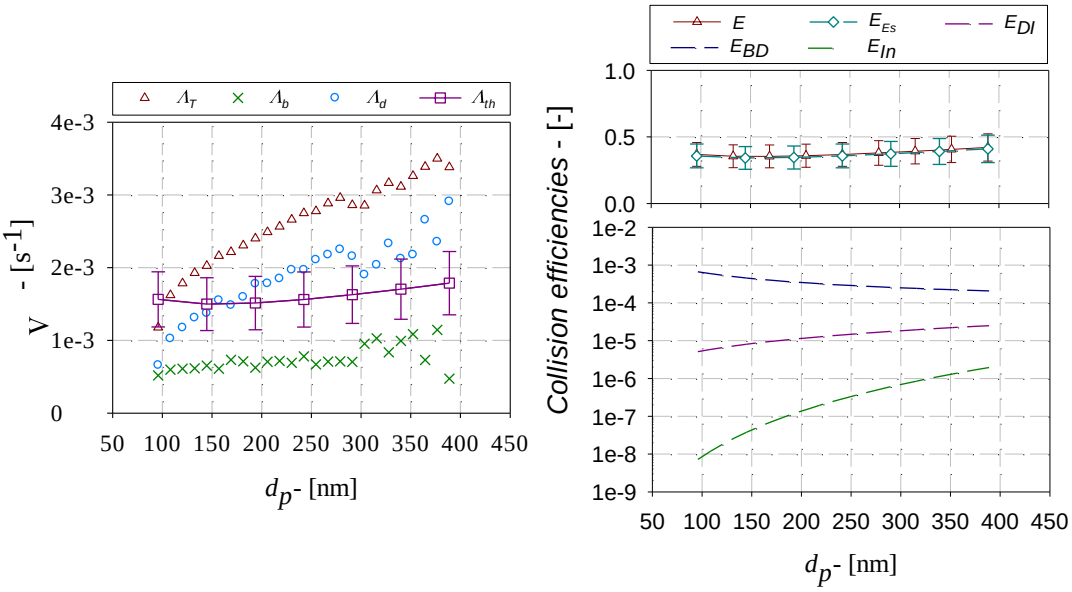
Λ_T
Λ_b
Λ_d
Λ_{th}
4e-3
3e-3
2e-3
1e-3
0
Λ - [s^{-1}]
50 100 150 200 250 300 350 400 450
d_p- [nm]
E
E_{Es}
E_{DI}
E_{BD}
E_{In}
1.0
0.5
0.0
1e-2
1e-3
1e-4
1e-5
1e-6
1e-7
1e-8
1e-9
Collision efficiencies - [-]
50 100 150 200 250 300 350 400 450
d_p- [nm]

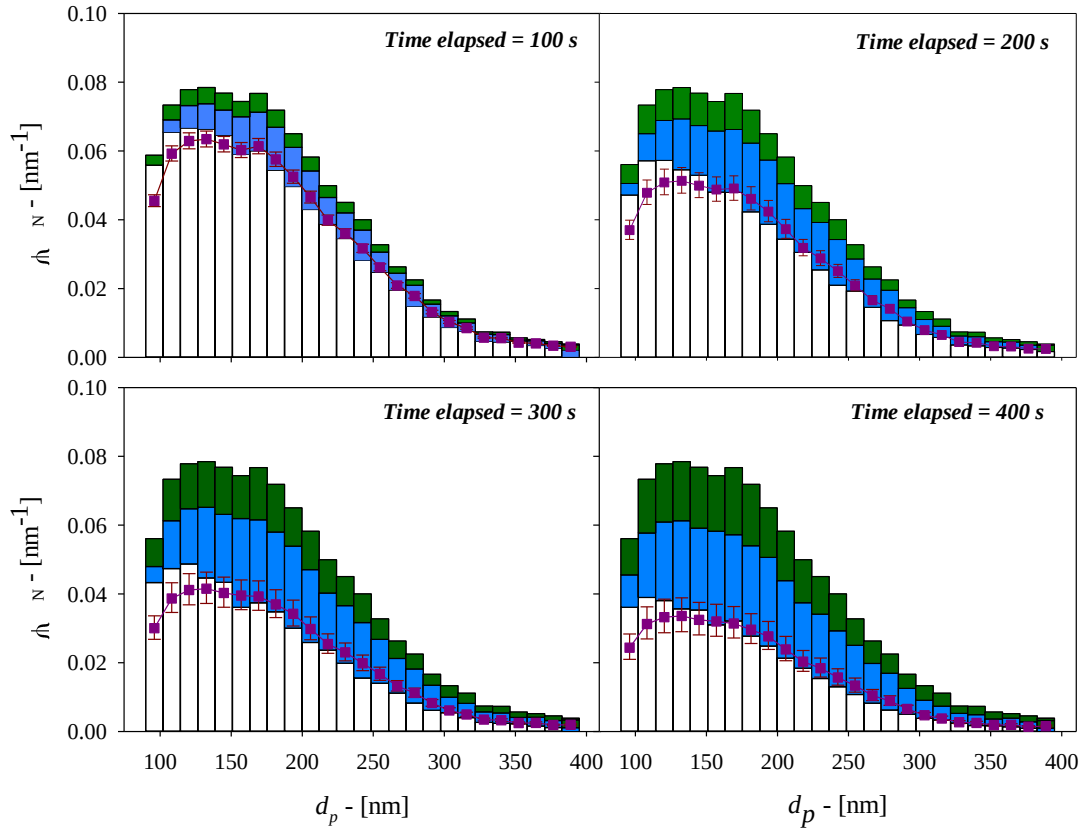
Time elapsed = 100 s
Time elapsed = 200 s
Time elapsed = 300 s
Time elapsed = 400 s
0.10
0.08
0.06
0.04
0.02
0.00
ΔN - [nm^{-1}]
100 150 200 250 300 350 400
d_p - [nm]

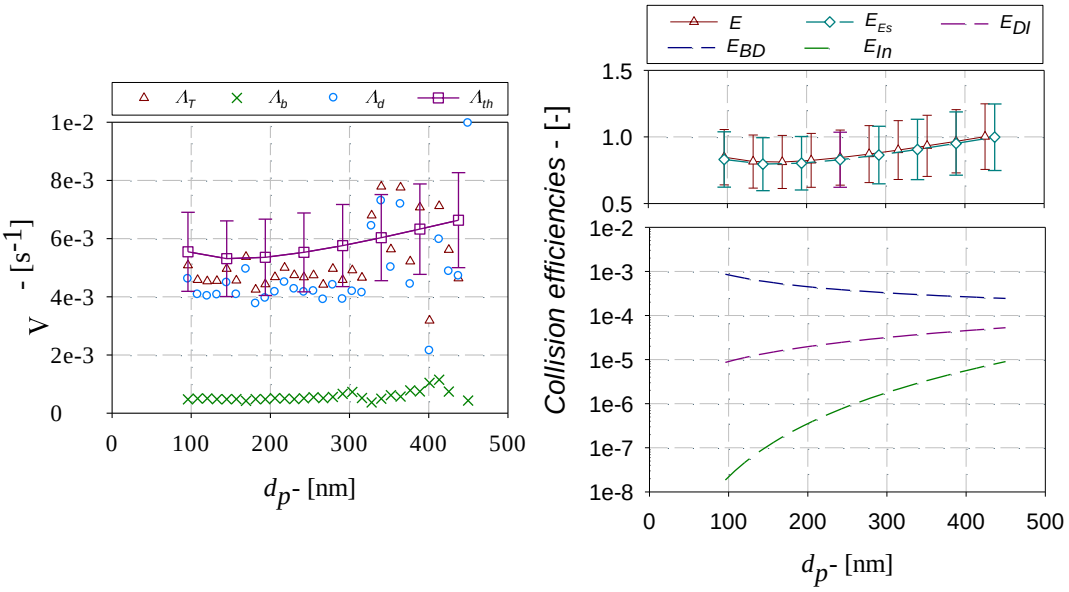
Λ_T
Λ_b
Λ_d
Λ_{th}
V - [s^{-1}]
d_p- [nm]
E
E_{Es}
E_{DI}
E_{BD}
E_{In}
Collision efficiencies - [-]
d_p- [nm]

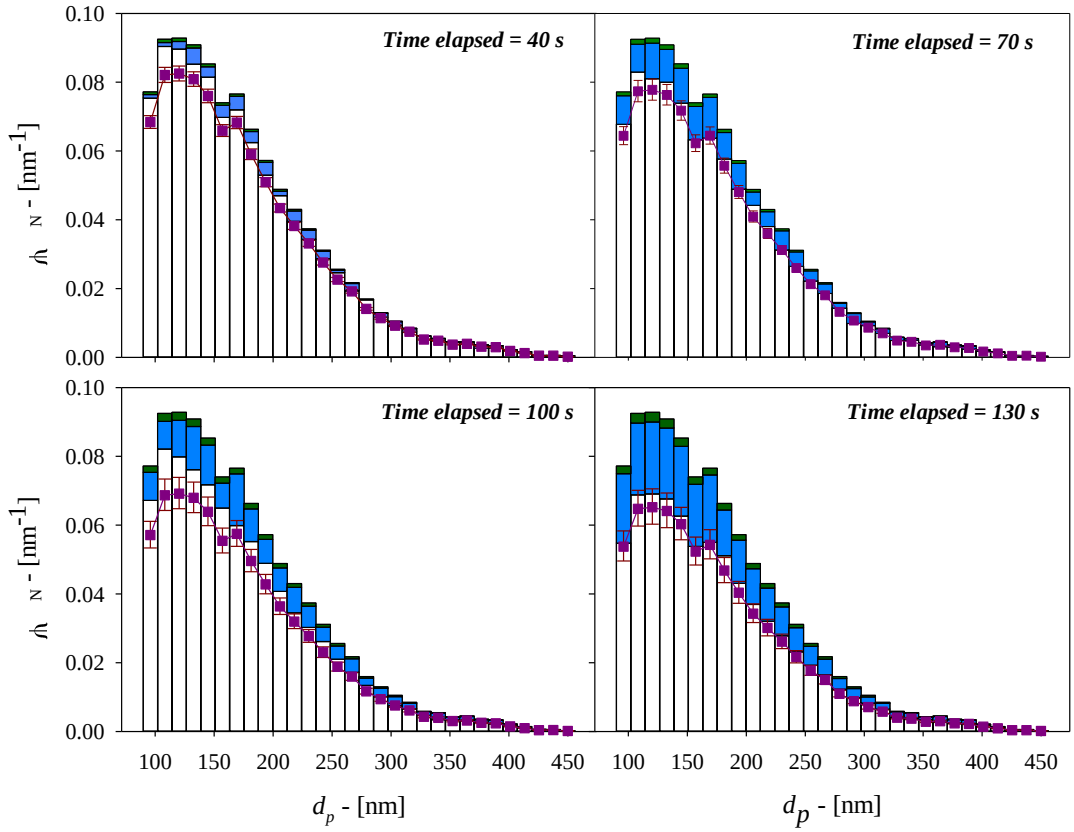
Time elapsed = 40 s
Time elapsed = 70 s
Time elapsed = 100 s
Time elapsed = 130 s
n_N - [nm^{-1}]
d_p - [nm]

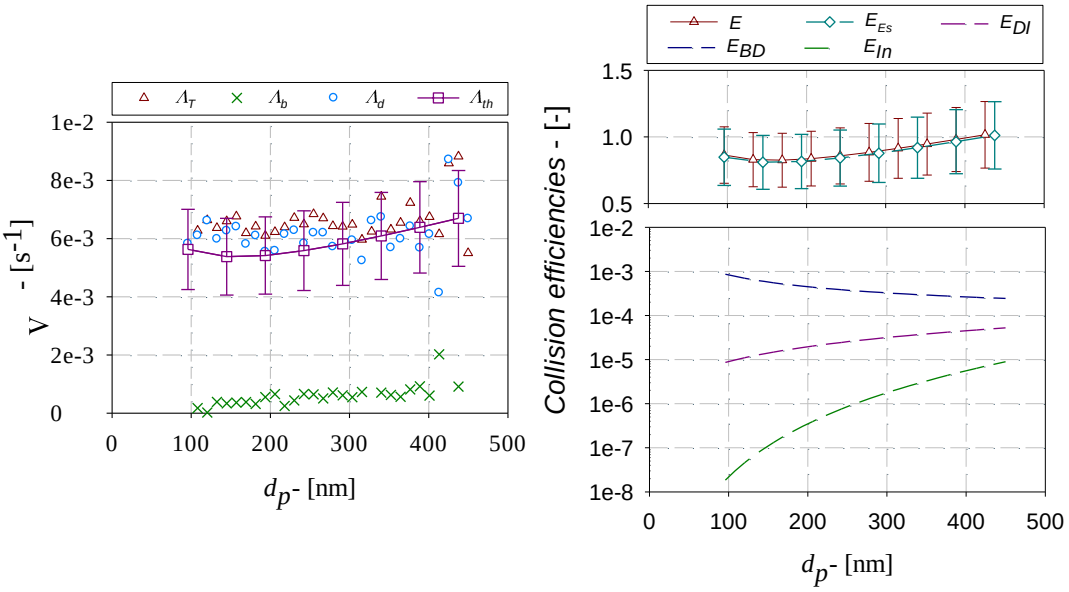
Λ_T
Λ_b
Λ_d
Λ_{th}
V - [s^{-1}]
d_p- [nm]
E
E_{Es}
E_{DI}
E_{BD}
E_{In}
Collision efficiencies - [-]
d_p- [nm]

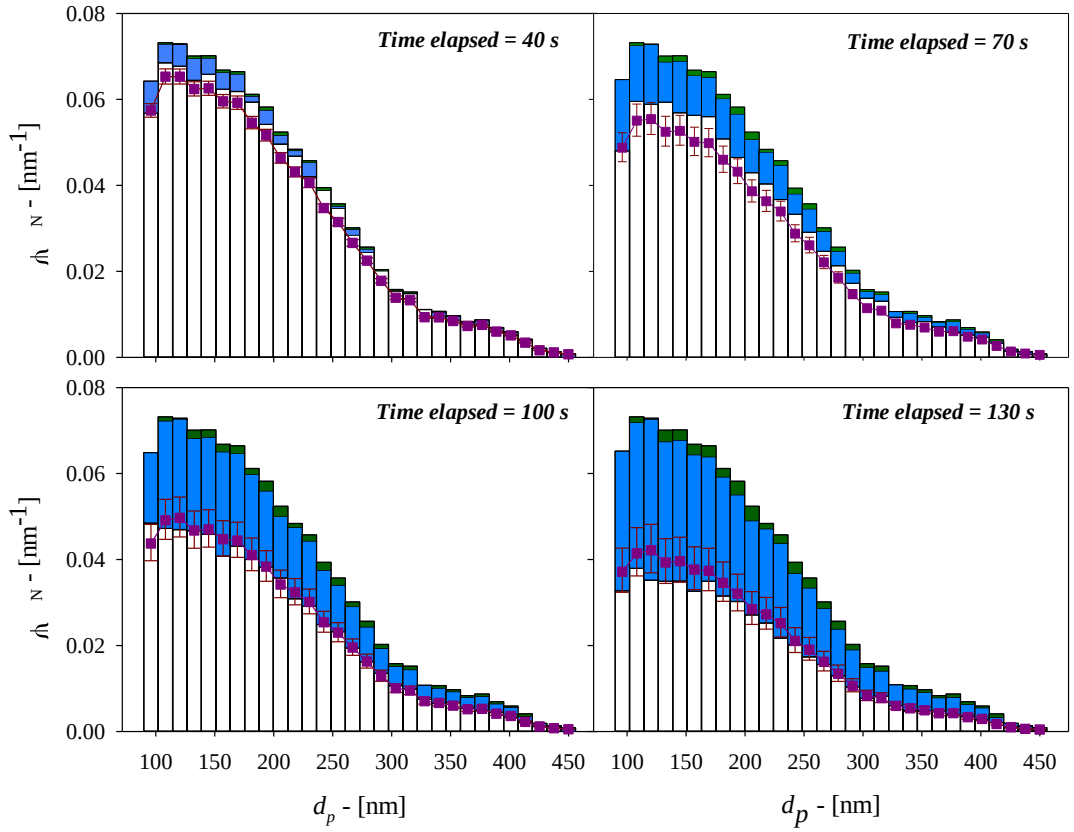
Time elapsed = 40 s
Time elapsed = 70 s
Time elapsed = 100 s
Time elapsed = 130 s
ΔN - [nm^{-1}]
d_p - [nm]

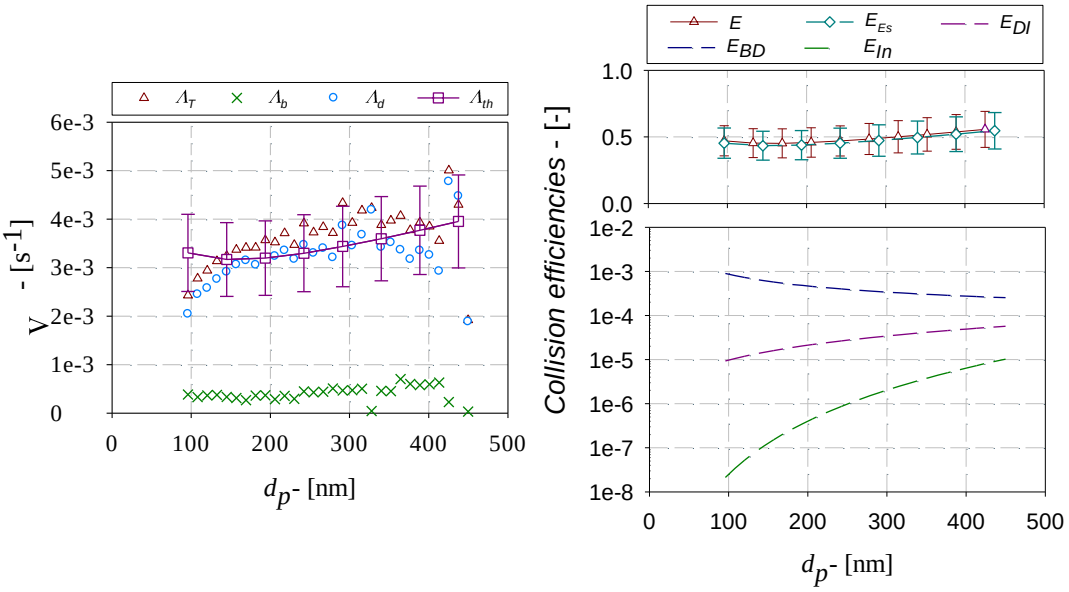
Λ_T
Λ_b
Λ_d
Λ_{th}
Λ - [s^{-1}]
d_p- [nm]
E
E_{Es}
E_{DI}
E_{BD}
E_{In}
Collision efficiencies - [-]
d_p- [nm]

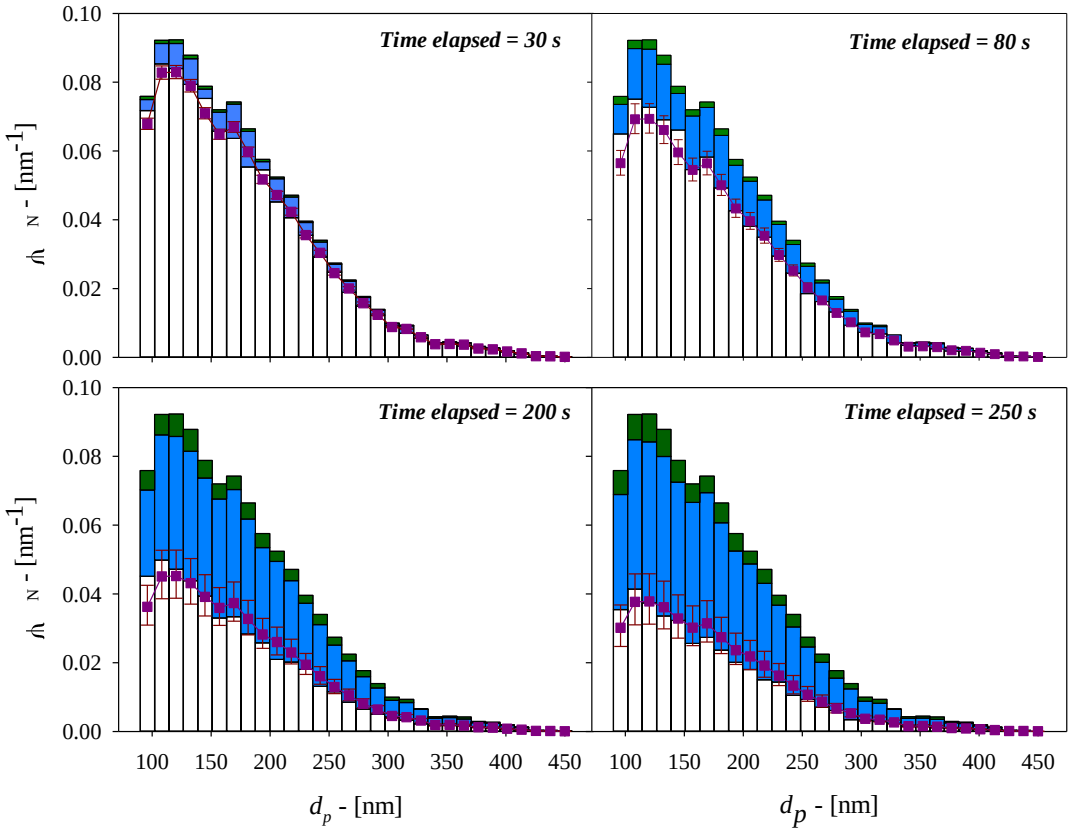
Time elapsed = 30 s
Time elapsed = 80 s
Time elapsed = 200 s
Time elapsed = 250 s
n_N - [nm^{-1}]
d_p - [nm]

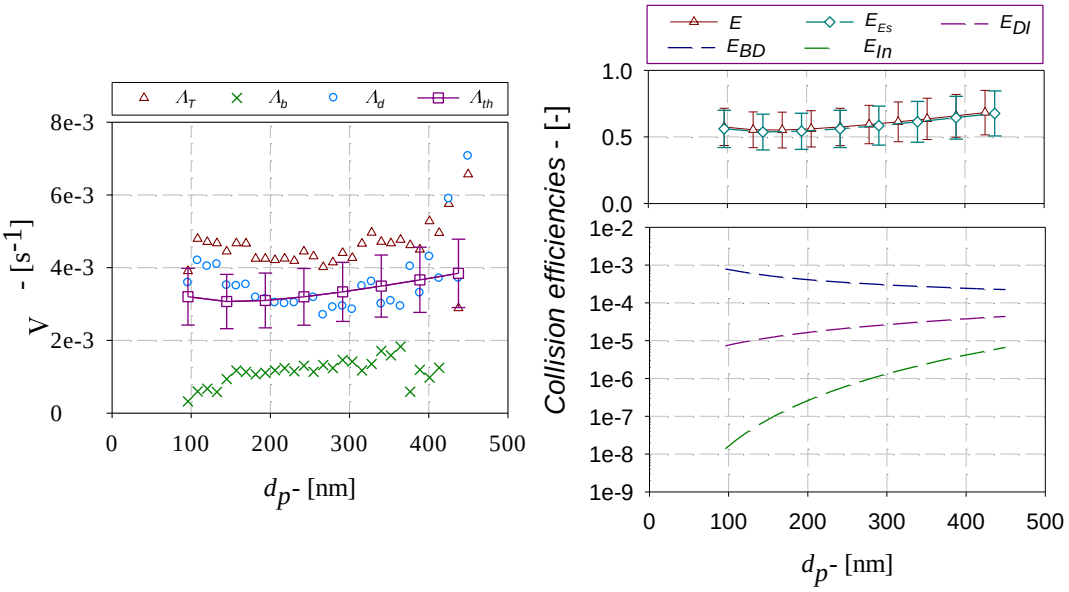
Λ_T
Λ_b
Λ_d
Λ_{th}
8e-3
6e-3
4e-3
2e-3
0
Λ - [s^{-1}]
0
100
200
300
400
500
d_p- [nm]
E
E_{Es}
E_{DI}
E_{BD}
E_{In}
1.0
0.5
0.0
1e-2
1e-3
1e-4
1e-5
1e-6
1e-7
1e-8
1e-9
Collision efficiencies - [-]
0
100
200
300
400
500
d_p- [nm]

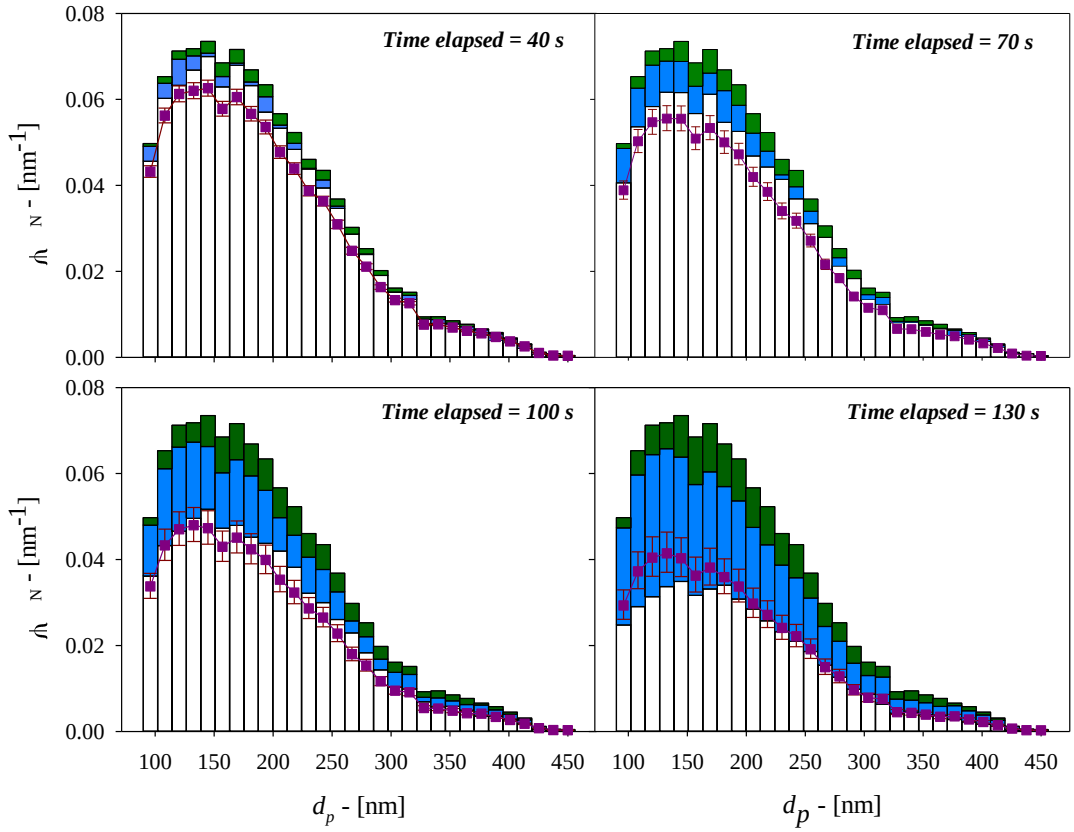
Time elapsed = 40 s
Time elapsed = 70 s
Time elapsed = 100 s
Time elapsed = 130 s
0.08
0.06
0.04
0.02
0.00
n_N - [nm^{-1}]
100
150
200
250
300
350
400
450
d_p - [nm]